Three-dimensional structure of kinetochore-fibers in human mitotic spindles

Robert Kiewisz[1,†1,†2], Gunar Fabig[1], William Conway[2], Daniel Baum[3], Daniel Needleman[2,4,5,6], and Thomas Müller-Reichert[1]

[1]Experimental Center, Faculty of Medicine Carl Gustav Carus, Technische Universität Dresden, 01307 Dresden, Germany

[2]Department of Physics, Harvard University, Cambridge, MA 02138, USA

[3]Department of Visual and Data-Centric Computing, Zuse Institute Berlin, 14195 Berlin, Germany

[4]Department of Molecular and Cellular Biology, Harvard University, Cambridge, MA 02138, USA

[5]John A. Paulson School of Engineering and Applied Sciences, Harvard University, Cambridge, MA 02138, USA

[6]Center for Computational Biology, Flatiron Institute, New York, NY 10010, USA

[†1]Current address: Biocomputing Unit, Centro Nacional de Biotecnologia (CNB-CSIC), Darwin, 3, Campus Universidad Autonoma, 28049 Cantoblanco, Madrid, Spain

[†2]Current address: Simons Machine Learning Center, New York Structural Biology Center, New York, NY 10027, USA

For correspondence:

T. Müller-Reichert

E-mail: mueller-reichert@tu-dresden.de

Phone: +49 351 458 6442

R. Kiewisz

E-mail: rkiewisz@nysbc.org

Abstract

During cell division, kinetochore microtubules (KMTs) provide a physical linkage between the chromosomes and the rest of the spindle. KMTs in mammalian cells are organized into bundles, so-called kinetochore-fibers (k-fibers), but the ultrastructure of these fibers is currently not well characterized. Here we show by large-scale electron tomography that each k-fiber in HeLa cells in metaphase is composed of approximately nine KMTs, only half of which reach the spindle pole. Our comprehensive reconstructions allowed us to analyze the three-dimensional (3D) morphology of k-fibers and their surrounding MTs in detail. We found that k-fibers exhibit remarkable variation in circumference and KMT density along their length, with the pole-proximal side showing a broadening. Extending our structural analysis then to other MTs in the spindle, we further observed that the association of KMTs with non-KMTs predominantly occurs in the spindle pole regions. Our 3D reconstructions have implications for KMT growth and k-fiber self-organization models as covered in a parallel publication applying complementary live-cell imaging in combination with biophysical modeling (Conway et al., 2021). Finally, we also introduce a new visualization tool allowing an interactive display of our 3D spindle data that will serve as a resource for further structural studies on mitosis in human cells.

Introduction

Chromosome segregation during cell division is carried out by microtubule (MT)-based spindles (Anjur-Dietrich et al., 2021; McIntosh et al., 2013; Oriola et al., 2018; Prosser and Pelletier, 2017). While mitotic spindles can contain thousands of MTs, only a fraction of those highly dynamic filaments is associated with the kinetochores (Redemann et al., 2017). These MTs are called kinetochore microtubules (KMTs) and function to establish a physical connection between the chromosomes and the rest of the spindle (Flemming, 1879; Khodjakov et al., 1997; Maiato et al., 2004; Musacchio and Desai, 2017; Rieder, 1981; Rieder and Salmon, 1998).

The regulation of KMT dynamics in mitotic spindles has been studied in great detail in a number of different systems, including the early *Caenorhabditis elegans* embryo, *Xenopus* egg extracts and mammalian tissue culture cells (DeLuca et al., 2006; Dumont and Mitchison, 2009; Farhadifar et al., 2020; Inoué and Salmon, 1995; Kuhn and Dumont, 2019; Long et al., 2020). However, our understanding of the ultrastructure of KMTs in mammalian k-fibers is rather limited due to a low number of three-dimensional (3D) studies on spindle organization. Earlier studies applied several techniques. Some studies used serial thin-section transmission electron microscopy (TEM) (Khodjakov et al., 1997; McDonald et al., 1992; McEwen and Marko, 1998) and partial 3D reconstruction by electron tomography (O’Toole et al., 2020; Yu et al., 2019). Other studies used scanning electron microscopy to analyze the ultrastructure of mitotic spindles (Hoffman et al., 2020; Nixon et al., 2017, 2015). However, these prior studies did not present comprehensive 3D reconstructions of mammalian mitotic spindles. Nevertheless, by applying serial thin-section TEM it was reported that k-fibers in PtK_1 cells are composed of about 20 KMTs (McDonald et al., 1992; McEwen et al., 1997). In contrast, tomographic analysis of RPE-1 cells revealed 12.6 ± 1.7 KMTs per k-fiber (O’Toole et al., 2020). Moreover, different cell types can exhibit a wide range of chromosome sizes, which could be an important factor modulating the number of attached KMTs (Moens, 1979). This variation in the reported numbers of KMTs per k-fiber as well as a lack of complete 3D models of human mitotic spindles motivated us to perform an in-depth analysis of the k-fiber organization and KMT length distribution in the context of whole mitotic spindles in human tissue culture cells.

It was shown that mitotic KMTs exhibited various patterns of organization in different species. Single KMTs are connected to the kinetochores in budding yeast (Winey et al., 1995), while multiple KMTs are connected to dispersed kinetochores in nematodes (O’Toole et al., 2003; Redemann et al., 2017). Multiple KMTs connected to kinetochores are also observed in human cells. However, KMTs in these cells are organized into bundles, termed “kinetochore (k)-fibers”, which are attached to a single region on each chromosome (Begley et al., 2021; Godek et al., 2015; Inoué, 1953; Metzner, 1894; Mitchison and Kirschner, 1984; O’Toole et al., 2020; Schmidt, 1939).

Three different simplified models of k-fiber organization can be drawn. Firstly, a direct connection between kinetochores and spindle poles can be considered (**Figure 1A**), in which all KMTs in a given k-fiber have approximately the same length and are rigidly connected (Rieder, 1981; Ris and Witt, 1981). Secondly, an indirect connection may be considered (**Figure 1B**). In such a model, none of the KMT minus ends would be directly associated with the spindle poles, thus KMTs would show differences in their length and connect to the poles purely by interactions with non-KMTs in the spindle. Thirdly, the kinetochore-to-spindle pole connection may be neither direct nor indirect, thus showing a semi-direct pattern of connection, in which only some of the KMTs in a given k-fiber are associated with the spindle pole while others are not (**Figure 1C**). Previously, we have shown such a semi-direct pattern of KMT anchoring into the spindle network for the first embryonic mitosis in *C. elegans* (Redemann et al., 2017). Some KMTs in this nematode system are indeed directly associated with the spindle poles, while others are not. As far as the length of the KMTs in mammalian cells is concerned, a difference in their length had previously been reported for PtK$_1$ cells (McDonald et al., 1992). We, therefore, wondered how the anchoring of k-fibers into the spindle network is achieved in mammalian cells.

Here, we aimed to determine the number and length of KMTs and the positioning of their putative minus ends in human HeLa cells. We further aimed to analyze the organization of k-fibers and the interaction of KMTs with non-KMTs in whole mammalian spindles. Focusing on the metaphase stage, we applied serial-section electron tomography to produce large-scale reconstructions of entire mitotic spindles in HeLa cells. To achieve this, we developed software tools for a quantitative in-depth analysis of both KMTs and non-KMTs (https://github.com/RRobert92/ASGA). We found that k-fibers in HeLa cells display a previously unexpected variable morphology. The k-fibers indeed contain KMTs of different lengths (a semi-direct type of connection with the spindle pole) and show an uncoupling of KMT minus ends at the site of preferred interaction with the spindle poles. For better visualization of KMT organization and k-fiber morphology, we introduce here a new 3D visualization tool that allows the interested reader to interactively display the 3D data (https://cfci.shinyapps.io/ASGA_3DViewer/).

Results

K-fibers are composed of approximately nine KMTs

For our large-scale analysis of mammalian k-fibers, we acquired data on metaphase spindles in HeLa cells by serial-section electron tomography (**Figure 2A-B**). To visually inspect the quality of our samples, we extracted slices of regions of interest (**Figure 2-figure supplement 1**). We also used the tomogram data to reconstruct full spindles in 3D for quantitative analysis of the spindle morphology (**Figure 2-videos 1-3**). In preparation for this quantitative analysis, we applied a Z-factor to our 3D models to correct for a sample collapse that had occurred during the acquisition of the tomographic data (**Figure 2-figure supplement 2**). In our three full reconstructions, we segmented all MTs, the chromosomes and the spindle poles (including the centrioles). Each of these metaphase spindles was composed of approximately 6300 MTs (6278 ± 1614 MTs, mean ± STD; **Figure. 2C-E**; **Table 1**) and had an average pole-to-pole distance of 9.0 ± 1.7 µm (mean ± STD; **Figure 2-figure supplement 3A-B**; **Table 1**).

We then annotated the KMTs in our reconstructions based on the association of the putative MT plus ends with kinetochores. MTs that were arranged in parallel and made end-on contact at a single ‘spot’ on the chromosomes were defined as KMTs being part of the same k-fiber. For this publication, these bundled KMTs were considered the ‘core’ of the k-fibers. Possible interactions of these KMTs with other MTs (referred to here as non-KMTs) in the spindle were subject to subsequent steps of our in-depth spindle analysis. In our tomographic data sets, we identified between 90 and 110 k-fibers per cell, which included on average 859 ± 218 KMTs (mean ± STD; n = 3; **Figure 2F-H**; **Figure 2-videos 4-6**; **Table 1**) in each spindle. Thus, only ~14% of all MTs in the reconstructed spindles were KMTs. The majority of annotated KMTs displayed open flared ends at the kinetochore (**Figure 2-figure supplement 4**), consistent with previous observations on the morphology of KMT plus ends in mammalian cells (**McIntosh et al., 2013**). We took advantage of these extracted k-fibers to further analyze the distance between the sister k-fiber ends in each data set. For this, we measured the median position of the KMT plus ends at each k-fiber and then determined the distance between the median of KMT plus-end positions of sister k-fibers (**Figure 2-figure supplement 3C-D**; **Table 1**). The average distance between the sister k-fiber ends was 1.13 ± 0.24 µm (mean ± STD; n = 292). The similarity in the median distance between sister k-fiber ends in the three reconstructions indicated to us that the selected pre-inspected spindles were indeed cryo-immobilized at a similar mitotic stage, thus allowing a further comparative quantitative analysis of our 3D models.

Next, we extracted individual k-fibers from our full 3D reconstructions to visualize their overall morphology (**Figure 3A**; **Figure 3-videos 1-6**). Our serial-section approach enabled us to follow each KMT in each k-fiber in 3D. This was achieved by semi-automatic stitching of the corresponding ends over section borders (**Figure 3-figure supplement 1**; (Lindow et al., 2021)). In addition to this semi-automatic stitching, each KMT in our reconstructions was manually checked for a proper end identification. The individual k-fibers showed remarkable variability in their overall shape. Some k-fibers were rather straight, while others were very curved. At the kinetochores, k-fibers showed a compacted appearance, while k-fibers were considerably broader at their pole-proximal end. Interestingly, some KMT minus ends extended beyond the position of the centrioles (**Figure 3A - #I - #III**).

We further investigated the number of KMTs associated per kinetochore (**Figure 3B**; **Figure 3-figure supplement 2A**; **Table 2**) and found that the k-fibers were composed of around 9 KMTs (8.5 ± 2.2, mean ± STD, n = 292). To exclude the possibility that the average number of KMTs attached to kinetochores is influenced by a possible stretch of the sister kinetochores, we plotted both the number of attached KMTs and the difference (delta) in the number of KMTs associated with the respective sister kinetochore against the distance between the kinetochore-proximal ends of k-fiber pairs. We did not observe a correlation between these parameters (**Figure 3C-D**; Pearson's correlation coefficients were 0.04 and 0.29) and concluded that the number of KMT attachments to kinetochores in metaphase is not influenced by a variation in the inter-kinetochore distance. Another variable with a possible influence on the number of attached KMTs to the outer kinetochores could be the position of the k-fibers within the metaphase spindle. Because spindles show a rounded appearance at metaphase, a difference in the number of attached MTs to the outer kinetochores could be influenced by the overall spindle shape. To analyze such a possible positional effect, we considered the cross-section of the metaphase plate as an ellipse and defined a central, an intermediate and a peripheral zone on this ellipse (**Figure 3-figure supplement 3A**). By determining the position of the kinetochores on the 3D-reconstructed metaphase plate, we then annotated each k-fiber in our three data sets to one of these regions (**Figure 3-figure supplement 3B-M**). Keeping the roundedness of spindles at metaphase in mind, we indeed observed that k-fibers positioned in the center are rather straight, while peripheral k-fibers are more curved. However, we did not find a difference in the number of attached KMTs for these three different regions (**Figure 3-figure supplement 3N**; **Table 4**) and concluded that also the position of the k-fibers within the spindle has no effect on the average number of KMTs per k-fiber.

We were also interested in measuring the density and spacing of KMTs at the kinetochore, thus allowing subsequent analysis of KMT density along the k-fiber length. Because kinetochores show relatively lower contrast in high-pressure frozen material compared to conventionally prepared samples (McEwen et al., 1998b), we indirectly measured the size of the kinetochores in our spindles by determining the cross-sectional area of the k-fibers (i.e., by encircling the KMTs) close to the outer kinetochore plate. The measured average kinetochore area was 0.10 ± 0.07 μm^2 (mean ± STD; **Figure 3-figure supplement 2B-C**). We then analyzed the density of KMTs at the outer kinetochores by counting the number of KMTs within the determined areas, which was 112 ± 60 KMTs/μm^2 (mean ± STD, n = 292; **Figure 3-figure supplement 2D**; **Table 2**). In addition, we observed an average center-to-center distance between neighboring KMTs of 74 ± 22 nm (mean ± STD, n = 292; **Figure 3-figure supplement 2E**; **Table 3**). Considering an MT diameter of 25 nm, this corresponds to an average wall-to-wall spacing of about 50 nm between the KMTs at the outer kinetochore. Thus, following our initial visual inspection of k-fibers, the KMTs tend to be highly compacted at the outer kinetochore.

We measured the length of the KMTs in our reconstructed k-fibers and observed a broad distribution of KMT lengths with an average value of 3.87 ± 1.98 µm (mean ± STD; n = 2580; **Figure 4A**; **Figure 4-figure supplement 1A**; **Table 2**). Our analysis revealed the existence of relatively short KMTs in central, intermediate and peripheral k-fibers that were not associated with the spindle poles (**Figure 4-figure supplement 2-3**; **Table 4**). Indeed, about 20 ± 4% of the KMTs had lengths less than 2 µm. Our analysis also showed relatively long KMTs (about 39 ± 10%) that were longer than the half spindle length. Some of these long KMTs showed a pronounced curvature at their pole proximal end, thus connecting to the 'back side' of the spindle poles (see also **Figure 3A** - k-fiber #**I** - #**III**; **Figure 3-videos 1-3**).

We continued our study by further analyzing the pole proximal ends (from now on called minus ends). As a first step, we annotated each KMT minus end in our spindle reconstructions. The development of appropriate software allowed us then to determine both the distance of the KMT minus ends to the nearest spindle pole and the relative position of the KMT minus ends along the pole-to-kinetochore axis (**Figure 5A**; (Kiewisz and Müller-Reichert, 2021)). In addition, we were also interested in the percentage of the KMT minus ends that were directly associated with the spindle poles. Similar to our previously published analysis of spindle morphology in the early *C. elegans* embryo (Redemann et al., 2017), we defined an MT-centrosome interaction area. For this, we plotted the distribution of all non-KMT minus-end distances to the nearest spindle pole. The distribution peaked ~1 µm from the pole and then fell before plateauing in the spindle bulk. To find the edge of the MT-centrosome interaction area, we fit a Gaussian to the distribution peak and defined the cutoff distance for the edge of the MT-centrosome interaction area as two fit half-widths from the center of the fit peak, 1.7 µm from the mother centriole. (**Figure 5B**, gray area). In other words, KMTs with their minus ends positioned at 1.7 µm or less to the center of the nearest mother centriole (i.e., inside this MT-centrosome interaction zone) were defined to be directly associated with a pole, while KMT minus ends positioned farther than this cut-off distance of 1.7 µm were called indirectly associated with the spindle pole. We then measured the distance of each KMT minus-end to the nearest mother centriole (**Figure 5C**; **Figure 5-figure supplement 2A**). Taking our determined cut-off value into account, we found that only 49% (± 15.5%; ± STD, n = 3) of the KMT minus ends were positioned within the defined MT-centrosome interaction area. This is in accord with our observation that the average number of KMTs per k-fiber at the spindle pole (4.1 ± 2.0; **Figure 5-figure supplement 3**; **Table 2**) was lower compared to the average number of KMTs per k-fiber at the kinetochore (8.5 ± 2.2; **Figure 3B**). All in all, this suggested to us that only half of the KMTs in HeLa cells are directly connected to the spindle pole, while the other half of the KMTs are indirectly connected.

Interestingly, we also observed that the number of KMT minus ends associated with the spindle poles was significantly higher in k-fibers positioned in the center compared to those at the periphery of the mitotic spindle. In addition, the average length of KMTs in central k-fibers and their minus-end distance to the spindle pole were significantly lower compared to those observed in peripherally positioned k-fibers (**Figure 5-figure supplement 4**; **Table 4**). This suggested to us that the position of the k-fibers within the spindle affects the ultrastructure of the individual KMTs.

We next investigated the relative position of the KMT minus ends on the pole-to-kinetochore axis (**Figure 5D**; **Figure 5-figure supplement 1**; **Figure 5-figure supplement 2B**; **Table 2**). We found that the KMT minus ends that were positioned within the MT-centrosome interaction zone showed a peak position close to the center of the spindle poles. In contrast, KMT minus ends outside this interaction area did not show a preferred position but rather displayed a flat relative distribution on the pole-to-kinetochore axis. This analysis confirmed our initial visual 3D inspection of the KMTs, revealing that the k-fibers in HeLa cells are not composed of compact bundles of KMTs of the same length but rather show KMTs of different lengths, thus confirming previously published data (McDonald et al., 1992; O'Toole et al., 2020).

For comparison, we also analyzed the length distribution of non-KMTs in the spindles. Non-KMTs had an average length of 2.0 ± 1.7 µm (mean ± STD; n = 9957; **Figure 4B**; **Figure 4-figure supplement 1B**) showing a high number of very short (< 2 µm) and a low number of long MTs (> half spindle length). In addition, 38 ± 9% of the non-KMT minus ends were localized in the defined MT-centrosome interaction zone and the remaining ~60% were located in the bulk of the spindle (**Figure 5F**; **Figure 2-figure supplement 2C**; **Table 2**). In addition, the distribution plot of the relative position of the non-KMT minus ends on the pole-to-pole axis showed two peaks at the spindle poles (**Figure 5G**; **Figure 5-figure supplement 2D**). Overall, this indicated to us that the non-KMTs show a very high number of very short MTs that is different from the flatter length distribution of KMTs.

K-fibers are broadened at spindle poles

Previous light microscopic observations have indicated that metaphase spindles show an internal twist (Novak et al., 2018; Taubenberger et al., 2020), which might possibly be a consequence of motor protein-related forces acting within the spindle. We wondered whether k-fibers show a characteristic curvature of MTs also in our data. Therefore, we were interested in whether such a twist can also be observed when analyzing 3D reconstructions of whole spindles by stitching serial sections for electron tomography. As a measure, we decided to analyze the tortuosity of individual KMTs in our 3D models. Tortuosity is the ratio of the total length of a curve (the spline length of a given KMT) to the distance between its ends. Straight KMTs, therefore, have a tortuosity of 1, while a quarter circle has a tortuosity of around ~1.1 and a half-circle of around ~1.6 (**Figure 6A**). Because the tortuosity of KMTs might not be homogeneous throughout the spindle, we aimed to measure both their global and local tortuosity in our 3D reconstructions, i.e., the tortuosity of the KMTs along their entire length and also in defined sections of a length of 500 nm along the k-fibers, respectively (**Figure 6B-C**).

Firstly, we analyzed the global tortuosity of the KMTs. For this, we applied a color code to our 3D models to visualize differences in the curvature of individual KMTs (**Figure 6D**; **Figure 6-movies 1-3**). For all data sets, we observed an average value of KMT tortuosity of 1.1 ± 0.1 (mean ± STD, n = 2580). We found that 62% ± 8% of the KMTs showed a tortuosity of lower than 1.1 and 38 ± 10% of the KMTs displayed a tortuosity higher than 1.1 (**Figure 6E**; **Table 3**). We also observed that straight KMTs (tortuosity <= 1.1) were predominantly located in the center of the spindle, while curved KMTs (tortuosity > 1.1) were located more at peripheral spindle positions (**Figure 6F**; **Figure 6-figure supplement 1, Table 4**). Furthermore, the global tortuosity of KMTs was correlated with their length. As expected, short KMTs were straighter, while long KMTs were more curved (R = 0.68; p = 2.2e-16; **Figure. 6G**). In addition, 75 ± 6% of the KMTs with a tortuosity higher than 1.1 were longer than the half-spindle length. Secondly, we also investigated the local tortuosity of the KMTs. For each KMT, we applied the same color code as used for the analysis of global tortuosity (**Figure 6H**). Then we plotted the tortuosity value for each 500 nm segment against the position on the pole-to-kinetochore axis (**Figure 5-figure supplement 1**). Our analysis revealed that the tortuosity of KMTs was not uniform along the pole-to-kinetochore axis. Importantly, the local tortuosity of the KMTs was weakly correlated with the relative position of the KMT segments on the pole-to-kinetochore axis, meaning that the local tortuosity slowly increased constantly from the kinetochores towards the spindle poles (R = -0.13; p = 2.2e-16; **Figure 6I**). Extending previously published knowledge, we showed that KMTs have a higher tortuosity at the spindle poles compared to the kinetochores.

Next, we also asked whether an increased KMT tortuosity at the spindle poles is reflected in the compactness of the k-fibers along their k-fiber length. For this, we analyzed cross-sections of k-fibers to determine their polygonal areas (**Figure 7A**; **Figure 7-figure supplement 1**). In the interest of precision, we considered such a polygonal analysis superior to an analysis of fitting circles to determine cross-sectional areas. Cross-sections of k-fibers showed an average polygonal area of 0.097 ± 0.161 μm^2 (± STD, n = 292). We then continued by plotting the values for these polygonal areas against the relative position on the pole-to-kinetochore axis (**Figure 7B**; **Table 3**). We measured an average polygonal area of 0.034 ± 0.019 μm^2 at the kinetochores, 0.149 ± 0.210 μm^2 in the middle of the spindles, and 0.092 ± 0.146 μm^2 at the spindle poles. Compared to the position at the kinetochore, the average polygonal area of the k-fibers was about 4-fold higher in the middle of the spindles and roughly 3-fold higher at the spindle poles. Moreover, the cross-section polygonal area of the k-fibers showed a higher spread of values at the spindle poles compared to the kinetochores, thus reflecting the observed broadened appearance of the k-fibers at the spindle poles.

To further characterize the arrangement of the KMTs in the k-fibers, we also set out to measure the number of the KMTs along the length of the k-fibers (**Figure 7C**). For each k-fiber, we defined a circle enclosing all KMTs at the kinetochore. We then measured the number of KMTs that were included in this defined k-fiber circle and plotted the percentage of the enclosed KMTs against the relative position along the pole-to-kinetochore axis. We observed a variation in the percentage of enclosed KMTs along the k-fiber length. As defined, the highest percentage of enclosed KMTs was observed at the outer kinetochore. However, at the spindle poles, roughly only 64% of the KMTs were enclosed (**Table 3**). Thus, the density of KMTs in the k-fibers at the spindle poles was decreased compared to the one observed at the outer kinetochore (**Figure 7D**). From all these analyses we concluded that k-fibers display a higher tortuosity and a lower KMT density close to the spindle poles compared to the position at the kinetochores, thus leading to a broadened appearance of the pole-proximal ends.

KMTs primarily associate with non-KMTs at spindle poles

So far, we had concentrated only on an analysis of KMT morphology and considered these bundled MTs as the ‘core structure’ of the k-fibers. Likely, the observed organization of KMTs in k-fibers is the result of KMTs interacting with other non-KMTs in the spindle, thus contributing to the maturing of k-fibers (Almeida et al., 2021). Therefore, we also aimed to investigate patterns of association of KMTs with the neighboring non-KMTs in our 3D reconstructions. Moreover, we were particularly interested in localizing such KMT/non-KMT associations in the spindles to map the detected positions of MT-MT interaction on the pole-to-kinetochore axis. In general, we considered two types of interactions between MTs. Firstly, we analyzed potential interactions between MT ends with neighboring MT lattices, which could be mediated by MT minus-end associated molecular motors such as dynein (Tan et al., 2018) or kinesin-14 (Molodtsov et al., 2016)**,** by other MT-associated proteins such as HDAC6 (Ustinova et al., 2020), Tau (Bougé and Parmentier, 2016) or by □-tubulin (Rosselló et al., 2018). Secondly, we considered MT-MT lattice interactions, which might be established by molecular motors such as kinesin-5 (Falnikar et al., 2011) or PRC1 (Mollinari et al., 2002). Both types of interactions are also displayed here by using our new 3D visualization tool. The aim of applying this tool is to enable an illustration of the 3D complexity of such KMT/non-KMT interactions.

We started our analysis by investigating possible KMT minus-end associations with either KMT or non-KMT lattices. For this, we annotated all KMT minus ends in our 3D reconstructions and measured the distance of each minus end to a neighboring MT lattice (**Figure 8A**). We then determined association distances (i.e., 25, 30, 35, 45, 50, 75 and 100 nm) to quantify the number of associations occurring within these given interaction distances (Kellogg et al., 2016; Redwine et al., 2012). From this, we further determined the percentage of all KMT minus ends that were associated with non-KMT lattices according to selected association distances (**Figure 8B**; **Table 5** and **Table 6**). As expected, we observed that the number of KMT minus ends associated with adjacent MT lattices increased with an increase in the association distance. Considering 35 nm as an example of a possible interaction distance between two MTs connected by a single dynein motor (Amos, 1989), we observed that only 32.6 ± 5.5% of all KMT minus ends were associated with other MTs (for a visualization of the pattern of association see **Figure 8C**; **Figure 8-figure supplement 1**; **Figure 8-video 1**). Moreover, of all KMT minus ends that were not associated with the spindle poles (i.e., those positioned farther than 1.7 µm away from the centrioles) only 32.8 ± 24.9% showed an association with other MT lattices at a given distance of 35 nm (**Figure 8D-E**). This suggested that for this given distance of association roughly only 30% of the KMT minus ends in k-fibers were associated with the MT network. Further considering larger distances of association between KMT minus end and neighboring MT lattices (**Figure 8B** and **Figure 8D**), we also observed that not all

KMT minus ends were associated with neighboring MTs even at a value of 100 nm (**Table 5** and **Table 6**).

Next, we sought to map the positions of the detected associations of KMT minus ends with either KMT or non-KMT lattices within the reconstructed spindles. We then determined the position of such associations in our spindles and plotted the data against the relative position on the pole-to-kinetochore axis. For this, we normalized the pole-to-kinetochore axis against the MT density at each given position. We first plotted the number of KMT minus-end associations with KMT lattices against the relative position on the pole-to-kinetochore axis (**Figure 8F**; **Figure 8-figure supplement 2A**). Associations of KMT minus ends with KMT lattices. KMT minus ends were distributed along the pole-to-kinetochore axis with a preference for positions at the spindle poles. As an example, for a given association distance of 35 nm, 60.7 ± 9.4% of the total number of associations were observed at the spindle poles. We then also determined the relative position of the KMT minus-end associations with non-KMT lattices (**Figure 8G**; **Figure 8-figure supplement 2E**). Similarly, the majority of the associations of KMT minus ends with non-KMT lattices were observed at the spindle poles. For the chosen distance of 35 nm, 44.7 ± 5.2% of these associations were observed at the spindle poles. Thus, the spindle poles appeared as the major sites for interaction of KMT minus ends with neighboring MT lattices.

Vice versa, we also determined the occurrence of either KMT or non-KMT minus ends in the vicinity of KMT lattices (**Figure 8-figure supplement 2** and **3**; **Figure 8-video 2**). At 35 nm or closer to the KMT lattice, we observed that on average 42 ± 8 % of KMTs associated with either KMT or non-KMT minus ends, with the majority of associations with non-KMT minus ends (**Table 7** and **Table 8)**. Moreover, we also determined the relative position of these associations on the spindle axis. Again, the majority of KMT lattices (59.8 ± 6.7%) associated with other MT minus ends were preferentially found at spindle poles (**Figure 8-figure supplement 2C-D**). In contrast, only 39.1 ± 4.6% of non-KMTs associated with other MT minus ends were found at the poles (**Figure 8-figure supplement 2G-H**). Again, this analysis indicated that the interaction of KMTs with other MTs preferentially takes place at the spindle poles regardless of the association distance.

In parallel to an analysis of the position of possible MT-MT associations on the pole-to-kinetochore axis, we were also interested in studying the length and number of these associations in the spindles on each MT, as such information would also help to recognize specific patterns of MT-MT interaction. For a pairing length analysis as previously applied (McDonald et al., 1992; Winey et al., 1995), we defined 20 nm as a minimal length of interaction. For each MT, we also counted the number of continuous interaction segments over which they retained this minimal association proximity (**Figure 9A**). In addition, we also varied the distance between associated MTs by choosing values of 25, 30, 35, 45 and 50 nm. As expected, the peaks in the number of KMTs changed rapidly with an increase in the number and length of associations (**Table 8** and **Table 9**). We then analyzed the association of KMTs with other MTs in the spindle by plotting the number of associations against the relative position on the pole-to-pole axis. With an increase in the considered association distance between MTs, we observed an increase in the number of associations at the spindle poles and a drastic decline in the number of these associations at positions in the middle of the spindle (**Figure 9B-C**; **Figure 9-video 1**). We then also analyzed the association of non-KMTs with other MTs. In contrast to the previous analysis, by increasing the association distances we detected a considerable increase in the number of interactions near the spindle midplane. (**Figure 9D-E**; **Figure 9-video 2**). This peak is of functional importance, most likely representing the region, where kinesin motors generate pushing forces (**Shimamoto et al., 2015**). We concluded from all these analyses that KMTs and non-KMTs differ in their spatial pattern of MT-MT association. KMTs strongly interact with neighboring MTs at the spindle poles, while non-KMTs show a broad region of MT-MT interaction within the middle of the spindle potentially forming interpolar bundles (McDonald et al., 1992).

Finally, we were interested in how the distribution patterns of MT-MT interactions change in relation to the position in the spindle. With our high-resolution 3D data sets covering all MTs in the spindle, we decided to investigate the number and the length of associations for both KMTs and non-KMTs as a function of the distance between MTs. Firstly, we plotted the distribution of the number of associations and also of the length of associations (**Figure 9-figure supplement 2**). As expected, with an increase in the considered distance between MTs, KMTs showed an increase in the number and also in the average length of interactions (**Table 9** and **Table 10**). For a given MT-MT distance of 35 nm, the number of KMT associations was 10.6 ± 3.2 (mean ± STD, n = 2580) with an average MT length of association of 145 ± 186 nm (±STD, n = 2580). Secondly, we also analyzed the association of non-KMTs with any MT in the spindle. Non-KMTs showed a similar pattern of increase in the number and length of associations with increasing distances between individual MTs. For 35 nm, the number of associations was 7.4 ± 3.1 (mean ± STD, n = 9957) with an average length of association of 103 ± 118 nm (mean ± STD, n = 9957). With an increase in the distance between MTs, we observed that KMTs tend to show a higher number of associations and a higher average length of associations compared to non-KMTs. Importantly, these results were consistent for all selected association distances.

Discussion

The ultrastructure of KMTs in human k-fibers was insufficiently described prior to this study on the 3D organization of metaphase spindles. Large-scale reconstruction by serial-electron tomography (Fabig et al., 2020; Redemann et al., 2018, 2017) allowed us to quantitatively analyze KMT organization both in individual k-fibers and in the context of whole spindles.

Methodological considerations

For generating 3D reconstructions of spindles, we applied electron microscopy of plastic sections. The use of plastic sections suffers from the fact that samples undergo a collapse in the electron beam during imaging, and this is obvious by a reduction in the section thickness (Luther et al., 1988; McEwen and Marko, 1998; O'Toole et al., 2020). By expanding the complete stack of serial tomograms (**Figure 2-figure supplement 2**), it is possible to correct this loss in Z, and we did so for our three data sets covering whole metaphase spindles in HeLa cells.

Here, we used serial, semi-thick sections of plastic-embedded material for a 3D tomographic reconstruction of whole spindles. Although serial sectioning is never perfect, in that the section thickness within ribbons always shows some variability, we were able to produce data sets of remarkable similarity. This is true for our analysis of MT length distribution (**Figure 4**; **Figure 4-figure supplement 1**) and our measurements of minus-end distance to the spindle poles and minus-end positioning (**Figure 5**; **Figure 5-figure supplement 2**). In combination with a semi-automatic segmentation and stitching of MTs (Lindow et al., 2021; Weber et al., 2012), our approach enabled us to reliably model individual MTs overall section borders, thus allowing a quantitative study of MT length and end-positioning in whole spindles. In the future, we will use this routine approach to quantify MT organization also in other mammalian systems, such as RPE-1 and U2OS cells.

In electron microscopic images, centrosomes or spindle poles are visible by pairs of centrioles surrounded by electron-dense pericentriolar material (PCM). Since these membrane-less organelles do not show a clear boundary in thin sections or in electron tomograms, it is not immediately obvious how to define the edge of the spindle pole. Inspired by earlier studies in the early *C. elegans* embryo (O'Toole et al., 2003; Redemann et al., 2017; Weber et al., 2012), we determined the edge of the spindle pole from the density distribution of non-KMT minus ends in the spindle. The non-KMT minus-end density peaked a micron away from the pole and then fell before leveling off at constant non-KMT minus-end density in the spindle bulk. We defined the edge of the spindle pole as two fit-half widths from the center of the non-KMT minus-end density peak. In the HeLa spindles, this was 1.7 µm from the mother centriole. We applied the same cutoff in a parallel study on the dynamics of mammalian k-fibers (see **Figure 1** in (Conway et al., 2021)).

In this parallel study, we supplemented our electron tomography data on the KMT length distribution with light microscopic data. Essentially, our 3D reconstructions show a distribution of KMT length in metaphase that is strikingly similar to the distribution plot of KMT length as obtained by biophysical modeling in combination with light microscopy (see **Figure 8B-D** in (Conway et al., 2021)). All this shows that light and electron microscopy produce truly complementary data, although completely different methods of sample preparation and data analysis need to be applied.

KMT organization

Counting the total number of KMTs and non-KMTs in our spindles, we show that only ~14% of all MTs in the reconstructed spindles were KMTs. However, this percentage in the total number of all MTs corresponds to ~25% of the tubulin mass as measured in parallel by light microscopy (Conway et al., 2021). Comparing the average length of KMTs and non-KMTs, we also find that KMTs are on average twice as long as non-KMT. Thus, a higher value in the average length of KMTs *versus* non-KMTs contributes to a higher percentage in the tubulin mass of KMTs compared to all other MTs in the spindle.

The length distribution of KMTs in HeLa cells shows striking similarities to the distribution of KMTs observed in the early *C. elegans* embryo (Redemann et al., 2017). Both human KMTs attached to monocentric kinetochores and also nematode KMTs associated with dispersed holocentric kinetochores show a rather flat length distribution and a rather low number of both very short and very long KMTs. In contrast, non-KMTs in both systems show an exponential length distribution with a very high occurrence of very short MTs (around 57% of the non-KMTs and ~21% of KMT in HeLa cells were less than 2 µm). Exponential length distributions as found for non-KMTs are typical of dynamic instability kinetics (Burbank et al., 2007; Loiodice et al., 2019). Uniform length distribution of KMTs, however, indicates a difference in dynamics and possibly higher stability of the plus-ends against MT depolymerization. Taken together, all this argues that KMTs in both spindles have distinct properties different from those of non-KMTs.

A difference in the properties between KMTs and non-KMTs is also obvious after a cold treatment of cells. Such treated cells show cold-stable k-fibers, while most of the non-KMTs undergo depolymerization upon exposure to cold (Maiato et al., 2004). Here we can only speculate about this resistance to cold temperature. Likely, KMTs are stabilized by association with the kinetochore (Brinkley and Cartwright, 1975; DeLuca et al., 2006; Warren et al., 2020) and/or by KMT-KMT/KMT-non-KMT interactions. The latter are possibly mediated by several MT-associated proteins (Agarwal, 2018). It is also possible that non-KMTs, involved in a k-fiber maturation during mitosis (Maiato et al., 2004), contribute to such stabilization of k-fibers in mammalian cells.

Electron tomography revealed that on average nine KMTs are attached to each kinetochore in HeLa cells in metaphase. This result differs from previous observations in PtK_1 cells (McEwen et al., 1997; O'Toole et al., 2020). In this marsupial cell line, about 20 KMTs were reported to connect to the kinetochores. This difference in the number of attached KMTs could be related to kinetochore size. As previously observed by light microscopy, kinetochores in HeLa cells have about half the size of kinetochores compared to PtK_1 cells (Cherry et al., 1989). Similarly, kinetochore size in PtK_1 cells was 0.157 ± 0.045 µm^2 (mean ± STD;

(McEwen et al., 1998a)) as observed by electron tomography, whereas kinetochores in HeLa cells, as determined indirectly by electron tomography in this study, have an estimated size of about 0.107 ± 0.075 µm^2 (mean ± STD). Possibly, the area of the outer kinetochore might indirectly define the size and/or the number of available free binding sites for MTs (Drpic et al., 2018; Monda and Cheeseman, 2018). Concerning the number of kinetochore-attached MTs, it is interesting to note here that the number of KMTs per k-fiber is not related to the position of these KMTs in the spindles. In fact, central, intermediate and peripheral kinetochores show similar average numbers of attached KMTs. Thus, the peripheral position of k-fibers within the spindle accompanied by an increase in the global tortuosity has no effect on the number of KMTs in the k-fibers.

KMTs in our reconstructed k-fibers are of different lengths, confirming previous observations (McDonald et al., 1992; O'Toole et al., 2020; Sikirzhytski et al., 2014). In fact, many KMTs are relatively short (~20% of KMTs were shorter than 2 µm; **Figure 4A**), and half of the KMT minus ends are not positioned in the defined MT-centrosome interaction area. Per definition, these short KMTs in k-fibers are not directly associated with the spindle poles. Interestingly, only 5% of the analyzed k-fibers show a length distribution in which none of the analyzed KMTs is positioned in the MT-centrosome interaction area (**Figure 5-figure supplement 3**). When analyzing KMTs in the one-cell *C. elegans* embryo, we found that only about 20 % of the KMT minus ends were located within 2 µm of their corresponding mother centriole. This had suggested that the majority of KMTs in *C. elegans* do not contact the centrosomes. In agreement with previously published data (McDonald et al., 1992; O'Toole et al., 2020), our tomographic analysis of mammalian KMTs thus suggests that the k-fibers in HeLa cells mediate a semi-direct connection with the spindle poles, in which at least one KMT of the k-fibers is directly connected to the poles, while the other KMTs of the fiber are indirectly linked to non-KMTs (**Figure 10**). Thus, spindles in nematode embryos and in mammalian cells are similar in that anchoring of KMTs into the spindle network can be observed.

Interestingly, we observed a difference in KMT length and their minus-end distance to the pole in central *versus* peripheral KMTs. Centrally located KMTs were shorter, and their minus ends showed a shorter distance to the mother centriole compared to peripheral KMTs. This difference is most likely related to the roundedness of the mitotic spindles (Taubenberger et al., 2020). To test whether the roundedness of spindles and the organization of KMTs in terms of KMT length and minus-end distribution are directly related, it would be interesting to analyze the organization of KMTs in spindles showing a lower degree of rounding up during mitosis such as PtK$_1$ (McDonald et al., 1992) and RPE-1 cells (O'Toole et al., 2020).

Extending previous knowledge, we have shown that k-fibers in our reconstructions show a remarkable morphological variability, as obvious by a change in the circumference of the k-fibers along their entire length (**Figure 10A-B**). This variability in the circumference of the k-fibers is reflected in an increase in the local tortuosity of KMTs at positions close to the spindle poles. This increase in the tortuosity of KMTs at spindle poles might promote anchoring of the broadened k-fibers with the non-KMT network through MT-MT interactions (**Figure 10C-D**).

Here, we consider the bundled KMTs as the 'core' of the k-fibers (**Figure 10C**). We used the annotated KMTs in our reconstruction to identify other non-KMTs associated with these KMTs. In other words, we annotated the KMTs in the spindles to 'fish out' other non-KMTs out of more than 6000 MTs to identify those non-KMTs that were positioned in the vicinity of reconstructed KMTs. Explicitly, the results obtained from our approach do not exclude models of KMT organization, in which the k-fiber is a tight bundle that continues to the pole with changing composition of KMTs and associated non-KMTs along its length. In this sense, differences in either the length of KMTs or in the loss of KMTs from the k-fiber might simply reflect an MT exchange with the spindle (**Figure 10D**). Our consideration of KMTs as the cores of k-fibers is also not in disagreement with a dynamic change in k-fiber composition during the maturing of those fibers (Begley et al., 2021; Maiato et al., 2004). Unfortunately, our 3D reconstructions can deliver only snapshots of the very dynamic mitotic process.

While both KMTs and non-KMTs show a clear correlation in the number and the average length of associations (**Figure 8** and **Figure 9**), both MT populations show differences in the position of these associations. In contrast to non-KMTs, KMTs show a high tendency to associate with non-KMTs at the spindle poles (**Figure 8F-G**; **Figure 9C-D**). This tendency to interact at spindle poles is independent of the chosen distance of MT interaction. In accord with the previously discussed broadening of the k-fibers at their pole-facing end, our results suggest that KMTs preferably associate with other MTs at the spindle poles. In contrast, non-KMTs show a flat pattern of interaction with other MTs at association distances of 25 and 35 nm. Moreover, an increase in the association distance from 35 nm to 50 nm, shows a higher tendency of non-KMTs to associate with MTs in the center of the spindle, very likely related to the organization of interpolar MTs in the center of the spindle (**Figure 8-figure supplement 1F**; (Kajtez et al., 2016; Mastronarde et al., 1993; Vukušić et al., 2017)). In general, it would be interesting to analyze the organization of these interpolar MTs, the structure of the KMTs in the k-fibers, and also the recognized patterns of MT-MT interaction during other stages of mitosis, for instance at anaphase. Patterns of the interaction of KMTs with non-KMTs might be more obvious during the segregation of the chromosomes.

Implications for models on spindle organization

As previously noted, we have combined our 3D reconstructions with additional live-cell imaging and biophysical modeling in a parallel publication (Conway et al., 2021). Combining data on the length and the position of minus ends of KMTs in spindles (as obtained here by electron microscopy), and the turnover and movement of tubulin in KMTs as generated by light microscopy, a model was proposed in which KMTs predominantly nucleate *de novo* at kinetochores, with KMTs growing towards the spindle poles. A major outcome of this parallel study is that KMTs in spindles grow along the same trajectories as non-KMTs and that both the KMTs and non-KMTs are well aligned throughout the spindle, leading to the assumption that spindles can be considered as active liquid crystals (Brugués and Needleman, 2014;

Oriola et al., 2020). This might apply to both centrosomal mitotic as well as acentrosomal female meiotic spindles (Redemann et al., 2018, 2017). Such liquid crystals can be characterized by the degree of local MT alignment, expressed by the nematic order parameter. Interestingly, the analyzed spindles show a high nematic order parameter $S= 0.81 \pm 0.02$ near the chromosomes, whereas the nematic order parameter $S=0.54 \pm 0.02$ is lower at the spindle poles (Conway et al., 2021). Along this line, KMTs in our electron tomography study are well aligned in the middle of the spindle, while the order of the KMTs in the k-fibers is progressively lost at positions closer to the spindle poles. While KMTs are growing out from the kinetochores towards the centrosomes, the observed broadening of the k-fibers at the spindle poles might be a direct consequence of a change (i.e., a decrease) in the internal structural organization of the spindle trajectories (i.e., the surrounding non-KMTs). In the future, it will be important to analyze k-fibers in other fully 3D-reconstructed mammalian spindles, thus allowing an advancement of the developed model on KMT outgrowth in the context of such well-defined trajectories.

Material and Methods

Key resource table

Reagent type (species) or resource	Designation	Source or reference	Identifiers	Additional information
Strain, background (HeLa, Kyoto)	Gerlich Lab	IMBA, Vienna, Austria	-	-
Software, algorithm	SerialEM Boulder Laboratory for 3-Dimensional Electron Microscopy of cells Colorado, USA	https://bio3d.colorado.edu/SerialEM/	-	-
Software, algorithm	IMOD Boulder Laboratory for 3-Dimensional Electron Microscopy of cells Colorado, USA	http://bio3d.colorado.edu/imod	-	-
Software, algorithm	Amira Thermo Fisher Scientific, USA	Zuse Institute Berlin (ZIB)	-	-
Software, algorithm	ASGA Robert Kiewisz / Müller - Reichert Lab Dresden, Germany	https://github.com/RRobert92/ASGA	-	https://kiewisz.shinyapps.io/ASGA

Software, algorithm	ASGA - 3D Viewer Robert Kiewisz / Müller - Reichert Lab Dresden, Germany	https://github.com/RRobert92/ASGA_3DViewer	-	https://cfci.shinyapps.io/ASGA_3DViewer/

Cell line

For all experiments we have used a HeLa Kyoto cell line obtained from Daniel Gerlich lab (IMBA, Vienna), which was given to the Gerlich lab by S. Narumiya (Kyoto, Japan; RRID: CVCL_1922) and validated using Multiplex Human Cell Line Authentication test (MCA). Furthermore, the HeLa Kyoto cell line was checked for mycoplasma with a PCR test kit. This cell line was not on the list of commonly misidentified cell lines as maintained by the International Cell Line Authentication Committee.

Cultivation of cells

HeLa (Kyoto) cells (Guizetti et al., 2011) were grown in Dulbecco's Modified Eagle's Medium (DMEM) supplemented with 10% fetal bovine serum (FBS) and 100 units/ml of penicillin/streptomycin (Pen/Strep). Flasks were placed in a humidified incubator at 37°C with a supply of 5% CO_2. For electron microscopy, cells in mitosis were enriched by applying the shake-off technique (Kiewisz et al., 2021). Flasks with cell confluency of 60-80% were shaken against the laboratory bench. The medium with detached cells was then collected, centrifuged at 1200 rpm for 3 min at room temperature, and resuspended in 1 ml of pre-warmed DMEM medium.

Electron tomography

Specimen preparation for electron microscopy

Cultures enriched in mitotic HeLa cells were further processed for electron microscopy essentially as described (Guizetti et al., 2011; Kiewisz et al., 2021). Briefly, sapphire discs with a diameter of 6 mm were cleaned in Piranha solution (1:1 H_2SO_4 and H_2O_2, v/v), coated with poly-L-lysine (0.1% in ddH_2O, w/v), and dried for 2 hrs at 60°C. Furthermore, the discs were coated with fibronectin (1:10 dilution in 1x PBS, v/v) for 2 hrs and stored in a humidified incubator until further used. The sapphire discs were then placed into custom-designed 3D-printed incubation chambers (Kiewisz et al., 2021). Subsequently, cells were seeded on the coated sapphire discs and incubated for 10 min in a humidified incubator at 37°C supplied with 5% CO_2. This allowed the mitotic cells to re-attach to the surface of the coated sapphire discs and continue to divide.

High-pressure freezing and freeze substitution

Cells were cryo-immobilized using an EM ICE high-pressure freezer (Leica Microsystems, Austria). For each run of freezing, a type-A aluminum carrier (Wohlwend, Switzerland) with the 100 µm-cavity facing up was placed in the specimen loading device of the EM ICE. The cavity of the type-A carrier was filled with 5 µl of DMEM containing 10% BSA. The carrier was then immediately closed by placing a 6 mm-sapphire disc with attached cells facing down on top of the type-A carrier. Finally, a spacer ring was mounted on top of the closed carrier, and freezing was started. Samples were frozen under high pressure (~2,000 bar) with a cooling rate of ~20,000 °C/s (Reipert et al., 2004). Frozen samples were then opened under liquid nitrogen and transferred to cryo-vials filled with anhydrous acetone containing 1% (w/v) osmium tetroxide (EMS, USA) and 0.1% (w/v) uranyl acetate (Polysciences, USA). Freeze substitution was performed in either a Leica AFS or a Lecia AFS II (Leica Microsystems, Austria). Samples were kept at -90°C for 1 h, warmed up to -30°C with increments of 5 °C/h, kept for 5 hrs at -30°C, and then warmed up to 0°C (increments of 5 °C/h). Finally, samples were allowed to warm up to room temperature. After freeze substitution, samples were washed three times with pure anhydrous acetone and infiltrated with Epon/Araldite (EMS, USA) using increasing concentrations of resin (resin:acetone: 1:3, 1:1, 3:1, then pure resin) for 1 hr each step at room temperature (Muller-Reichert et al., 2003). Samples were infiltrated with pure resin overnight and then embedded by using commercial flow-through chambers (Leica Microsystems, Austria) designed for sapphire discs of a diameter of 6 mm. Samples were polymerized at 60°C for 36 hrs.

Pre-selection of staged cells

To select cells in metaphase, resin-embedded samples were pre-inspected using an Axiolab RE upright brightfield microscope (Zeiss, Germany) with a 5x and a 40x objective lens (Zeiss, Germany). Selected cells in metaphase were sectioned using an EM UC6 ultramicrotome (Leica Microsystems, Austria). Ribbons of semi-thick (~300 nm) serial sections were collected on Formvar-coated copper slot grids, post-stained with 2% (w/v) uranyl acetate in 70% (v/v) methanol, followed by 0.4% (w/v) lead citrate (Science Services, USA) in double-distilled water. In addition, 20 nm-colloidal gold (British Biocell International, UK) was attached to the serial sections, serving as fiducial markers for subsequent electron tomography. The selected cells were then pre-inspected at low magnification (~2900x) using either an EM906 (Zeiss, Germany) or a TECNAI T12 Biotwin (ThermoFisher Scientific, USA) transmission electron microscope operated at either 80 or 120 kV, respectively.

Acquisition and calculation of tomograms

Serial sections of the selected cells were then transferred to a TECNAI F30 transmission electron microscope (ThermoFisher Scientific, USA) operated at 300 kV and equipped with a US1000 CCD camera (Gatan, USA). Using a dual-axis specimen holder (Type 2040, Fishione, USA) tilt series were acquired from -65° to +65° with a 1° increment at a magnification of 4700x and a final pixel size of 2.32 nm applying the SerialEM software package (Mastronarde, 2005, 2003). For double-tilt electron tomography, the grids were rotated for 90 degrees and the second tilt series were acquired using identical microscope settings (Mastronarde, 1997). The tomographic A- and B-stacks were combined using IMOD (Kremer et al., 1996; Mastronarde and Held, 2017). For each spindle reconstruction, montages of 2 × 3 frames were collected. Depending on the orientation of the spindles during the sectioning process, between 22 to 35 serial sections were used to fully reconstruct the volumes of the three selected spindles (**Table 8**).

Segmentation of MTs and stitching of serial tomograms

As previously published (Redemann et al., 2014; Weber et al., 2012), MTs were automatically segmented using the ZIB Amira (Zuse Institute Berlin, Germany) software package (Stalling et al., 2005). After manual correction of MT segmentation, the serial tomograms of each recorded cell were stitched using the segmented MTs as alignment markers (Lindow et al., 2021) Following this pipeline of data acquisition and 3D reconstruction, three complete models of HeLa cells in metaphase were obtained (**Table 8**). As also done in our previous study (Redemann et al., 2017), for all the analyses we discarded MT with one endpoint found at the border of the reconstructed tomogram. These MTs with a high probability were leaving the tomographic volume. The number of these MTs in all dataset account for <1% of all traced MTs and therefore, we do not expect a relevant error in this analysis.

Z-correction of stacked tomograms

Each stack of serial tomograms was expanded in Z to correct for a sample collapse during data acquisition (McEwen and Marko, 1998). We corrected this shrinkage by applying a Z-factor to the stacked tomograms (**Figure 2-figure supplement 2**; (O'Toole et al., 2020)). Taking the microtome setting of 300 nm, we multiplied this value by the number of serial sections. For each spindle, we also determined the thickness of each serial tomogram and then calculated the total thickness of the reconstruction. The Z-factor was then determined by dividing the actual thickness of each stack of tomograms by the total thickness as determined by the microtome setting. Such calculated Z-factors (1.3 for spindle #1, **Figure 1B, C and F**; 1.4 for spindle #2, **Figure 1D and G**; and 1.42 for spindle #3, **Figure 1E and H**) were then applied to our full spindle reconstructions. All quantitative data in this publication are given for the Z-expanded spindles. For comparison, values for the non-expanded spindles are also given in **Table 12** and **Table 13**.

Software packages

We used the ZIB extension of the Amira software (Zuse Institute Berlin, Germany) for further quantitative analyses (Stalling et al., 2005). In addition, an automatic spatial graph analysis (ASGA) software tool was created for the quantification of KMT length and minus-end distribution (Kiewisz and Müller-Reichert, 2021). The ASGA software tool was also used to quantify the position of each k-fiber in the mitotic spindles and determine the tortuosity, the cross-section area, the shape and the density of KMTs in the k-fibers.

Staging of spindles

For staging of the three reconstructed metaphase spindles, we determined the inter-kinetochore distance for each k-fiber pair. More precisely, we analyzed the distance between the paired outer kinetochores. For this, the closest neighboring sister kinetochores were determined. The center of each kinetochore was then defined as a median position of all KMT plus ends associated with each selected kinetochore, and the inter-kinetochore distance was then calculated as the 3D distance between the defined median centers of each kinetochore pair. For each mitotic spindle, the inter-kinetochore distance is given as the mean value (±STD). As an additional criterion for mitotic staging, the pole-to-pole distances were measured. For this, we analyzed the 3D distance between the centers of the manually segmented mother centrioles in each data set. This read-out was used to determine the spindle size at metaphase.

Classification of MTs

MTs with their putative plus end associated with the chromosomes were defined as KMTs (**Figure 2 - figure supplement 2**). Characteristically, these KMTs showed a parallel arrangement at the site of attachment to the chromosomes. Unfortunately, identification of individual kinetochores in our electron tomograms was hindered by the fact that prominent single and electron-dense KMT attachment sites, as described previously for conventionally fixed cells (**McEwen et al., 1998b**), were not always clearly visible after cryo-fixation by high-pressure freezing. All other MTs in our 3D reconstructions were classified as non-KMTs.

MT-centrosome interaction area

For each non-KMT, the end closest to the nearest mother centriole was defined as the minus-end. The absolute distance of each putative non-KMT minus-end to the nearest mother centriole was measured in 3D. The number of the non-KMT minus ends was then plotted against their distance to the pole. We then fit a Gaussian distribution to the peak of the non-KMT minus end density near the spindle pole. The border of spindle poles, termed here the border of the MT-centrosome interaction area, was defined as two-half widths from the peak of a Gaussian distribution fit to the density peak near the poles in the non-KMT minus-end density histogram, which was 1.7 µm from the centrosome.

Position of MT minus ends

To analyze the position of KMT and non-KMT minus ends in the metaphase spindles, two measurements were performed. Firstly, the 3D distance between the nearest mother centriole and the KMT and the non-KMT minus ends for the definition of non-KMT minus ends see above) was determined. Secondly, we determined the relative position of these ends on the pole-to-kinetochore and the pole-to-pole axis. For each KMT minus end, the relative position is given as the normalized position between the mother centriole (position = 0) and the kinetochore (position = 1) and along the spindle axis (**Figure 5-figure supplement 1**). For each non-KMTs minus end, the relative position is given as the normalized position between two spindle poles (Pole_1 = 0, and Pole_2 = 1; **Figure 5A**). The distribution of the relative positions of KMT and non-KMTs ends (mean ± STD) is given for each data set. The number and percentage of KMT and non-KMTs ends not associated with the spindle pole were defined as minus ends detected farther than the calculated MT-centrosome interaction area.

Length distribution of MTs

The full length of each reconstructed KMT and non-KMT was measured, and the average (± STD) is given for each data set. We also analyzed the percentage of short *versus* long KMTs. For each data set, short KMTs were defined as those shorter than 1.7 µm in length. This threshold was chosen based on the MT-centrosome interaction area. The long KMTs were identified as KMTs longer than the half-spindle length for each given data set. Long KMTs were identified as KMTs longer than the half-spindle length for each given data set.

Interaction of KMTs with non-KMTs

KMT minus-end association with other MT lattices was calculated as a 3D distance. For this analysis, KMT minus ends were identified as KMT ends that were closer to one of the spindle poles. Finally, a possible association between KMT ends and other MT lattices was measured by calculating the 3D distance between KMT ends and every MT lattice in the reconstructed spindle. An interaction between KMT minus ends and an MT lattice was identified when KMT minus ends were found within a given interaction distance to any MT lattice. The defined interaction distances were 25, 30, 35, 45, 50, 75 and 100 nm. To account for differences in the density of MTs along the pole-to-pole axis, each KMT interaction was normalized by calculating the local MT density around each KMT end. This was achieved by selecting a voxel of 0.001 μm^3 with the KMT end in its center and calculating the local MT density by dividing the number of potential interactions by the voxel volume. For visualization, each KMT was labeled based on the type of detected interaction with KMTs or non-KMTs. KMTs without any interaction were also labeled. The percentage of KMTs with any interaction was measured and the average value for all data sets is given (mean ± STD).

To identify possible MT minus-end associations with KMT lattices, the 3D distances of the MT minus ends to KMT lattices were calculated. An association between KMT lattices and MT minus ends was detected when MT minus ends were positioned within defined interaction distances to the KMT lattices. We considered the following interaction distances: 25, 30, 35, 45, 50, 75 and 100 nm. In addition, each interaction was normalized by the local MT density, as described above. The percentage of KMTs with any interaction was measured and the average from all datasets is given (mean ± STD). Moreover, to calculate the position of interaction, the relative position of MT minus ends on the pole-to-kinetochore axis was calculated. The relative position of each minus end is given as the normalized position between the kinetochore (position = 1) and mother centriole (position = 0) along the spindle axis.

Defining kinetochore position

To determine the position of each k-fiber in the mitotic spindle, a position model was created that is based on the location of each kinetochore on the metaphase plate. For this, the kinetochores of each spindle were projected in 2D space on the X/Z axis and an ellipse with a semi-major (called a-axis) and a semi-minor axis (called b-axis) was fitted onto all projected kinetochores. The fitted ellipse was then divided into three regions ranging from 0 - 50% (central region), from 50 - 75% (intermediate region), and 75 - 100% (peripheral region). Kinetochores with associated k-fibers were then assigned to these three regions.

Global tortuosity of KMTs

For the analysis of global KMT tortuosity, the ratio of the KMT spline length and the 3D distance between the plus and the minus end for each KMT was measured. The distribution of KMTs tortuosity (mean, ± STD) is given. In addition, the correlation of the tortuosity of KMTs with their length is given as a fitted polynomial line calculated as a local polynomial regression by the locally estimated scatterplot smoothing "loess" method. A confidence interval for the created polynomial line was calculated with the t-based approximation, which is defined as the overall uncertainty of how the fitted polynomial line fits the population of all data points. Local polynomial regressions and confidence intervals for all data sets were calculated using the stat 4.0.3 R library (R Core Team, 2021).

Local tortuosity of KMTs

For the calculation of the local tortuosity, each KMT was subsampled with segments of a length of 500 nm. Both the tortuosity and the relative position along the pole-to-kinetochore axis were measured for each segment. In addition, the correlation of local KMT tortuosity against the relative position is given. Local polynomial regressions and confidence intervals for all data sets were calculated using the stat 4.0.3 R library (R Core Team, 2021).

The polygonal cross-section area of k-fibers

The cross-section area was calculated every 500 nm along each k-fiber. For each defined k-fiber cross-section, the KMT positions were mapped on a 2D plane, and the polygonal shape of the k-fiber cross-sections was calculated based on the position of the KMTs. The polygonal shape was calculated with the alpha shape algorithm ($\alpha = 10$) using the "ashape3d" function of the alphashape3d 1.3.1 R library (**Lafarge and Pateiro-Lopez, 2020**). The alpha shape is the polygon shape formed around a given set of points (KMTs from a cross-section) created by a carving space around those points with a circle of a radius defined as α. The polygonal shape was then built by drawing outline polygon lines between contact points on the fitted circle. In order to calculate the polygonal area from the polygon shape of the k-fiber cross-section, a polygonal prism was created by duplicating and shifting a polygonal shape 1 µm in the X/Y/Z dimension. This creates a prism with a height of 1 µm. The volume of the created 3D object (prism) was then calculated with alphashape3d 1.3.1 R library (Lafarge and Pateiro-Lopez, 2020) and from this, a polygonal area could be calculated by dividing the prism volume (V_{pp}) by prism high ($h_{pp} = 1$ µm). The distribution of the k-fiber polygonal area along the pole-to-kinetochore axis is given as a fitted polynomial line of local polynomial regression using the "loess" method. Confidence intervals were calculated with the t-based approximation using the stat 4.0.3 R library (R Core Team, 2021).

Density of KMTs in k-fibers

The density of KMTs in the k-fibers was calculated in segments of 500 nm length along the entire path of each fiber. To determine the percentage of KMTs that were enclosed in the k-fiber for each cross-section, the number of KMTs enclosed in the given k-fiber section and the circular area were determined. The radius of the circular area was calculated for each k-fiber at the position of the KMTs attached to the kinetochores. The distribution of the k-fiber density along the pole-to-pole axis is given as a fitted polynomial line and a confidence interval calculated with the t-based approximation using the stat 4.0.3 R library (R Core Team, 2021).

Analysis of KMT-KMT distances

The KMT-KMT distances at a given k-fiber cross-section were selected by a K-nearest neighbor estimation. An estimation was achieved by calculating a distance matrix between all selected KMTs. Each KMT-KMT connection was ranked according to its distance. Finally, for each KMT in a k-fiber, neighboring KMTs were selected by picking KMTs with k=1. For each k-fiber, the mean KMT-KMT distance and the standard deviation were calculated.

Interaction of MTs

The interaction between MTs was calculated in steps of 20 nm along each MT. For each MT segment, the distance to a neighboring MT was calculated. In addition, the length of interaction was analyzed for each detected MT-MT interaction. The length of interaction between MTs was calculated as a sum of the 20-nm segments. This analysis was performed for defined interaction distances of 25, 30, 35, 45 and 50 nm. The frequency plots for the average number of interactions per MT and the average length of interaction length are given for each interaction distance. Each MT segment is labeled based on the number of interactions.

Error analysis

For the tracing of MTs, the error associated with our approach was previously analyzed for the 3D reconstructions of mitotic centrosomes in the early *C. elegans* embryo using serial semi-thick plastic sections (**Weber et al., 2012**). Although the data on mammalian spindles is larger, the tomogram content of this current study is similar to the published centrosome data sets, and thus we assume that the error MT tracing lies in the same range of 5–10%. All traced MTs were manually verified. This was achieved by using the ‘filament editor’ tool in the ZIB extension of the Amira software that allowed us to create a flattened overview of the entire MT track, which was instrumental for quick validation of each MT. Both false-positive and negative tracings were corrected.

However, it is more difficult to estimate the error of the matching algorithm. Our standardized automatic stitching method has been described in detail in previous publications (Lindow et al., 2021; Redemann et al., 2014; Weber et al., 2012). In general, the stitching depends on the local density and properties of the MTs. For this reason, the stitched MTs were manually verified and corrected (Lindow et al., 2021). In particular, all KMTs in our reconstructions were checked for correct stitching across section borders. Examples of correct stitching of MTs at section borders are given in **Figure 3-figure supplement 1**. The quality of the analysis of the MTs, especially the KMTs, should therefore be influenced by minor errors. In our previous publications (Redemann et al., 2014; Weber et al., 2012), we estimated the overall quality of the stitching by analyzing the distribution of MT endpoints in the Z-direction (i.e., normal to the plane of the slice). We expect to find approximately the same density of MT endpoints along the Z-direction of each serial-section tomogram. This distribution is visualized in the *Serial Section Aligner* tool previously presented (Lindow et al., 2021). Therefore, if the density of endpoints after matching is approximately the same along the Z-direction of the serial-section tomograms, we can assume that the number of artificial points that have been introduced at the interfaces of the serial sections are negligible. This was visualized by projecting each spindle along the Y/Z axis (**Figure 3 - figure supplement 1**).

Custom-designed software for the visualization of 3D data

For better visualization of the 3D organization of KMTs in k-fibers, a platform was developed using the WebGL library (rgl 0.106.8 R library; (Adler et al., 2021)). This platform was implemented for the public and will allow readers to choose data sets from this publication for interactive visualization of selected spindle features. For instance, users may choose to visualize the organization of k-fibers or KMTs and select for the analysis of MT-MT interactions. For an analysis of KMTs, users can select the following features of analysis such as length distribution, minus-end positioning, curvature, and number at the kinetochore. For the MT-MT interaction analysis, users can select different interaction distances. This platform is designed for the continuous addition of 3D reconstructions of spindles obtained from different systems and can be accessed as follows: https://cfci.shinyapps.io/ASGA_3DViewer/.

Data availability

Tomographic data before and after the z-expansion has been uploaded to the TU Dresden Open Access Repository and Archive system (OpARA) and is available as open access:

http://doi.org/10.25532/OPARA-128

We released all datasets in Amira format. The tomographic data are also available in tiff format, which can be opened either with the ImageJ Fiji (Schindelin et al., 2012) or the IMOD (Kremer et al., 1996) open-source software packages. The MT-track files containing information about the segmented MTs were released in binary and ASCII format. To make this task easier for interested readers, the ASGA (Kiewisz and Müller-Reichert, 2021) open-source software, which is part of this publication, is supplied with small scripts written in R language, which allows users to read the ASCII format into an array.

https://github.com/RRobert92/ASGA/blob/main/R/bin/Utility/Load_Amira.R

The code used to perform quantitative analysis and visualization of MT organization in spindles has been uploaded to the GitHub repository and is available as open access under the GPL v3.0 license:

https://github.com/RRobert92/ASGA; https://github.com/RRobert92/ASGA_3DViewer

The supplementary high-resolution videos have also been uploaded to YouTube. I These movies can be found at this URL:

https://youtube.com/playlist?list=PL-L6a60L11laVrVBFZqGi0wmULXD1b4Px

Acknowledgments

The authors would like to thank Dr. Tobias Fürstenhaupt (Electron Microscopy Facility at the MPI-CBG, Dresden, Germany) for technical support. We are also grateful to Drs. Reza Farhadifar, Stefanie Redemann, Alejandra Laguillo Diego and Isabelle Vernos for a critical reading of the manuscript. We also would like to thank Felix Herter for implementing a module in the ZIB extension of Amira that we used in this paper for visualizing different cross-section plains of KMT ends. Research in the Müller-Reichert laboratory is supported by funds from the Deutsche Forschungsgemeinschaft (MU 1423/8-2). R.K. received funding from the European Union's Horizon 2020 research and innovation program under the Marie Skłodowska-Curie grant agreement No. 675737 (grant to T.M.R.). This work was supported by the NSF-Simons Center for Mathematical and Statistical Analysis of Biology at Harvard (award number #1764269), and the Harvard Quantitative Biology Initiative.

Declaration of interests

The authors declare no competing financial interests.

References

Adler D, Murdoch D, Nenadic O, Urbanek S, Chen M, Gebhardt A, Bolker B, Csardi G, Srzelecki A, Senger A. 2021. RGL - 3D visualization device system for R using OpenGL.

Agarwal PK. 2018. Public Administration Challenges in the World of AI and Bots. *Public Administration Review* **78**:917–921. doi:10.1111/puar.12979

Almeida AC, Oliveira J, Drpic D, Cheeseman LP, Damas J, Lewin HA, Larkin DM, Aguiar P, Pereira AJ, Maiato H. 2021. Kinetochore-mediated microtubule assembly and Augmin-dependent amplification drive k-fiber maturation in mammals Condensed title: Mechanism of mammalian kinetochore fiber maturation. *bioRxiv*. doi:10.1101/2021.08.18.456780

Amos LA. 1989. Brain dynein crossbridges microtubules into bundles. *Journal of Cell Science* **93**:19–28.

Anjur-Dietrich MI, Kelleher CP, Needleman DJ. 2021. Mechanical Mechanisms of Chromosome Segregation. *Cells* **10**:465. doi:10.3390/cells10020465

Begley MA, Solon AL, Davis EM, Sherrill MG, Ohi R, Elting MW. 2021. K-fiber bundles in the mitotic spindle are mechanically reinforced by Kif15. *Molecular Biology of the Cell* **32**:2020.05.19.104661. doi:10.1091/mbc.E20-06-0426

Bougé A-L, Parmentier M-L. 2016. Tau excess impairs mitosis and kinesin-5 function, leading to aneuploidy and cell death. *Disease Models & Mechanisms*. doi:10.1242/dmm.022558

Brinkley BR, Cartwright J. 1975. COLD-LABILE AND COLD-STABLE MICROTUBULES IN THE MITOTIC SPINDLE OF MAMMALIAN CELLS. *Ann N Y Acad Sci* **253**:428–439. doi:10.1111/j.1749-6632.1975.tb19218.x

Brugués J, Needleman D. 2014. Physical basis of spindle self-organization. *Proceedings of the National Academy of Sciences* **111**:18496–18500. doi:10.1073/pnas.1409404111

Burbank KS, Mitchison TJ, Fisher DS. 2007. Slide-and-Cluster Models for Spindle Assembly. *Current Biology* **17**:1373–1383. doi:10.1016/j.cub.2007.07.058

Cherry LM, Faulkner AJ, Grossberg LA, Balczon R. 1989. Kinetochore size variation in mammalian chromosomes: an image analysis study with evolutionary implications. *J Cell Sci* **92**:281–289.

Conway W, Kiewisz R, Fabig G, Kelleher, Colm, Wu, Hai-Yin, Anjur-Dietrich, Maya, Mu□ller-Reichert T, Needleman DJ. 2021. Self-organization of kinetochore-fibers in human mitotic spindles. *bioRxiv*.

DeLuca JG, Gall WE, Ciferri C, Cimini D, Musacchio A, Salmon ED. 2006. Kinetochore Microtubule Dynamics and Attachment Stability Are Regulated by Hec1. *Cell* **127**:969–982. doi:10.1016/j.cell.2006.09.047

Drpic D, Almeida AC, Aguiar P, Renda F, Damas J, Lewin HA, Larkin DM, Khodjakov A, Maiato H. 2018. Chromosome Segregation Is Biased by Kinetochore Size. *Current Biology* **28**:1344-1356.e5. doi:10.1016/j.cub.2018.03.023

Dumont S, Mitchison TJ. 2009. Force and Length in the Mitotic Spindle. *Current Biology* **19**:749–761. doi:10.1016/j.cub.2009.07.028

Fabig G, Kiewisz R, Lindow N, Powers JA, Cota V, Quintanilla LJ, Brugués J, Prohaska S, Chu DS, Müller-Reichert T. 2020. Male meiotic spindle features that efficiently segregate paired and lagging chromosomes. *Elife* **9**. doi:10.7554/eLife.50988

Falnikar A, Tole S, Baas PW. 2011. Kinesin-5, a mitotic microtubule-associated motor protein, modulates neuronal migration. *Molecular Biology of the Cell* **22**:1561–1574. doi:10.1091/mbc.e10-11-0905

Farhadifar R, Yu C-H, Fabig G, Wu H-Y, Stein DB, Rockman M, Müller-Reichert T, Shelley MJ, Needleman DJ. 2020. Stoichiometric interactions explain spindle dynamics and scaling across 100 million years of nematode evolution. *Elife* **9**:1–26. doi:10.7554/eLife.55877

Flemming W. 1879. Beitrage zur Kenntniss der Zelle und ihrer Lebenserscheinungen. *Archiv für Mikroskopische Anatomie* **16**:302–436. doi:10.1007/BF02956386

Godek KM, Kabeche L, Compton DA. 2015. Regulation of kinetochore–microtubule attachments through homeostatic control during mitosis. *Nature Reviews Molecular Cell Biology* **16**:57–64. doi:10.1038/nrm3916

Guizetti J, Schermelleh L, Mäntler J, Maar S, Poser I, Leonhardt H, Müller-Reichert T, Gerlich DW. 2011. Cortical Constriction During Abscission Involves Helices of ESCRT-III–Dependent Filaments. *Science (1979)* **331**:1616–1620. doi:10.1126/science.1201847

Hoffman DP, Shtengel G, Xu CS, Campbell KR, Freeman M, Wang L, Milkie DE, Pasolli HA, Iyer N, Bogovic JA, Stabley DR, Shirinifard A, Pang S, Peale D, Schaefer K, Pomp W, Chang C-L, Lippincott-Schwartz J, Kirchhausen T, Solecki DJ, Betzig E, Hess HF. 2020. Correlative three-dimensional super-resolution and block-face electron microscopy of whole vitreously frozen cells. *Science (1979)* **367**. doi:10.1126/science.aaz5357

Inoué S. 1953. Polarization optical studies of the mitotic spindle. *Chromosoma* **5**:487–500. doi:10.1007/BF01271498

Inoué S, Salmon ED. 1995. Force Generation by Microtubule Assembly/Disassembly in Mitosis and Related Movements. *Molecular Biology of the Cell* **6**:1619–1640. doi:10.1091/mbc.6.12.1619

Kajtez J, Solomatina A, Novak M, Polak B, Vukušić K, Rüdiger J, Cojoc G, Milas A, Šumanovac Šestak I, Risteski P, Tavano F, Klemm AH, Roscioli E, Welburn J, Cimini D, Glunčić M, Pavin N, Tolić IM. 2016. Overlap microtubules link sister k-fibres and balance the forces on bi-oriented kinetochores. *Nature Communications* **7**:10298. doi:10.1038/ncomms10298

Kellogg EH, Howes S, Ti S-C, Ramírez-Aportela E, Kapoor TM, Chacón P, Nogales E. 2016. Near-atomic cryo-EM structure of PRC1 bound to the microtubule. *Proceedings of the National Academy of Sciences* **113**:9430–9439. doi:10.1073/pnas.1609903113

Khodjakov A, Cole RW, McEwen BF, Buttle KF, Rieder CL. 1997. Chromosome Fragments Possessing Only One Kinetochore Can Congress to the Spindle Equator. *Journal of Cell Biology* **136**:229–240. doi:10.1083/jcb.136.2.229

Kiewisz R, Müller-Reichert T. 2021. Automatic Spatial-Graph Analysis (ASGA). doi:https://doi.org/10.5281/zenodo.3732108

Kiewisz R, Müller-Reichert T, Fabig G. 2021. High-throughput screening of mitotic mammalian cells for electron microscopy using classic histological dyes In: Müller-Reichert T, Verkade P, editors. Methods in Cell Biology:Correlative Light and Electron Microscopy IV. New Jersey: Academic Press Inc. pp. 151–170. doi:10.1016/bs.mcb.2020.08.005

Kremer JR, Mastronarde DN, McIntosh JR. 1996. Computer Visualization of Three-Dimensional Image Data Using IMOD. *Journal of Structural Biology* **116**:71–76. doi:10.1006/jsbi.1996.0013

Kuhn J, Dumont S. 2019. Mammalian kinetochores count attached microtubules in a sensitive and switch-like manner. *Journal of Cell Biology* **218**:3583–3596. doi:10.1083/jcb.201902105

Lafarge T, Pateiro-Lopez B. 2020. alphashape3d: Implementation of the 3D Alpha-Shape for the Reconstruction of 3D Sets from a Point Cloud.

Lindow N, Brünig FN, Dercksen VJ, Fabig G, Kiewisz R, Redemann S, Müller-Reichert T, Prohaska S, Baum D. 2021. Semi-automatic stitching of filamentous structures in image stacks from serial-section electron tomography. *Journal of Microscopy* **284**:25–44. doi:10.1111/jmi.13039

Loiodice I, Janson M, Tavormina P, Schaub S, Bhatt D, Cochran R, Czupryna J, Fu C, Tran P. 2019. Quantifying Tubulin Concentration and Microtubule Number Throughout the Fission Yeast Cell Cycle. *Biomolecules* **9**:86. doi:10.3390/biom9030086

Long AF, Suresh P, Dumont S. 2020. Individual kinetochore-fibers locally dissipate force to maintain robust mammalian spindle structure. *Journal of Cell Biology* **219**:1–13. doi:10.1083/jcb.201911090

Luther PK, Lawrence MC, Crowther RA. 1988. A method for monitoring the collapse of plastic sections as a function of electron dose. *Ultramicroscopy* **24**:7–18. doi:10.1016/0304-3991(88)90322-1

Maiato H, Rieder CL, Khodjakov A. 2004. Kinetochore-driven formation of kinetochore fibers contributes to spindle assembly during animal mitosis. *Journal of Cell Biology* **167**:831–840. doi:10.1083/jcb.200407090

Mastronarde DN. 2005. Automated electron microscope tomography using robust prediction of specimen movements. *Journal of Structural Biology* **152**:36–51. doi:10.1016/j.jsb.2005.07.007

Mastronarde DN. 2003. SerialEM: A Program for Automated Tilt Series Acquisition on Tecnai Microscopes Using Prediction of Specimen Position. *Microscopy and Microanalysis* **9**:1182–1183. doi:10.1017/S1431927603445911

Mastronarde DN, Held SR. 2017. Automated tilt series alignment and tomographic reconstruction in IMOD. *Journal of Structural Biology* **197**:102–113. doi:10.1016/j.jsb.2016.07.011

Mastronarde DN, McDonald KL, Ding R, McIntosh JR. 1993. Interpolar spindle microtubules in PTK cells. *Journal of Cell Biology* **123**:1475–1489. doi:10.1083/jcb.123.6.1475

McDonald KL, O'Toole ET, Mastronarde DN, McIntosh JR. 1992. Kinetochore microtubules in PTK cells. *Journal of Cell Biology* **118**:369–383. doi:10.1083/jcb.118.2.369

McEwen BF, Ding Y, Heagle AB. 1998a. Relevance of kinetochore size and microtubule-binding capacity for stable chromosome attachment during mitosis in PtK1 cells. *Chromosome Research* **6**:123–132. doi:10.1023/A:1009239013215

McEwen BF, Heagle AB, Cassels GO, Buttle KF, Rieder CL. 1997. Kinetochore Fiber Maturation in PtK1 Cells and Its Implications for the Mechanisms of Chromosome Congression and Anaphase Onset. *Journal of Cell Biology* **137**:1567–1580. doi:10.1083/jcb.137.7.1567

McEwen BF, Hsieh C-E, Mattheyses AL, Rieder CL. 1998b. A new look at kinetochore structure in vertebrate somatic cells using high-pressure freezing and freeze substitution. *Chromosoma* **107**:366–375. doi:10.1007/s004120050320

McEwen BF, Marko M. 1998. Chapter 5 Three-Dimensional Transmission Electron Microscopy and Its Application to Mitosis Research. pp. 81–111. doi:10.1016/S0091-679X(08)61976-7

McIntosh JR, O'Toole E, Zhudenkov K, Morphew M, Schwartz C, Ataullakhanov FI, Grishchuk EL. 2013. Conserved and divergent features of kinetochores and spindle microtubule ends from five species. *Journal of Cell Biology* **200**:459–474. doi:10.1083/jcb.201209154

Metzner R. 1894. Beitrage zur Granulalehre. I. Kern und kerntheilung. *Arch Anat Physiol* 309–348.

Mitchison T, Kirschner M. 1984. Dynamic instability of microtubule growth. *Nature* **312**:237–242. doi:10.1038/312237a0

Moens P. 1979. Kinetochore microtubule numbers of different sized chromosomes. *Journal of Cell Biology* **83**:556–561. doi:10.1083/jcb.83.3.556

Mollinari C, Kleman J-P, Jiang W, Schoehn G, Hunter T, Margolis RL. 2002. PRC1 is a microtubule binding and bundling protein essential to maintain the mitotic spindle midzone. *Journal of Cell Biology* **157**:1175–1186. doi:10.1083/jcb.200111052

Molodtsov MI, Mieck C, Dobbelaere J, Dammermann A, Westermann S, Vaziri A. 2016. A Force-Induced Directional Switch of a Molecular Motor Enables Parallel Microtubule Bundle Formation. *Cell* **167**:539-552.e14. doi:10.1016/j.cell.2016.09.029

Monda JK, Cheeseman IM. 2018. The kinetochore–microtubule interface at a glance. *Journal of Cell Science* **131**. doi:10.1242/jcs.214577

Muller-Reichert T, Hohenberg H, O'Toole ET, Mcdonald K. 2003. Cryoimmobilization and three-dimensional visualization of C. elegans ultrastructure. *Journal of Microscopy* **212**:71–80. doi:10.1046/j.1365-2818.2003.01250.x

Musacchio A, Desai A. 2017. A Molecular View of Kinetochore Assembly and Function. *Biology (Basel)* **6**:5. doi:10.3390/biology6010005

Nixon FM, Gutiérrez-Caballero C, Hood FE, Booth DG, Prior IA, Royle SJ. 2015. The mesh is a network of microtubule connectors that stabilizes individual kinetochore fibers of the mitotic spindle. *Elife* **4**:1–21. doi:10.7554/eLife.07635

Nixon FM, Honnor TR, Clarke NI, Starling GP, Beckett AJ, Johansen AM, Brettschneider JA, Prior IA, Royle SJ. 2017. Microtubule organization within mitotic spindles revealed by serial block face scanning EM and image analysis. *Journal of Cell Science* **130**:1845–1855. doi:10.1242/jcs.203877

Novak M, Polak B, Simunić J, Boban Z, Kuzmić B, Thomae AW, Tolić IM, Pavin N. 2018. The mitotic spindle is chiral due to torques within microtubule bundles. *Nature Communications* **9**:1–10. doi:10.1038/s41467-018-06005-7

Oriola D, Jülicher F, Brugués J. 2020. Active forces shape the metaphase spindle through a mechanical instability. *Proceedings of the National Academy of Sciences* **117**:16154–16159. doi:10.1073/pnas.2002446117

Oriola D, Needleman DJ, Brugués J. 2018. The Physics of the Metaphase Spindle. *Annual Review of Biophysics* **47**:655–673. doi:10.1146/annurev-biophys-060414-034107

O'Toole E, Morphew M, McIntosh JR. 2020. Electron tomography reveals aspects of spindle structure important for mechanical stability at metaphase. *Molecular Biology of the Cell* **31**:184–195. doi:10.1091/MBC.E19-07-0405)

O'Toole ET, McDonald KL, Mäntler J, McIntosh JR, Hyman AA, Müller-Reichert T. 2003. Morphologically distinct microtubule ends in the mitotic centrosome of Caenorhabditis elegans. *Journal of Cell Biology* **163**:451–456. doi:10.1083/jcb.200304035

Prosser SL, Pelletier L. 2017. Mitotic spindle assembly in animal cells: A fine balancing act. *Nature Reviews Molecular Cell Biology*. doi:10.1038/nrm.2016.162

R Core Team. 2021. R: A language and environment for statistical computing. R Foundation for Statistical Computing.

Redemann S, Baumgart J, Lindow N, Shelley M, Nazockdast E, Kratz A, Prohaska S, Brugués J, Fürthauer S, Müller-Reichert T. 2017. C. elegans chromosomes connect to centrosomes by anchoring into the spindle network. *Nature Communications* **8**:15288. doi:10.1038/ncomms15288

Redemann S, Lantzsch I, Lindow N, Prohaska S, Srayko M, Müller-Reichert T. 2018. A Switch in Microtubule Orientation during C. elegans Meiosis. *Current Biology* **28**:2991–2997. doi:10.1016/j.cub.2018.07.012

Redemann S, Weber B, Möller M, Verbavatz J-M, Hyman AA, Baum D, Prohaska S, Müller-Reichert T. 2014. The Segmentation of Microtubules in Electron Tomograms Using Amira In: Sharp DJ, editor. Mitosis: Methods and Protocols, Methods in Molecular Biology. New York: Springer Science+ Business Media. pp. 261–278. doi:10.1007/978-1-4939-0329-0_12

Redwine WB, Hernández-López R, Zou S, Huang J, Reck-Peterson SL, Leschziner AE. 2012. Structural Basis for Microtubule Binding and Release by Dynein. *Science (1979)* **337**:1532–1536. doi:10.1126/science.1224151

Reipert S, Fischer I, Wiche G. 2004. High-pressure freezing of epithelial cells on sapphire coverslips. *Journal of Microscopy* **213**:81–85. doi:10.1111/j.1365-2818.2004.01260.x

Rieder CL. 1981. The structure of the cold-stable kinetochore fiber in metaphase PtK1 cells. *Chromosoma* **84**:145–158. doi:10.1007/BF00293368

Rieder CL, Salmon ED. 1998. The vertebrate cell kinetochore and its roles during mitosis. *Trends Cell Biol* **8**:310.

Ris H, Witt PL. 1981. Structure of the mammalian kinetochore. *Chromosoma* **82**:153–170. doi:10.1007/BF00286101

Rosselló C, Lindström L, Eklund G, Corvaisier M, Kristensson M. 2018. γ-Tubulin–γ-Tubulin Interactions as the Basis for the Formation of a Meshwork. *International Journal of Molecular Sciences* **19**:3245. doi:10.3390/ijms19103245

Schmidt WJ. 1939. Doppelbrechung der Kernspindel und Zugfasertheorie der Chromosomenbewegung. *Chromosoma* **1**:253–264. doi:10.1007/BF01271634

Sikirzhytski V, Magidson V, Steinman JB, He J, le Berre M, Tikhonenko I, Ault JG, McEwen BF, Chen JK, Sui H, Piel M, Kapoor TM, Khodjakov A. 2014. Direct kinetochore–spindle pole connections are not required for chromosome segregation. *Journal of Cell Biology* **206**:231–243. doi:10.1083/jcb.201401090

Stalling D, Westerhoff M, Hege H-C. 2005. Amira: a Highly Interactive System for Visual Data Analysis In: Hansen CD, Johnson CR, editors. The Visualization Handbook. Elsevier. pp. 749–767.

Taubenberger A v., Baum B, Matthews HK. 2020. The Mechanics of Mitotic Cell Rounding. *Frontiers in Cell and Developmental Biology* **8**. doi:10.3389/fcell.2020.00687

Ustinova K, Novakova Z, Saito M, Meleshin M, Mikesova J, Kutil Z, Baranova P, Havlinova B, Schutkowski M, Matthias P, Barinka C. 2020. The disordered N-terminus of HDAC6 is a microtubule-binding domain critical for efficient tubulin deacetylation. *Journal of Biological Chemistry* **295**:2614–2628. doi:10.1074/jbc.RA119.011243

Vukušić K, Buđa R, Bosilj A, Milas A, Pavin N, Tolić IM. 2017. Microtubule Sliding within the Bridging Fiber Pushes Kinetochore Fibers Apart to Segregate Chromosomes. *Developmental Cell* **43**:11-23.e6. doi:10.1016/j.devcel.2017.09.010

Warren JD, Orr B, Compton DA. 2020. A comparative analysis of methods to measure kinetochore-microtubule attachment stability. pp. 91–116. doi:10.1016/bs.mcb.2020.01.004

Weber B, Greenan G, Prohaska S, Baum D, Hege H-C, Müller-Reichert T, Hyman AA, Verbavatz J-M. 2012. Automated tracing of microtubules in electron tomograms of plastic embedded samples of Caenorhabditis elegans embryos. *Journal of Structural Biology* **178**:129–138. doi:10.1016/j.jsb.2011.12.004

Winey M, Mamay CL, O'Toole ET, Mastronarde DN, Giddings TH, McDonald KL, McIntosh JR. 1995. Three-dimensional ultrastructural analysis of the Saccharomyces cerevisiae mitotic spindle. *Journal of Cell Biology* **129**:1601–1615. doi:10.1083/jcb.129.6.1601

Yu C-H, Redemann S, Wu H-Y, Kiewisz R, Yoo TY, Conway W, Farhadifar R, Müller-Reichert T, Needleman D. 2019. Central-spindle microtubules are strongly coupled to chromosomes during both anaphase A and anaphase B. *Molecular Biology of the Cell* **30**:2503–2514. doi:10.1091/mbc.E19-01-0074

Figures

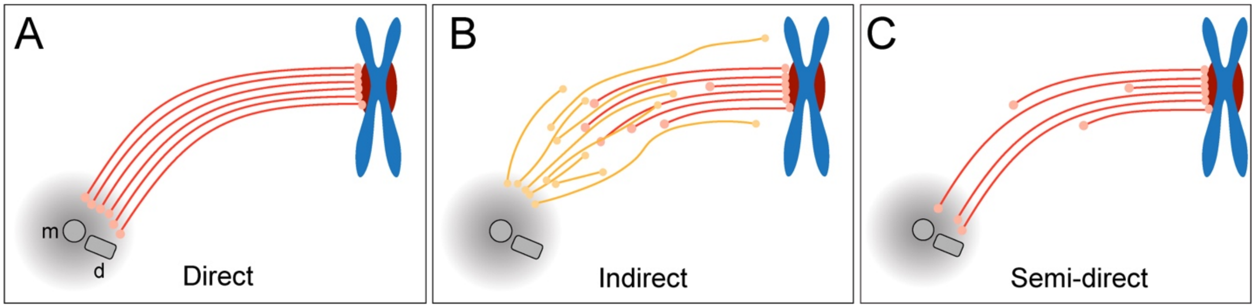

Figure 1. Models of k-fiber organization in mammalian mitosis

(**A**) Direct connection with KMTs (red lines) spanning the distance between the kinetochore and the spindle pole. Chromosomes are shown in blue with kinetochores in red. The mother (m) and the daughter centriole (d) of the spindle pole are indicated. All KMTs are assumed to have similar lengths. (**B**) Indirect connection showing KMTs linking the kinetochore and the spindle pole by association with non-KMTs (yellow lines). K-fibers in this model are composed of KMTs with different lengths, and none of the KMTs is directly associated with the spindle pole. (**C**) Semi-direct connection showing KMTs of different lengths. Some KMTs are directly associated with the spindle pole, while others are not. In this model, KMTs show a difference in length.

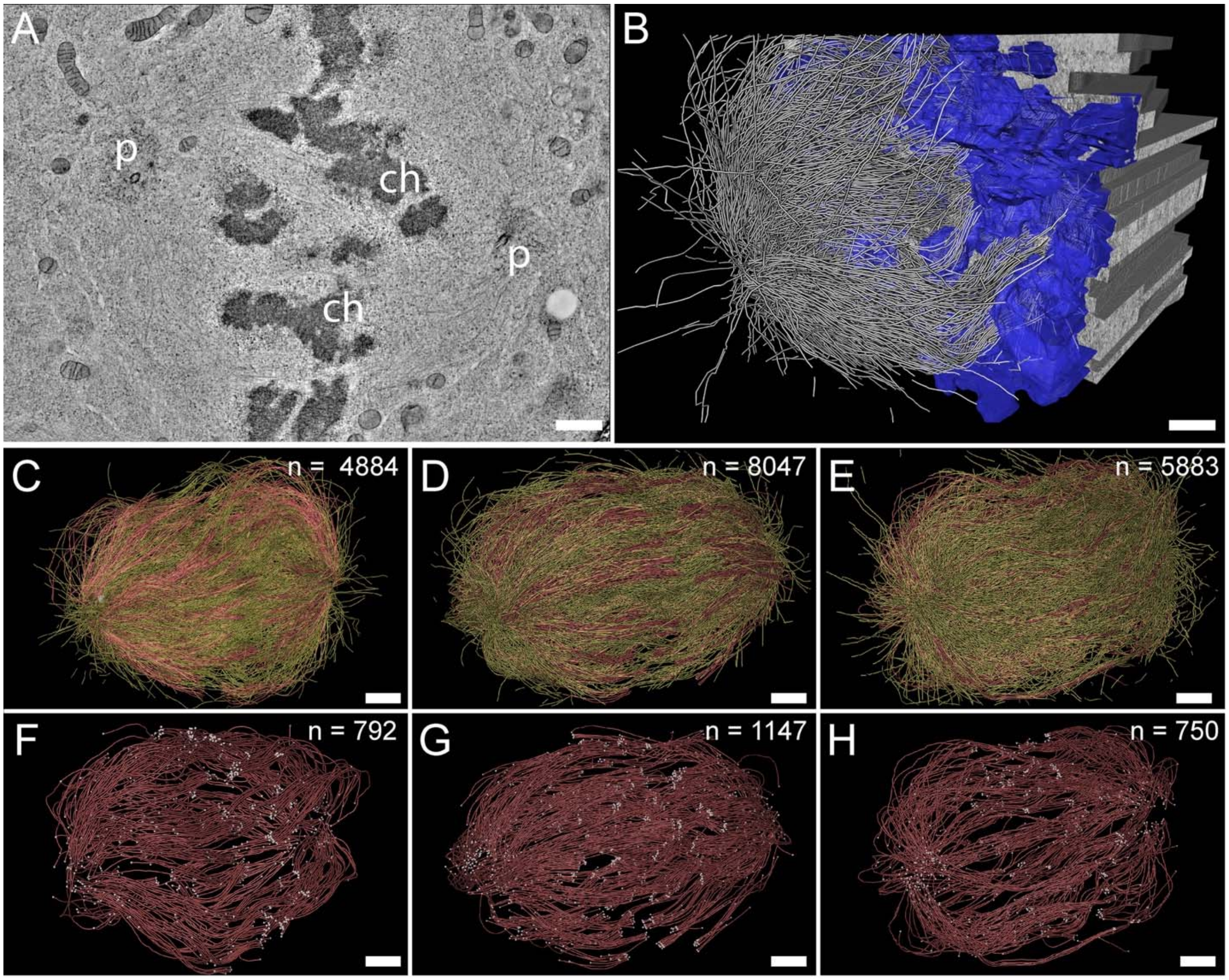

Figure 2. Three-dimensional reconstruction of metaphase spindles by large-scale electron tomography

(**A**) Tomographic slice showing a HeLa cell (spindle #1) in metaphase. The chromosomes (ch) and the spindle poles (p) are indicated. (**B**) Three-dimensional reconstruction of the same spindle as shown in A. The stacking of the serial tomograms used to generate a three-dimensional model of the spindle with the MTs (white lines) is visualized. The segmented chromosomes are shown in blue. (**C**) Three-dimensional model of the spindle as shown in A. The total number of all MTs is given in the upper right corner. The non-KMTs (yellow lines) and KMTs (red lines) are shown. (**D**) Full 3D model of metaphase spindle #2. (**E**) Full 3D model of metaphase spindle #3. (**F**) Extraction of KMTs from the 3D reconstruction as shown in C. The number of KMTs is given in the upper right corner. (**G**) KMTs extracted from spindle #2. (**H**) KMTs extracted from spindle #3. Scale bars, 1 µm.

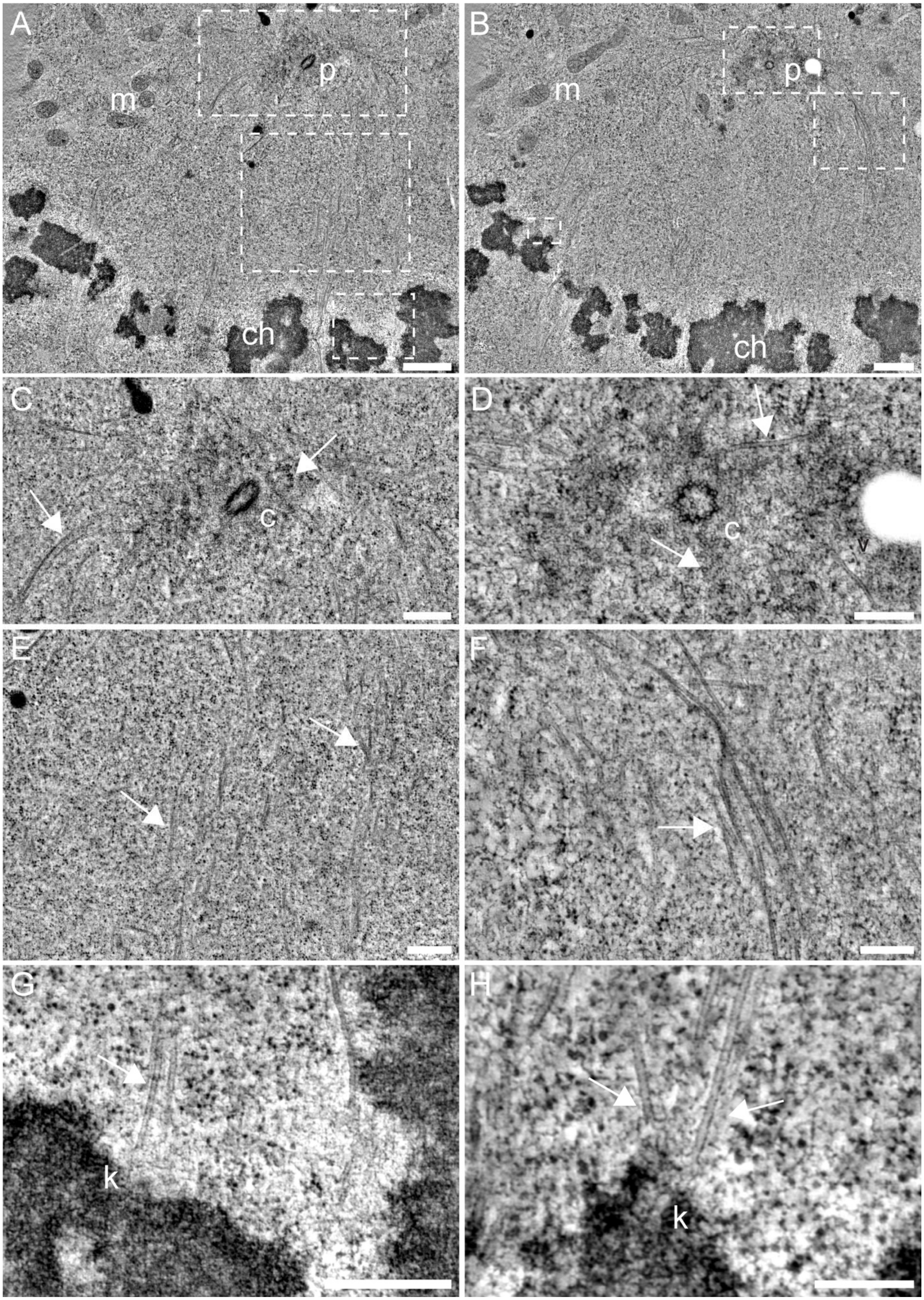

1075

Figure 2-figure supplement 1. Illustration of metaphase in HeLa cells

(**A-B**) Tomographic slices through spindle #3 illustrate the metaphase morphology in HeLa cells. Spindle poles (p) with a centriole, chromosomes (ch), and mitochondria (m) are indicated. The boxed regions (from top to bottom) show a spindle pole, MTs in between the spindle pole and the chromosomes, and a kinetochore region with attached KMTs. Scale bars, 500 nm. (**C-D**) Tomographic slices showing the centrioles (c) and MTs (white arrows) at higher magnification (corresponds to the top boxes in A-B). Scale bars, 250 nm. (**E-F**) Region of the cell between the spindle pole and the chromosomes. MTs (white arrows) are marked (corresponds to the mid boxes in A-B). Scale bars, 250 nm. (**G-H**) Kinetochores (k) with associated KMTs (marked by arrows) are shown (corresponds to the bottom boxes in A-B). Scale bars, 250 nm.

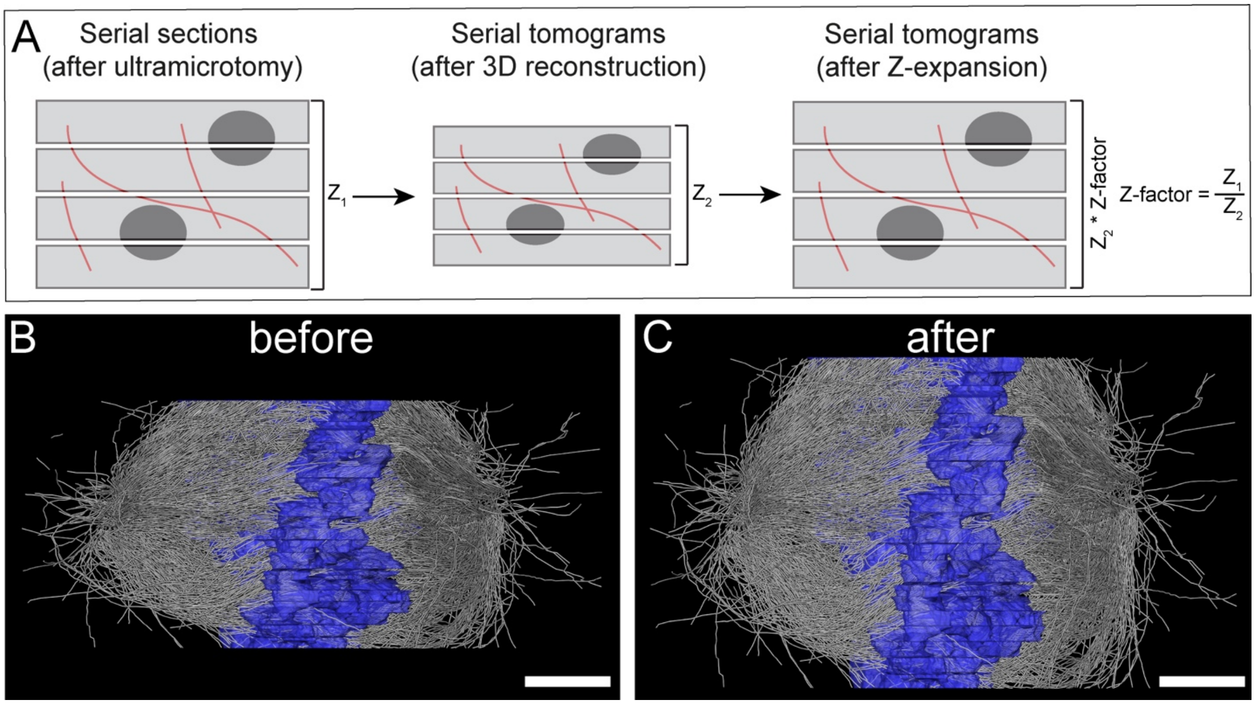

Figure 2-figure supplement 2. Correction of sample collapse caused during data acquisition by electron tomography.

(**A**) Schematic illustration of correction for a sample collapse in Z. Left panel shows a stack of semi-thick sections after ultramicrotomy (total height, Z_1). The mid panel illustrates a sample collapse as obvious after computational stacking of the serial tomograms (total height, Z_2). Right panel, calculation of the Z-factor (Z_1/Z_2) and correction of the collapse by application of the Z-factor (Z_2*Z-factor). (**B**) Side view (Y/Z orientation) of the 3D reconstructed spindle #1 before Z-expansion. (**C**) Side view of the same spindle after Z-expansion. Scale bars, 1 µm.

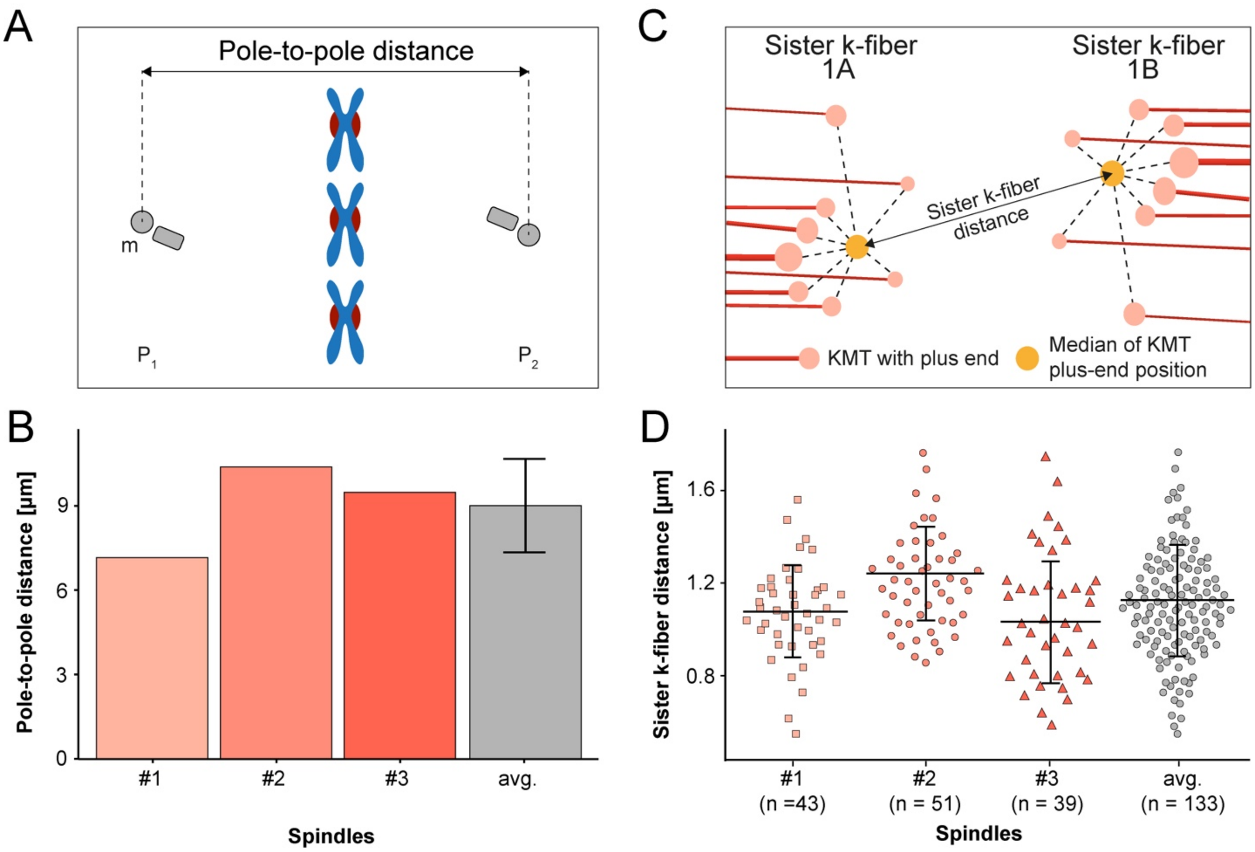

Figure 2-figure supplement 3. Analysis of pole-to-pole and sister k-fiber distances

(**A**) Schematic illustration of the pole-to-pole distance. This distance was calculated as a 3D Euclidean distance between the mother centrioles (m, marked in gray) of the two opposing spindle poles (P_1 and P_2). Chromosomes (blue) and kinetochores (red) are also shown. (**B**) Bar plot showing the pole-to-pole distance for each data and the average of all data sets (mean ± STD indicated by error bar; n = 3). Error bar for an average of all data set was indicated. (**C**) Schematic illustration of the distance between sister k-fiber kinetochore proximal ends (called 1A and 1B) as measured in 3D. The KMTs (red lines) with their plus ends (light red circles) are indicated. The median position (yellow circle) of all KMT plus ends was calculated for each kinetochore pair. (**D**) Graph showing the average sister k-fiber distance for each data set and the average for all data sets (mean ± STD indicated by error bar). The number of measurements per dataset was indicated.

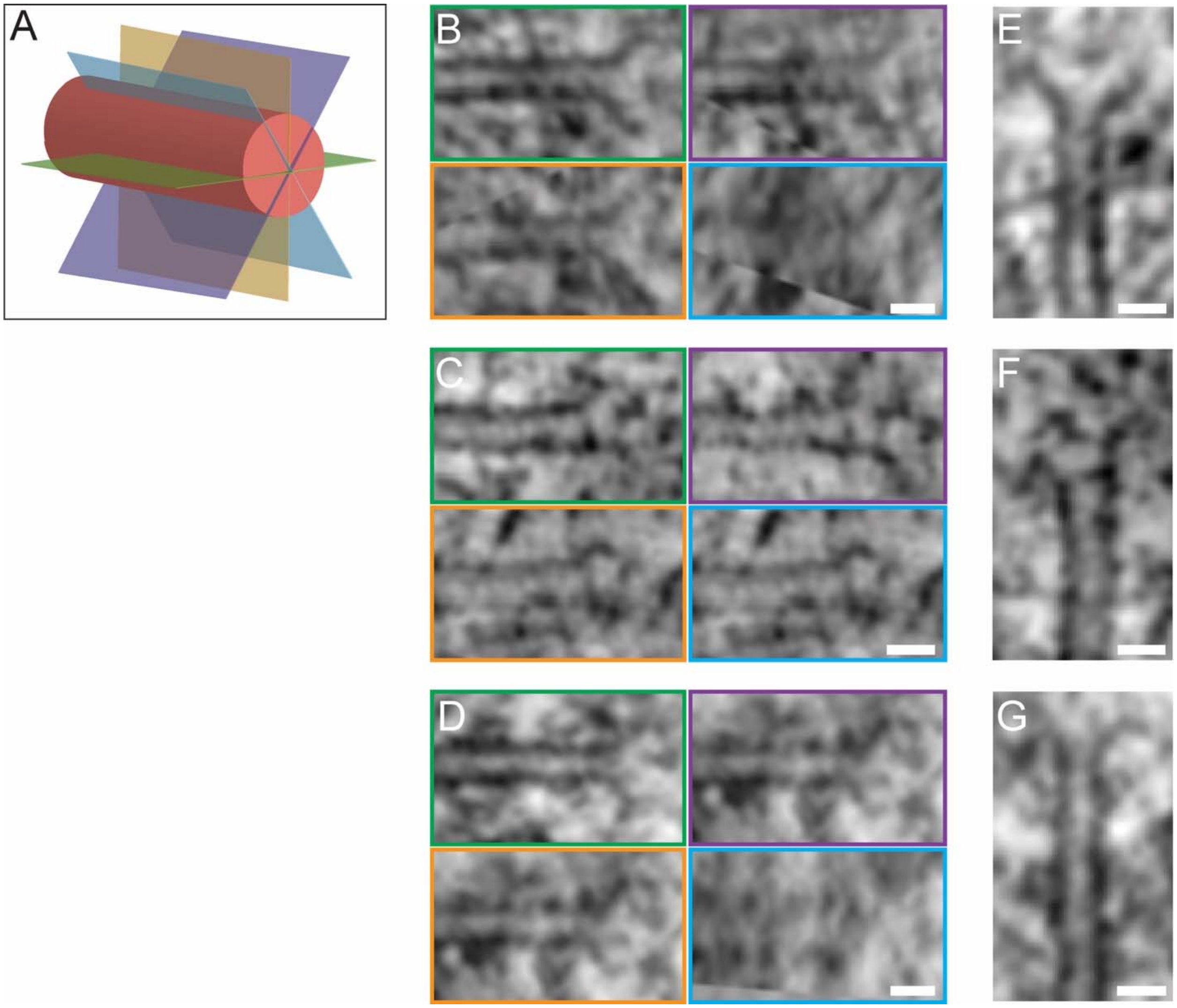

Figure 2-figure supplement 4. Morphology of KMT plus ends

(**A**) Schematic illustration of a KMT (red tube) with different viewing planes (colored in light green, light blue, orange and purple). (**B-D**) Tomographic slices of KMT plus ends are visualized at different viewing planes as shown in A. Scale bars, 25 nm. (**E-G**) Average intensity Z projections of the KMT plus ends as shown in B-D. The KMTs show flared open ends. Scale bars, 25 nm.

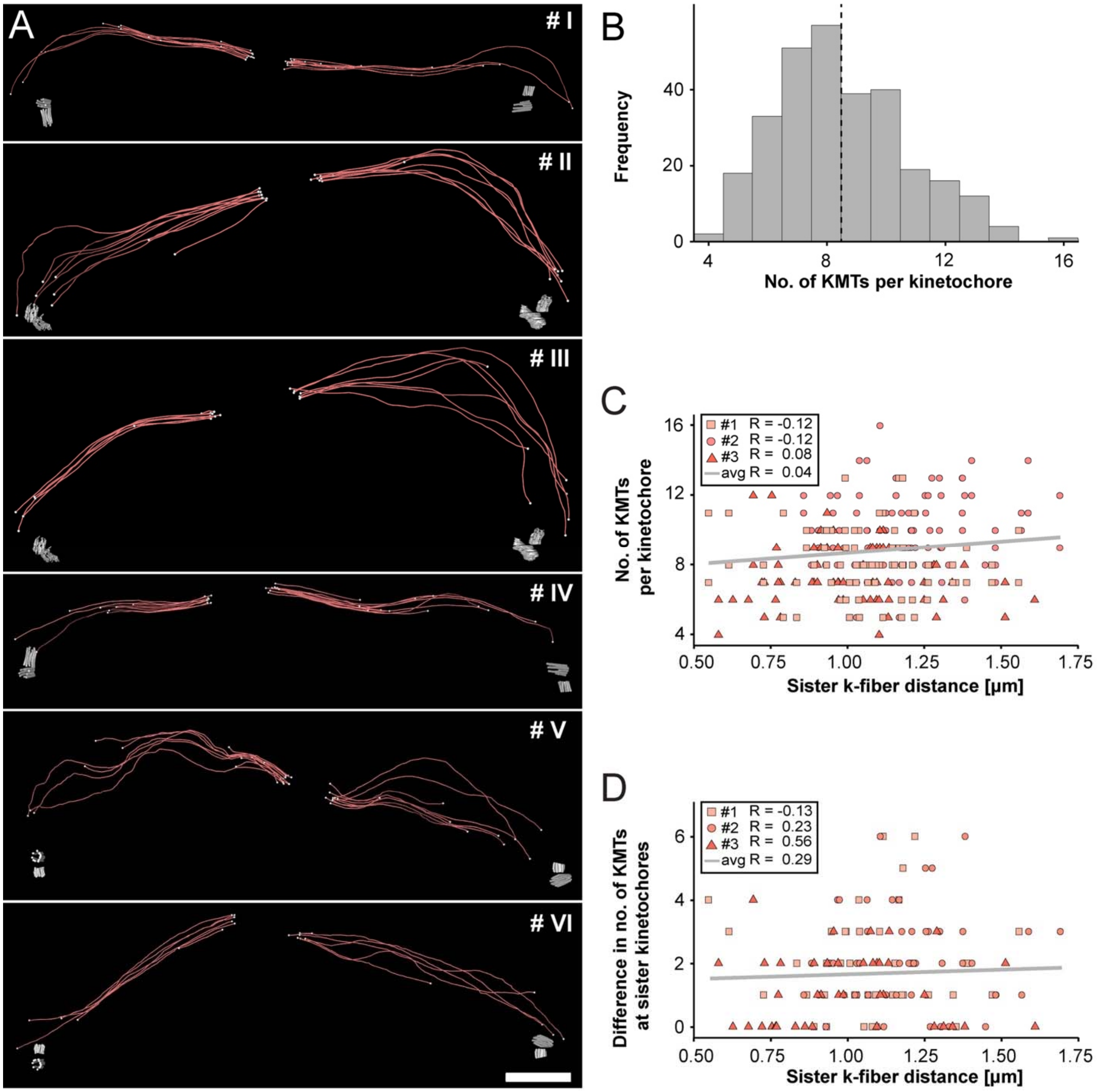

Figure 3. Morphology of k-fibers and number of KMTs attached per kinetochore

(**A**) Examples of individual sister k-fibers extracted from the full 3D reconstructions of metaphase spindles #1. The numbering of these examples (corresponding to the supplementary videos) is given in the upper right corners. KMTs are shown as red lines. The ends of the KMTs are indicated by white spheres, centrioles are shown as cylinders (gray). Scale bar for all examples, 1.5 µm. (**B**) Histogram plot shows the frequency of detected KMTs per kinetochore. This plot includes data from all three spindle reconstructions. The dashed line (black) indicates the average number of KMTs per kinetochore (n = 292). (**C**) Graph showing the number of KMTs associated per kinetochore plotted against the sister k-fiber distance n = 292). The Pearson's correlation coefficient for each data set and the average coefficient for all data sets are given. (**D**) Graph showing the difference (delta) in the number of KMTs associated with the respective sister kinetochores plotted against the distance between the kinetochore-proximal ends of k-fiber pairs (n = 292). The Pearson's correlation coefficient for each data set and the average coefficient for all data sets are given.

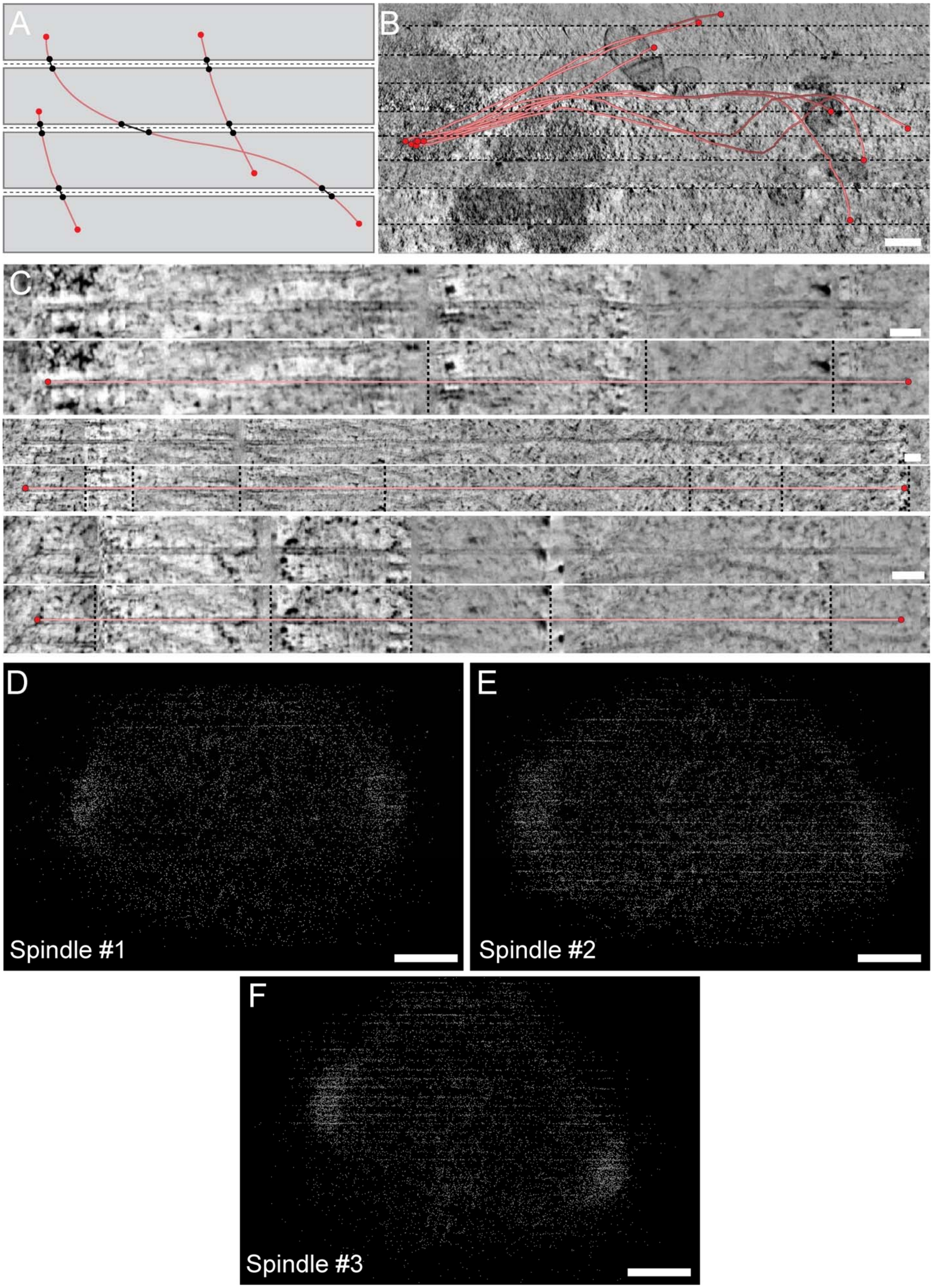
A
B
C
D
Spindle #1
E
Spindle #2
F
Spindle #3

Figure 3-figure supplement 1. MT segmentation and stitching across consecutive serial sections

(**A**) Schematic illustration of MT segmentation across stacked consecutive serial sections. Each section is represented as a gray area. MTs are shown as red lines and their ends as red circles. ‘Artificial ends’ at section borders that need to be stitched are labeled by black dots. The horizontal dashed lines (black) indicate the seams between the sections. (**B**) Stacked serial tomograms show a selected k-fiber that has been followed over several serial sections. The KMTs are indicated as red lines and the ends are marked by red circles. The dashed lines (black) indicate the seam regions. Scale bar, 250 nm. (**C**) Longitudinal views of KMTs of the same k-fiber as shown in B. The top rows of each reconstruction show selected traced KMTs. The bottom rows show the same KMTs with overlays to indicate the length (red line) and the ends (red dots) of each KMT. Scale bars, 50 nm. (**D**) Y/Z view of the 3D model of spindle #1 showing MT tracings at section borders. Scale bar, 500 nm. (**E**) Y/Z view of spindle #2. Scale bar, 600 nm. (**F**) Y/Z view of spindle #3. Scale bar, 500 nm.

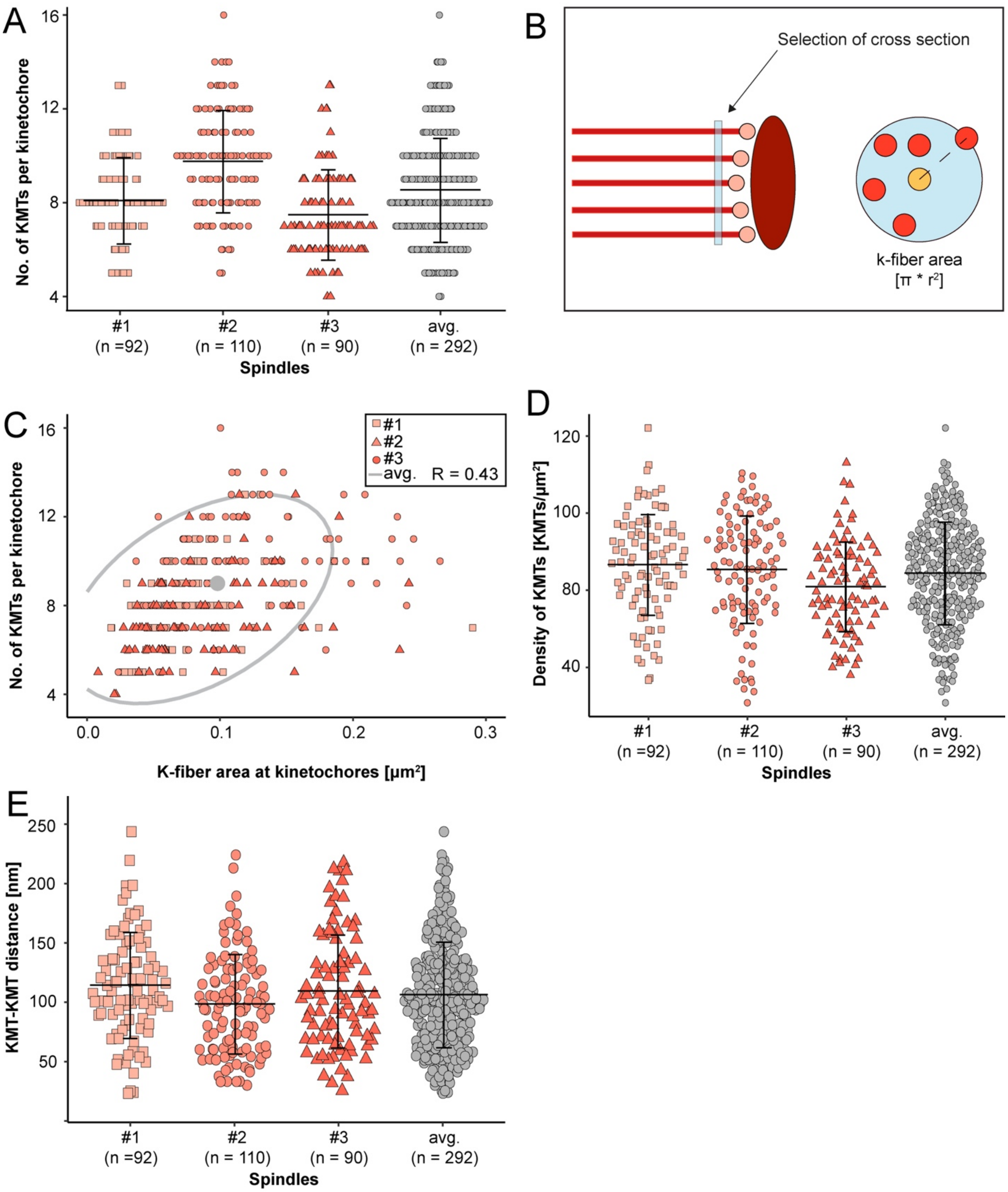

Figure 3-figure supplement 2. Correlation of k-fiber circumference and number of attached KMTs

(**A**) Graph showing the number of KMTs per kinetochore for each data set and the average number for all data sets (mean ± STD indicated by error bars). (**B**) Schematic illustration of the indirect measurement of the k-fiber area. MTs (red lines) with their ends (circles in light red) and the kinetochore (ellipsoid in dark red) are shown (right). The measurement of the cross-section of a k-fiber in the vicinity of the KMT ends is indicated by a blue bar (left). The k-fiber area is given by a circle (blue) enclosing all KMTs (circle reaching to the middle of the peripheral KMTs). (**C**) Graph showing the number of KMTs per kinetochore for all reconstructed spindles plotted against the area of k-fibers at the kinetochore (n = 292). The ellipse (gray) indicates a 95% confidence interval for all data and the central dot (gray) indicates the average kinetochore area. (**D**) Graph showing the density of KMTs at the kinetochore for each 3D reconstruction and for all data sets (mean ± STD indicated by error bars). (**E**) Plot showing the average KMT-to-KMT distance at the kinetochore for all data sets (mean ± STD indicated by error bars). The average for all data sets (mean ± STD) is also given.

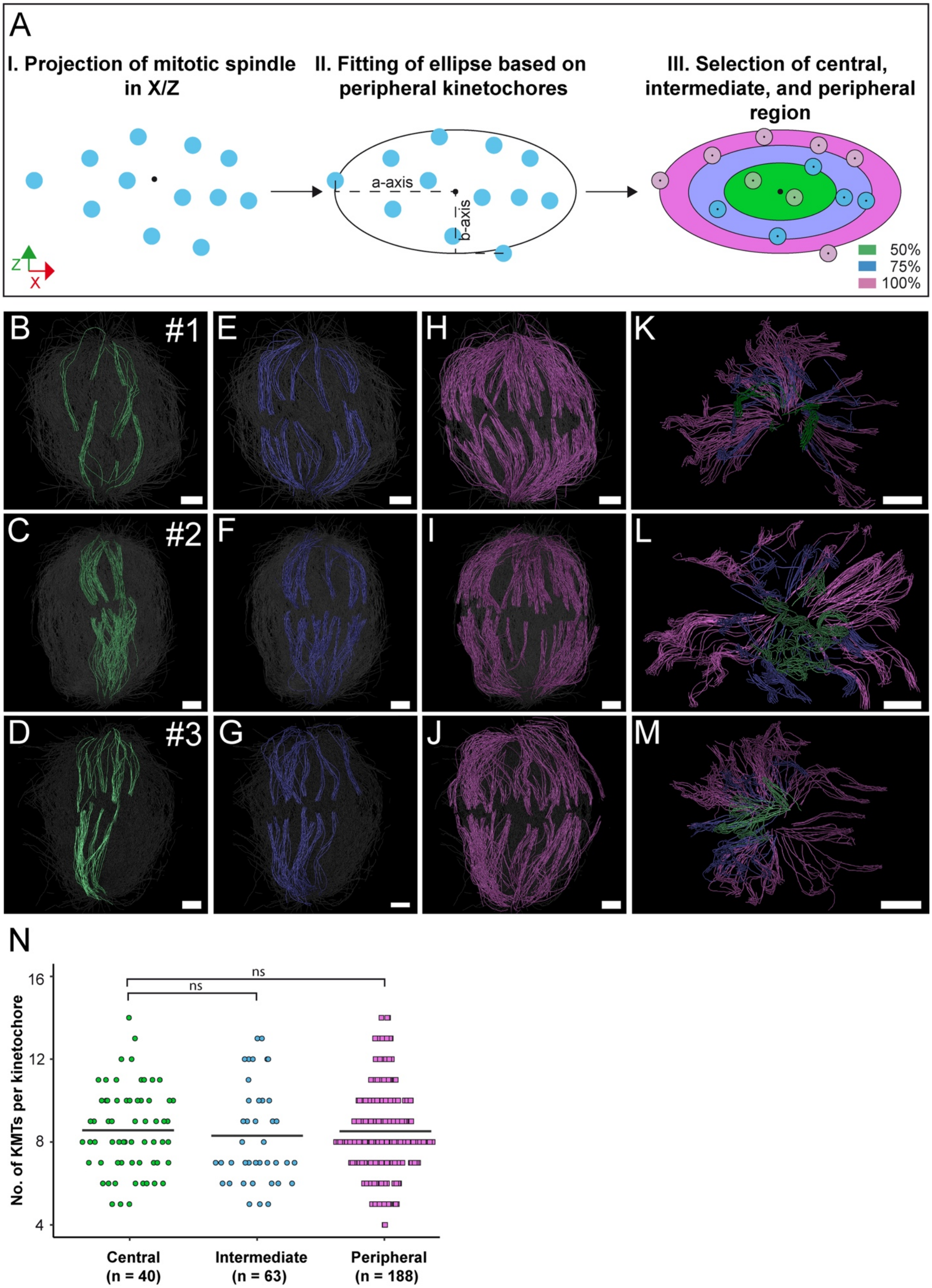
A
I. Projection of mitotic spindle in X/Z
II. Fitting of ellipse based on peripheral kinetochores
III. Selection of central, intermediate, and peripheral region
a-axis
b-axis
Z
X
50%
75%
100%
B
#1
E
H
K
C
#2
F
I
L
D
#3
G
J
M
N
ns
ns
No. of KMTs per kinetochore
16
12
8
4
Central (n = 40)
Intermediate (n = 63)
Peripheral (n = 188)

Figure 3-figure supplement 3. Correlation of KMT number and association with the spindle poles according to the position of the k-fibers in the mitotic spindles

(**A**) Schematic illustration of the k-fiber positions on the X/Z projection of the metaphase plate. Kinetochores are indicated as blue circles. The fitted ellipse (center marked by a black dot) including all kinetochores is characterized by the semi-major (a-) and the semi-minor (b-) axis. The ellipse is divided into three areas representing the percentage of occupancy on the ellipse (0-50%, central kinetochores, green; 50-75%, intermediate kinetochores, blue; and 75-100%, peripheral kinetochores, purple). (**B-D**) Perspective views of the reconstructed spindles with selected central k-fibers (green). The numbers of the spindles are indicated in the upper right corners. (**E-G**) Perspective views with selected intermediate k-fibers (blue). (**H-J**) Perspective views with selected peripheral k-fibers (purple). (**K-M**) Cross-section views of the spindles with all k-fiber classes. (**N**) Plot showing the number of KMTs per kinetochore according to the three positional regions in the mitotic spindle for all data sets. The mean of the KMT number is indicated. A Student's t-test was applied for statistical analysis (mean values indicated by error bars). Scale bars, 1 µm.

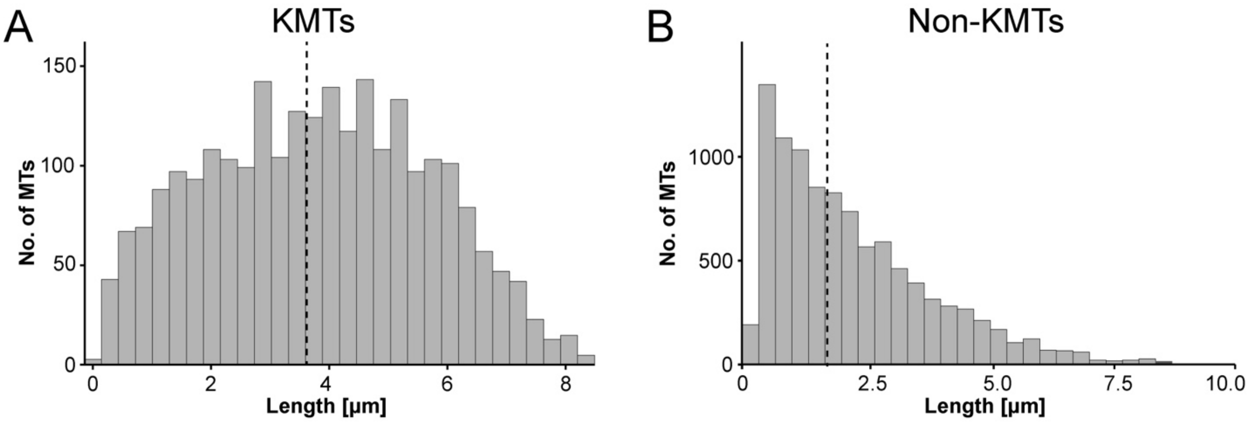

Figure 4. Analysis of MT length distribution

(**A**) Histogram showing the length distribution of KMTs from all data sets (n = 2580). The dashed line indicates the average length of KMTs. (**B**) Histogram showing the length distribution of non-KMTs (n = 9957). The dashed line indicates the average length of non-KMTs.

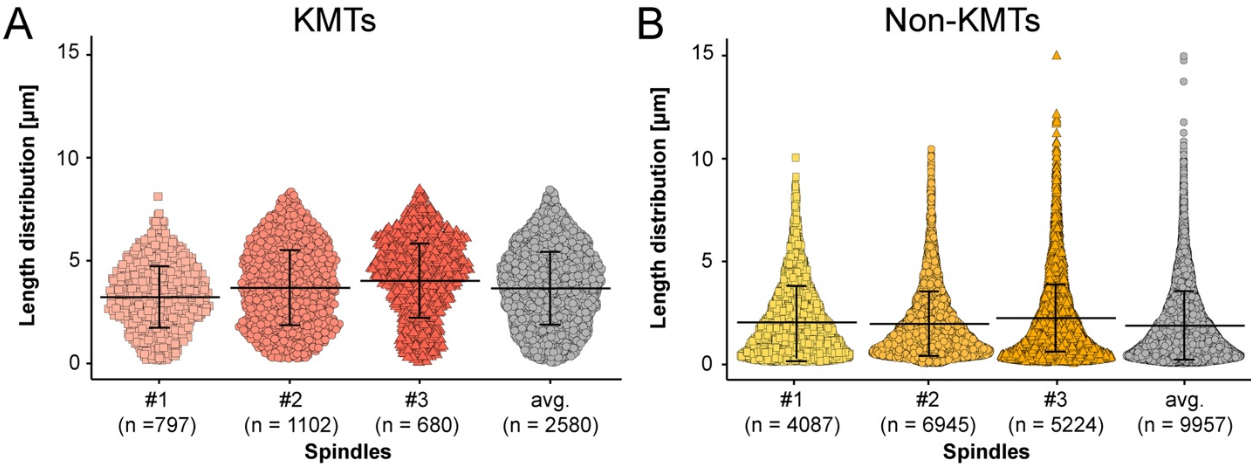

Figure 4-figure supplement 1. Length distribution of KMTs and non-KMTs

(**A**) Beeswarm plot showing the length distribution of KMTs in the individual data sets. The average of all data sets is also given. The plots show the mean ± STD indicated by the error bar. (**B**) Beeswarm plot showing the length distribution of non-KMTs in the individual data sets. The average of all data sets is also given. The plots show the mean ± STD indicated by the error bars.

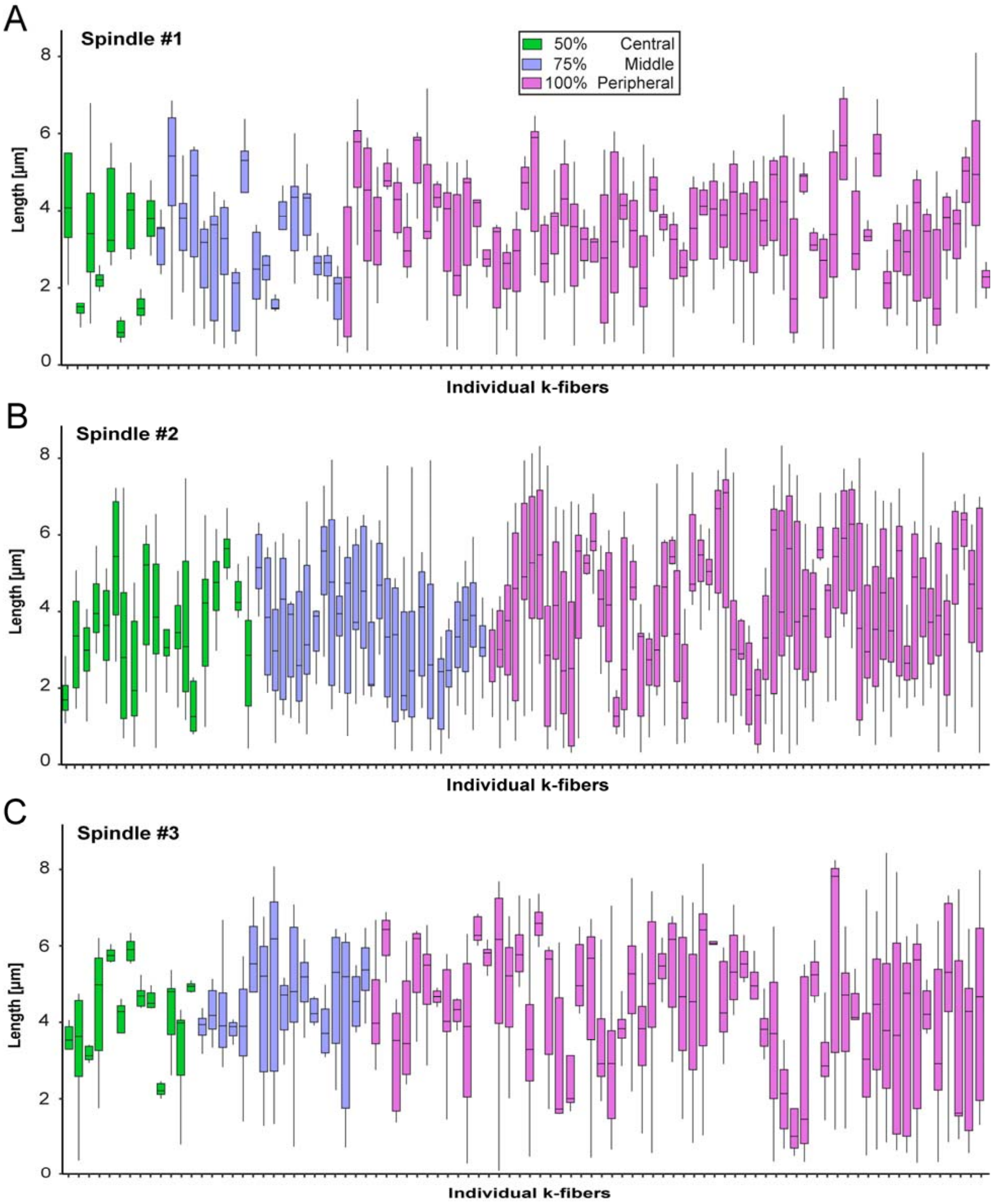

1183

1184 **Figure 4-figure supplement 2. KMT length distribution based on the k-fiber**
1185 **position in the spindle**

(**A**) Box plot showing the length distribution of KMTs in individual k-fibers as observed in spindle #1 (n = 98). The k-fibers are displayed and color-coded according to their position within the spindle. Each bar shows the mean ± STD indicated by error bars. (**B**) KMT length distribution in spindle #2 (n = 110). (**C**) KMT length distribution in spindle #3 (n = 90).

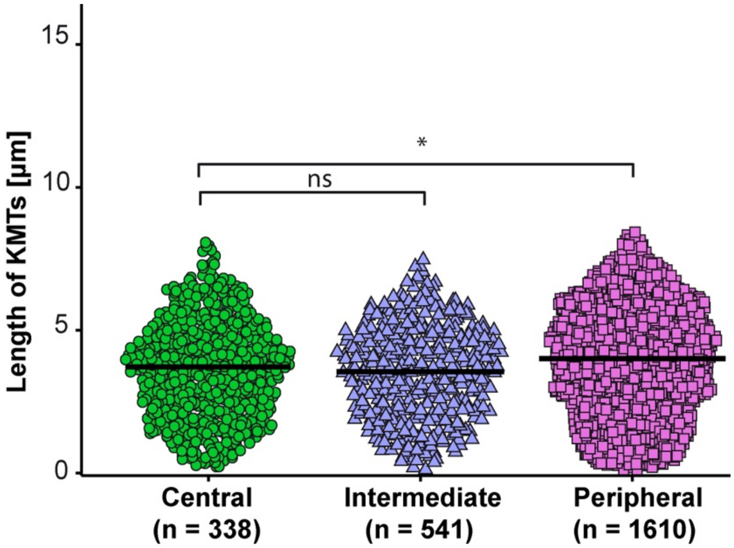

Figure 4-figure supplement 3. KMT length distribution based on position within the spindle for individual k-fiber

Beeswarm plot showing the length distribution of KMTs in the average of all data sets based on the k-fiber position in the spindle. The plots show the mean indicated by black bar. The statistical significance ($p<0.001$) was calculated with a Student's t-test. The mean values are also indicated by error bars.

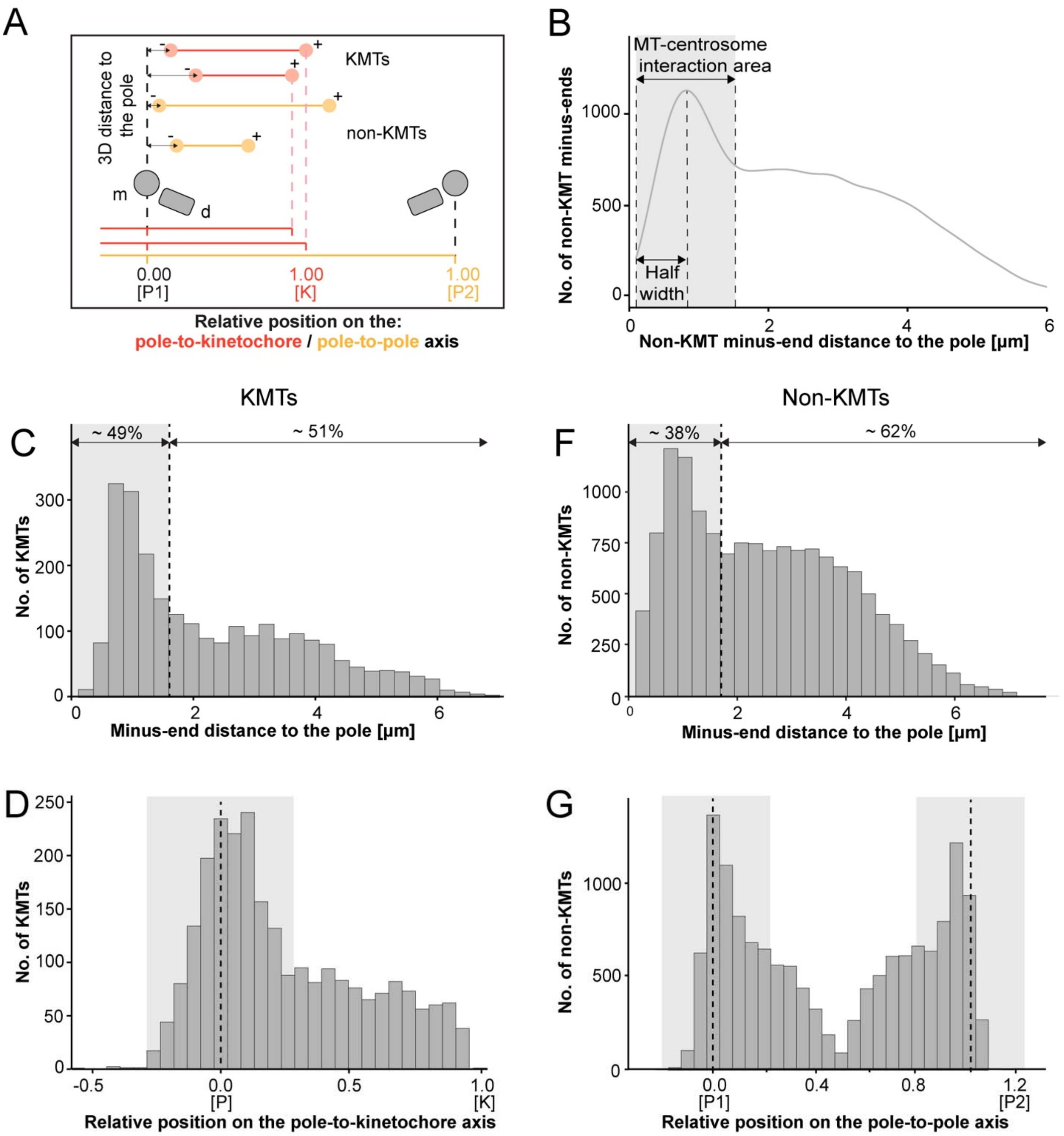

Figure 5. Analysis of MT minus ends

(**A**) Measurement of MT minus-end positioning. A KMT (red line) with its ends (red circles) and a non-KMT (yellow line) with its ends (yellow circles) are shown. The distance of both the KMT and the non-KMT minus ends to the center of the mother centriole was calculated. The relative position of the KMT minus ends along the pole-to-kinetochore axis and the non-KMT minus ends along the pole-to-pole axis was also determined (P1 – pole 1; P2 – pole 2; K – kinetochore). (**B**) Determination of the MT-centrosome interaction area. Graph showing the number of non-KMT minus ends plotted against their distance to the pole (i.e., to the center of the mother centriole). The determined area of the interaction of non-KMTs with the centrosome and the half-width of this area is indicated in gray. The border of the MT-centrosome interaction area (right dashed line) was determined by identifying the half-width of a peak of minus-end distance distribution. (**C**) Histogram showing the distribution of the KMT minus-end distances to the center of the mother centriole (n = 2580). The MT-centrosome interaction area as defined in B is indicated by a gray area (dashed line shows the border of this area). (**D**) Histogram showing the relative position of the KMT minus ends on the pole-to-kinetochore axis (n = 2580). The position of the spindle pole (P=0, dashed line) and the kinetochore (K=1) is indicated. The MT-centrosome interaction area is indicated in gray. (**F**) Histogram showing the distribution of the non-KMT minus-end distances to the center of the mother centriole (n = 9957). (**G**) Plot showing the relative position of the non-KMT minus ends on the pole-to-pole axis. The position of the spindle poles (P1=0, P2=1) is indicated (n = 9957). The MT-centrosome interaction area is indicated in gray.

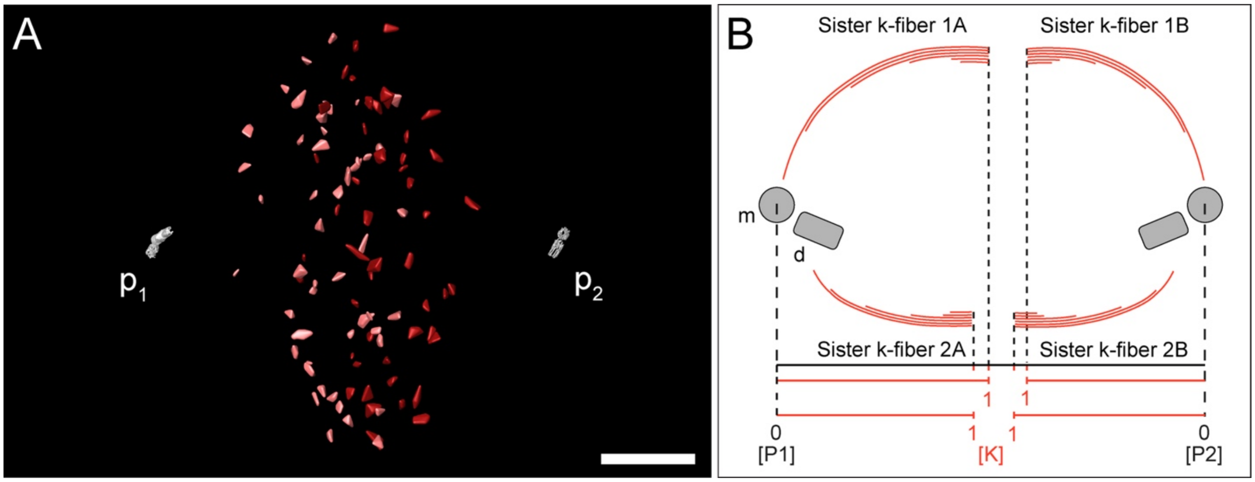

Figure 5-figure supplement 1. Normalization of minus-end positioning on the pole-to-kinetochore axis

(**A**) Three-dimensional model of the kinetochores visualized in spindle #1. For each kinetochore pair, each kinetochore is assigned to the closest spindle pole (p_1, left pole, kinetochores in light red; p_2, right pole, kinetochores in dark red). (**B**) Schematic drawing illustrating the normalization of KMT ends positioning (pole position, P1 and P2 = 0; kinetochore position = 1). End positioning is then determined between positions 0 and 1 for each k-fiber.

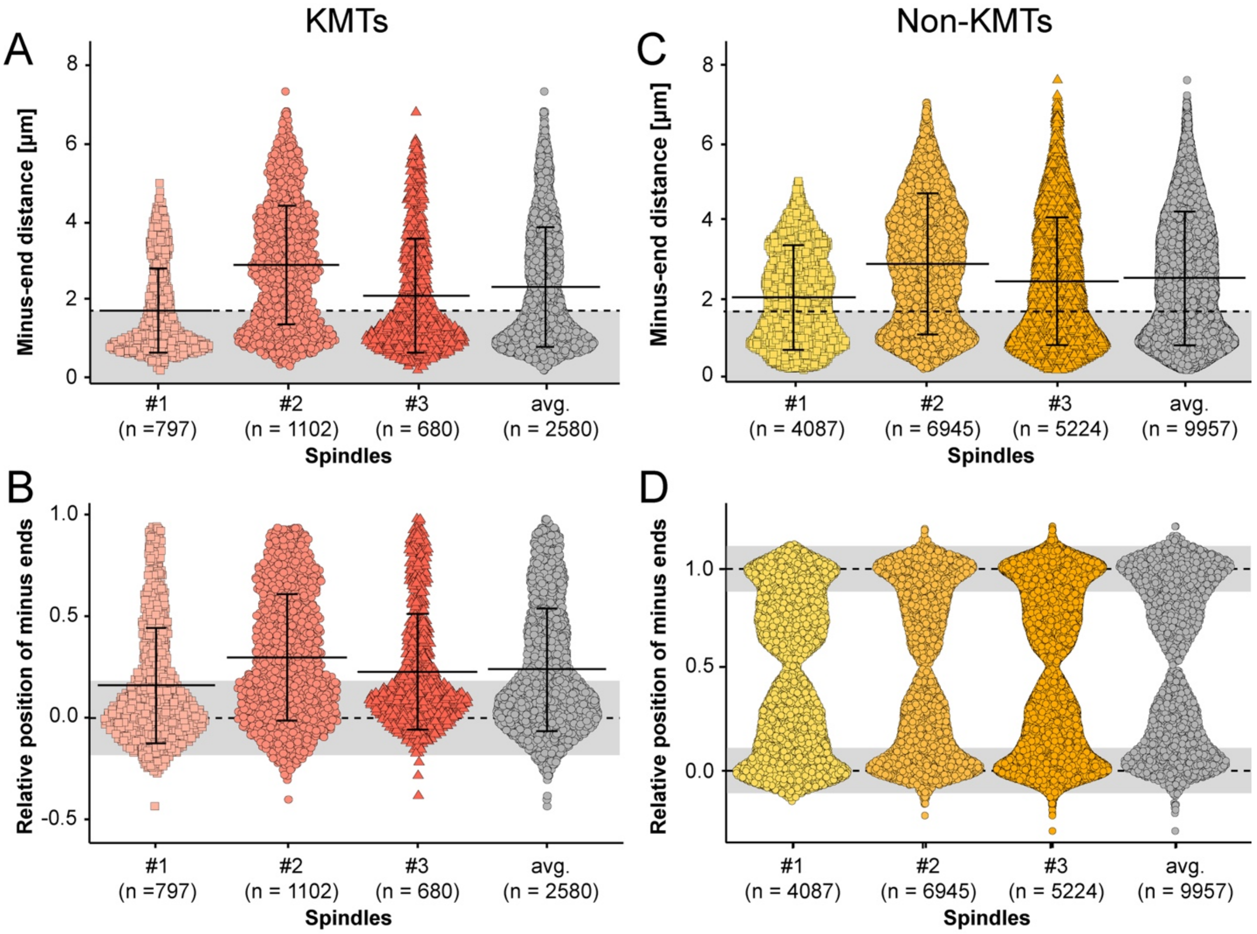

Figure 5-figure supplement 2. Minus-end distribution of KMTs and non-KMTs

(**A**) Beeswarm plot showing the distribution of KMT minus-end distances to the center of the mother centrioles. The MT-centrosome interaction area is indicated in gray (mean ± STD indicated by error bars). (**B**) Plot showing the distribution of relative positioning of the KMT minus ends on the pole-to-kinetochore axis (position of the pole, P=0; the position of the kinetochore = 1; mean ± STD indicated by error bars). (**C**) Distribution of the distances of the non-KMT minus ends to the center of the mother centriole (mean ± STD indicated by error bars). (**D**) Distribution of relative positioning of the non-KMT minus ends on the pole-to-kinetochore axis.

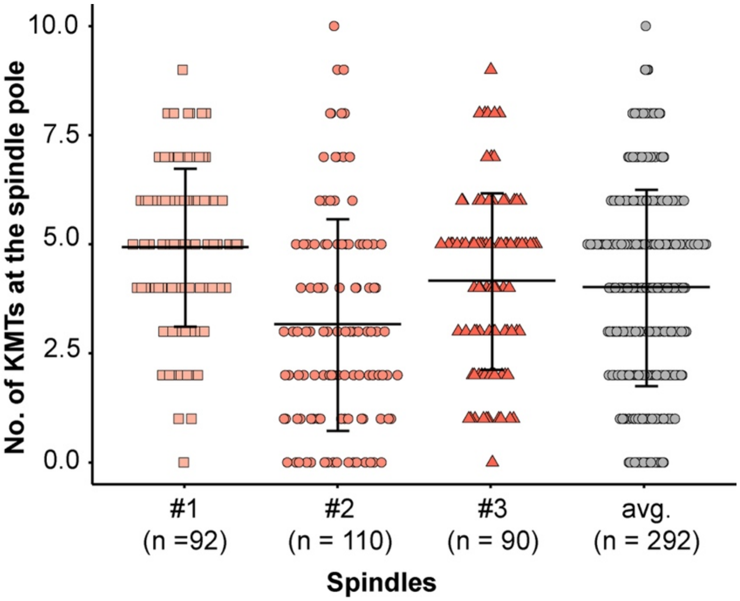

Figure 5-figure supplement 3. K-fiber analysis of KMT minus ends reaching the pole

Plot showing the number of KMT minus ends per k-fiber at the spindle pole for each data set and the average number for all data sets (mean ± STD indicated by error bars).

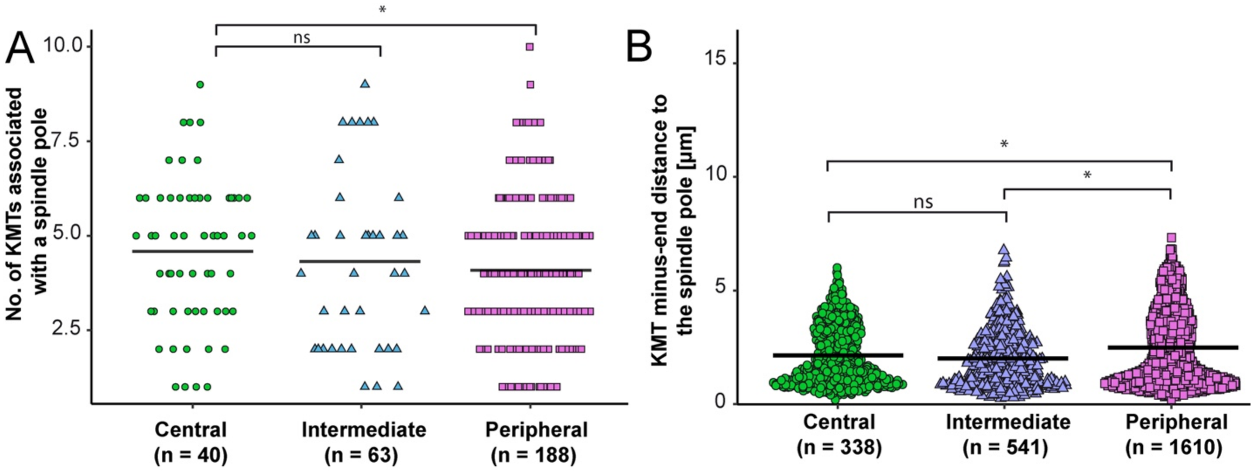

Figure 5-figure supplement 4. KMT minus-end distribution based on the k-fiber position in the spindle

(**A**) Plot showing the number of KMTs in each k-fiber associated with the spindle poles for the three positional regions in the mitotic spindle for all data sets. The mean values are indicated. (**B**) Beeswarm plot showing number of KMT minus-end associated with the center of the mother centrioles for each k-fiber. The mean value was indicated with error bars. The statistical significance (p<0.001) was calculated with a Student's t-test.

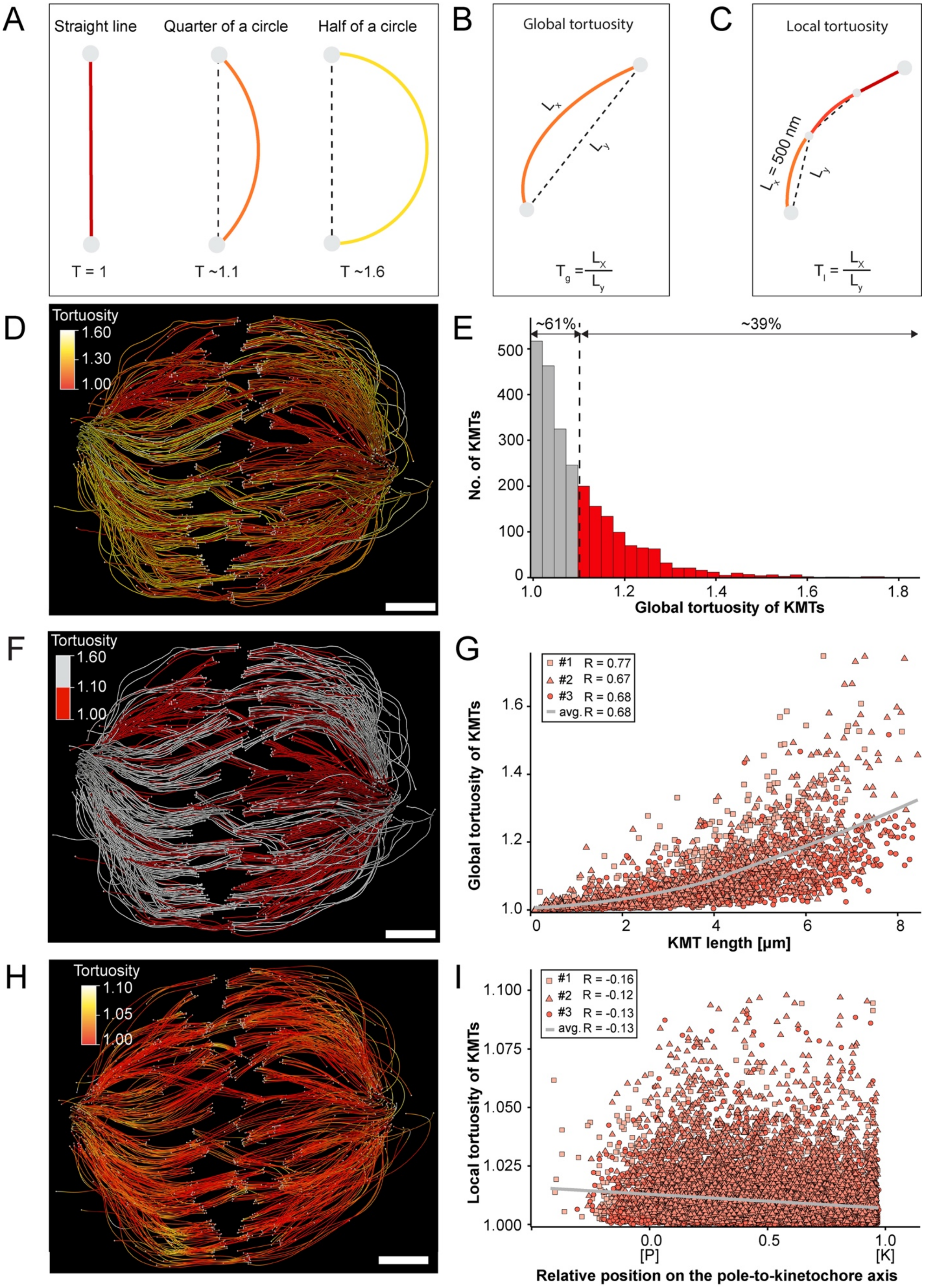
A
Straight line
Quarter of a circle
Half of a circle
T = 1
T ~1.1
T ~1.6
B
Global tortuosity
L_x
L_y
$T_g = \frac{L_x}{L_y}$
C
Local tortuosity
L_x = 500 nm
L_y
$T_l = \frac{L_x}{L_y}$
D
Tortuosity
1.60
1.30
1.00
E
~61%
~39%
No. of KMTs
0
100
200
300
400
500
1.0
1.2
1.4
1.6
1.8
Global tortuosity of KMTs
F
Tortuosity
1.60
1.10
1.00
G
#1 R = 0.77
#2 R = 0.67
#3 R = 0.68
avg. R = 0.68
Global tortuosity of KMTs
1.0
1.2
1.4
1.6
0
2
4
6
8
KMT length [µm]
H
Tortuosity
1.10
1.05
1.00
I
#1 R = -0.16
#2 R = -0.12
#3 R = -0.13
avg. R = -0.13
Local tortuosity of KMTs
1.000
1.025
1.050
1.075
1.100
0.0
[P]
0.5
1.0
[K]
Relative position on the pole-to-kinetochore axis

Figure 6. Global and local tortuosity of KMTs

(**A**) Schematic illustration of tortuosity (T) as given for a straight line, a quarter of a circle, and a half of a circle. (**B**) Schematic illustration of global tortuosity (T_g) of KMTs given by the ratio of the spline length (L_x) to the 3D Euclidean distance between the KMT ends illustrated by gray dots (L_y). (**C**) Schematic illustration of KMT local tortuosity (T_l) as given by division segments with a length of 500 nm. (**D**) Three-dimensional model of k-fibers (spindle #1) showing the global tortuosity of KMTs as indicated by color coding (top left corner). (**E**) Histogram showing the frequency of different degrees of KMT tortuosity (n = 2580). A tortuosity of 1.1 is length. The Pearson's correlation coefficient is given for each reconstructed spindle. The gray line indicates indicated by a dashed line. (**F**) Perspective view as shown in D. Straight KMTs (tortuosity of 1.0 - 1.1, red) and curved KMTs (tortuosity ≥ 1.1, white) are highlighted. (**G**) Correlation of global tortuosity and KMT length (n = 2580). The Pearson's correlation coefficient is given for each reconstructed spindle. The gray line indicates the local regression calculated by the loess method. (**H**) Three-dimensional model of k-fibers (from spindle #1) showing the local tortuosity of KMTs as indicated by color-coding. (**I**) Correlation of the local tortuosity of KMTs with the relative position along the pole (P)-to-kinetochore (K) axis (n = 2580). Scale bars, 1 µm.

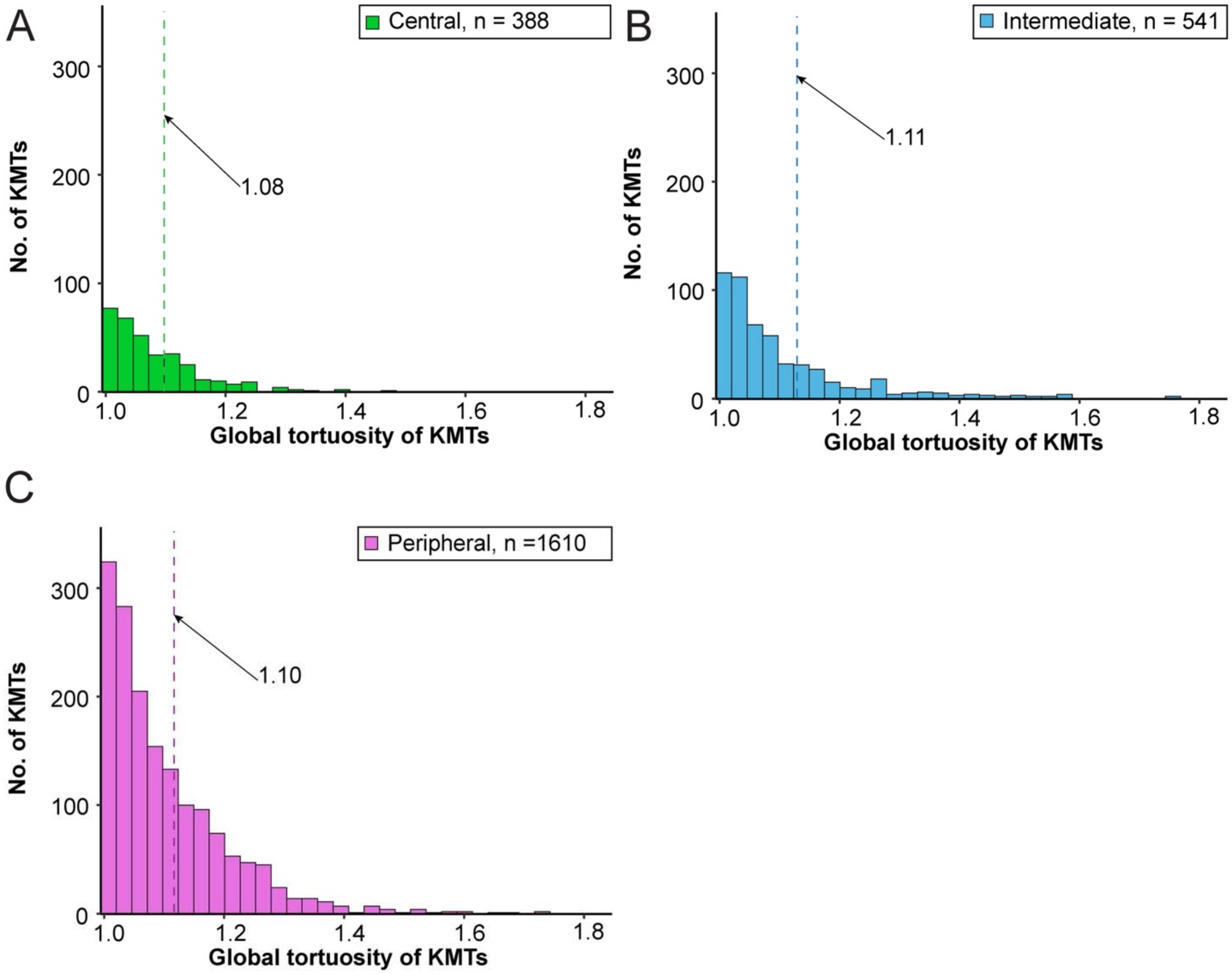

Figure 6-figure supplement 1. Global tortuosity of KMTs according to k-fiber positioning in the spindle

(**A**) Histogram showing the number of central KMTs plotted against the global tortuosity (n = 338). (**B**) Histogram showing intermediate KMTs (n = 541). (**C**) Histogram showing peripheral KMTs. The mean global tortuosity of each k-fiber position is indicated by a dashed line (n = 1610).

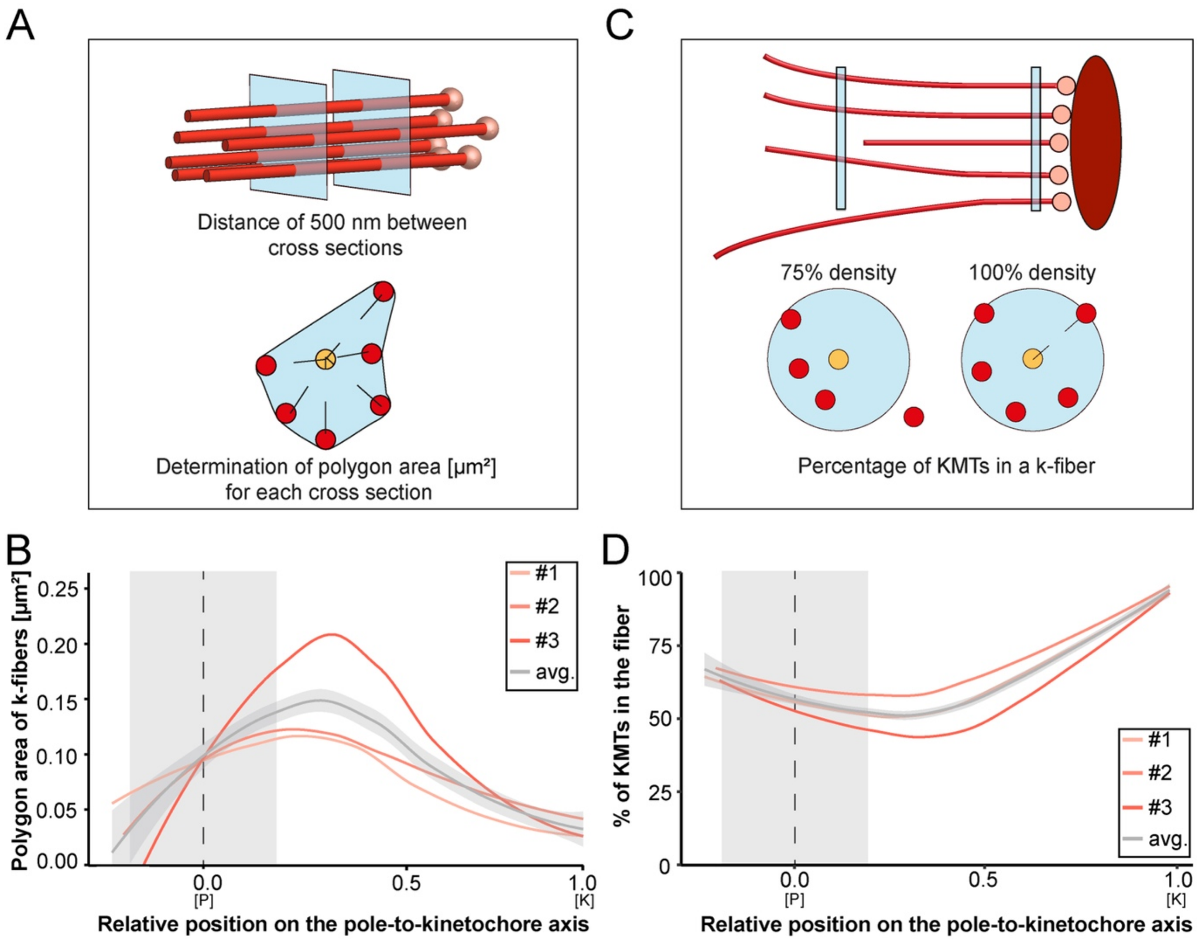

Figure 7. Shape of k-fibers

(**A**) Schematic illustration of the analysis of polygonal areas as obtained from k-fiber cross-sections. KMTs are shown in red, KMT ends as red spheres. The cross-section of the given k-fiber is shown as a blue square and the median position of all KMTs in the cross-section as a yellow circle. (**B**) Distribution of the k-fiber polygonal area along with the relative position on the pole [P]-to-kinetochore [K] axis (n = 292). (**C**) Schematic illustration of the k-fiber density analysis. For each k-fiber, a radius at the kinetochore was estimated by calculating a minimum circle enclosing all KMTs. The determined radius was then enlarged by factor 2 to account for k-fiber flexibility. Along with the k-fiber, the number of KMTs enclosed in the selected radius was then measured. (**D**) Distribution of the KMT enclosed in the k-fiber along with the relative position along the pole [P]-to-kinetochore [K] axis (n = 292). For each reconstructed spindle, data sets are presented as polynomial lines showing local regression calculated with the loess method. Average values with standard deviations are shown in gray.

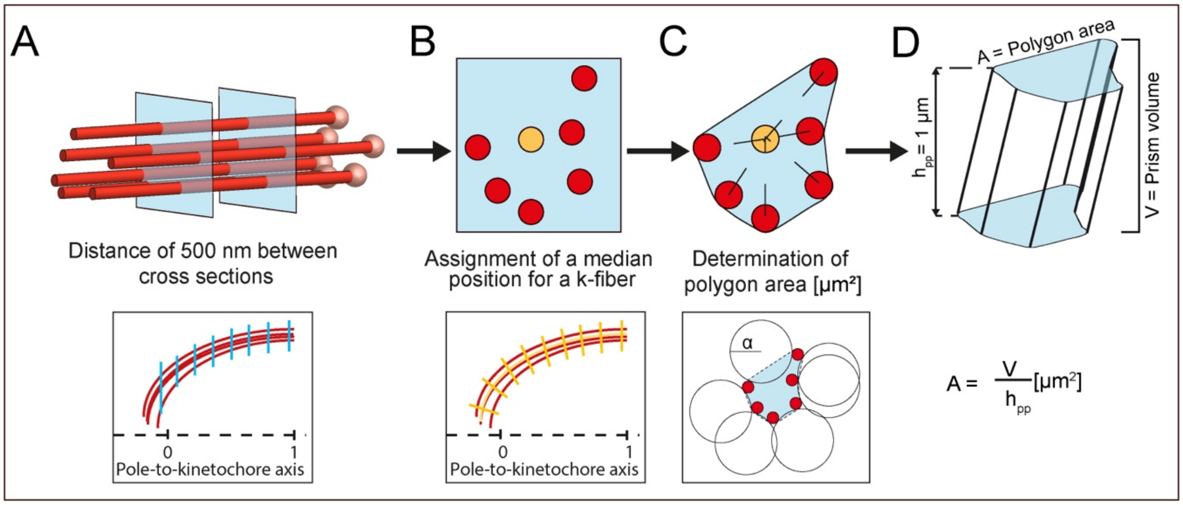

Figure 7-figure supplement 1. Schematic illustration of the analysis of k-fiber area and density

(**A**) Selection of cross-sections on a k-fiber (KMTs in red, KMT ends, red spheres) every 500 nm (upper row - blue squares; lower row - blue lines). (**B**) Assignment of a median position (upper row - yellow circle; lower row, yellow line) for each cross-section and geometric correction of each cross-section based on the k-fiber's curvature (lower row - yellow short lines). (**C**) Calculation of the polygonal area (upper row). The polygonal area was calculated using the alpha shape algorithm. For each cross-section, circles with a diameter defined by α (lower row - black lines) were fitted around the 2D projection of KMTs. The polygonal α-shape was created by drawing lines around KMTs that were at the junction of fitted circles (lower row - black dashed lines). (**D**) Calculation of the polygonal area from the created prism shape. For this, a polygonal area was duplicated and moved in Euclidean space by 1 µm in each dimension to create a prism shape. The polygonal area (A) is given by dividing a prism volume [μm^3] by a prism height (h_{pp} = 1 µm).

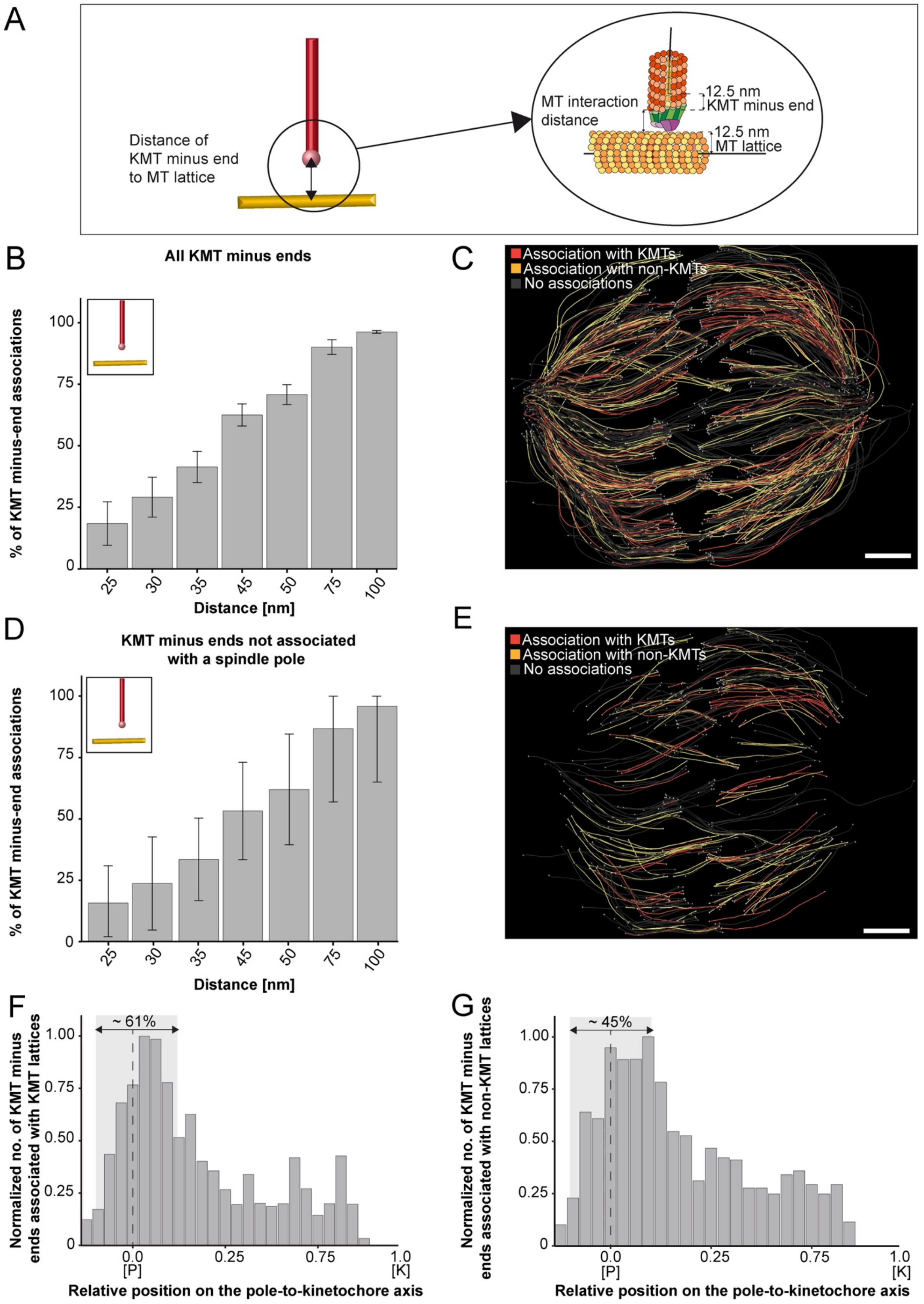
A
Distance of
KMT minus end
to MT lattice
MT interaction
distance
12.5 nm
KMT minus end
12.5 nm
MT lattice
B
All KMT minus ends
% of KMT minus-end associations
0
25
50
75
100
25
30
35
45
50
75
100
Distance [nm]
C
🟥 Association with KMTs
🟨 Association with non-KMTs
⬛ No associations
D
KMT minus ends not associated
with a spindle pole
% of KMT minus-end associations
0
25
50
75
100
25
30
35
45
50
75
100
Distance [nm]
E
🟥 Association with KMTs
🟨 Association with non-KMTs
⬛ No associations
F
Normalized no. of KMT minus
ends associated with KMT lattices
~ 61%
0
0.25
0.50
0.75
1.00
0.0
[P]
0.25
0.75
1.0
[K]
Relative position on the pole-to-kinetochore axis
G
Normalized no. of KMT minus
ends associated with non-KMT lattices
~ 45%
0
0.25
0.50
0.75
1.00
0.0
[P]
0.25
0.75
1.0
[K]
Relative position on the pole-to-kinetochore axis

Figure 8. Association of KMT minus ends with the MT network

(**A**) Schematic illustration of the association of KMT minus ends with MT lattices showing a KMT (red line) with its minus end (red sphere) located close to the lattice of a non-KMT (yellow line). The distance from a KMT minus-end to the center of a non-KMT lattice is estimated. (**B**) Bar plot showing the percentage of all KMT minus ends associated with an MT lattice depending on defined distances of association (25 - 100 nm; mean ± STD indicated by error bars; n = 2580). The standard deviations are given. (**C**) A 3D model showing the interaction pattern of all KMT minus ends associated with MTs based on an interaction distance of 35 nm (data obtained from spindle #1). KMTs with their minus ends associated with other KMTs are labeled in red, and KMTs with an association with non-KMTs are marked in yellow. KMTs without any association with other MTs are shown in gray. (**D**) Bar plot showing the percentage of KMT minus ends not associated with the centrosome interaction area (mean ± STD indicated by error bars; n = 1558). The association with MT lattices is shown in relation to the chosen distance of association. (**E**) Three-dimensional model of KMTs with their minus ends not attached to the centrosome and associated with MT lattices. Colors are shown as displayed in the C. (**F**) Graph showing the number of KMT minus ends interacting with KMT lattices within a distance of 35 nm (n = 2580). Numbers of KMT minus ends are normalized by the density of surrounding MTs and plotted against the relative position on the pole-to-kinetochore axis (P, pole; K, kinetochore). (**G**) Bar plot showing the normalized number of KMT minus ends interacting with non-KMT lattices within 35 nm distance (n = 2580). Scale bars, 1 µm.

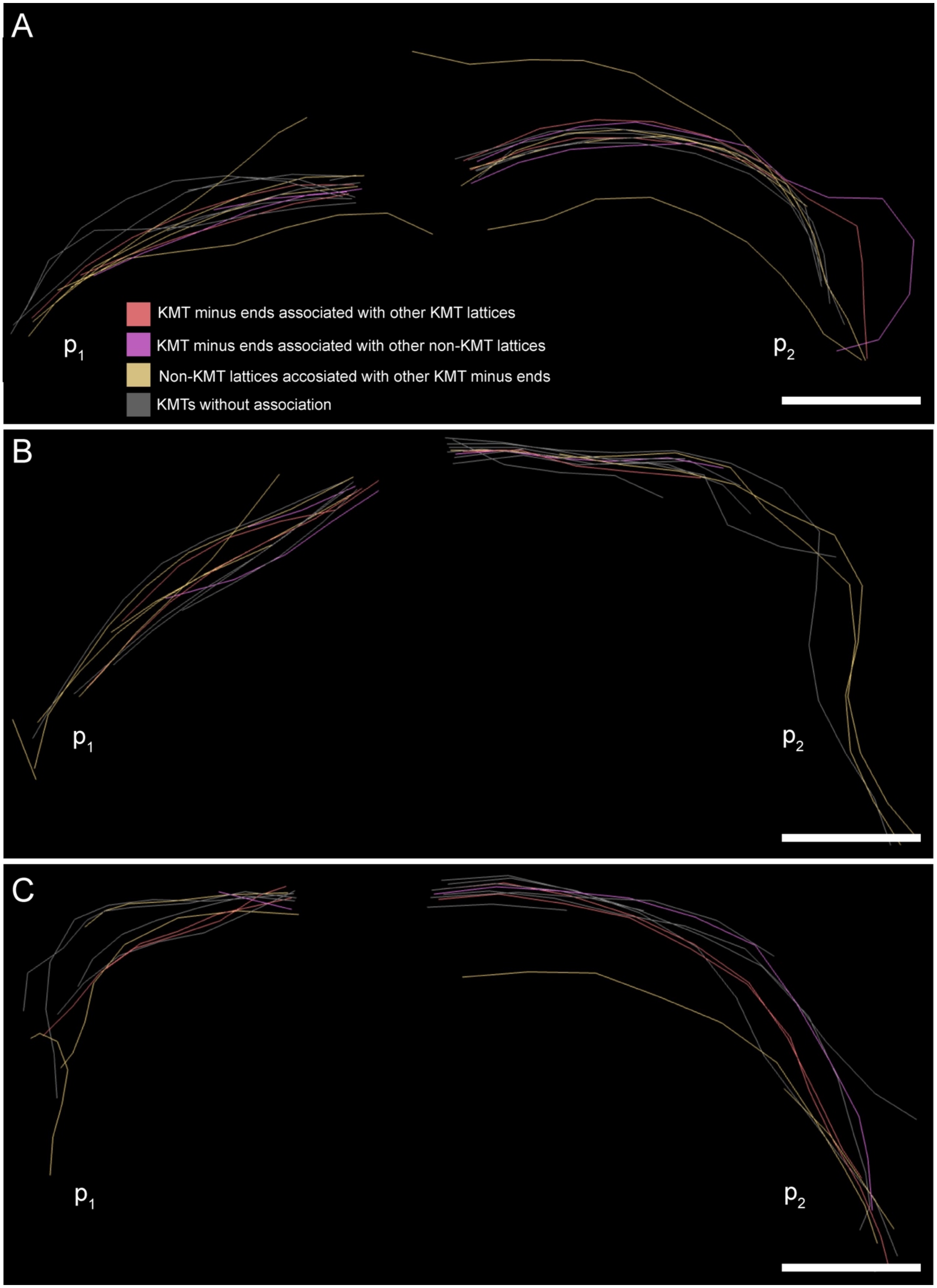
A
🟥 KMT minus ends associated with other KMT lattices
🟪 KMT minus ends associated with other non-KMT lattices
🟨 Non-KMT lattices accosiated with other KMT minus ends
⬛ KMTs without association
p_1
p_2
B
p_1
p_2
C
p_1
p_2

Figure 8-figure supplement 1. Association of KMT minus ends with KMT and non-KMT lattices at 35 nm interaction distance

(**A**) Visualization of KMTs and non-KMTs obtained from the ASGA 3D-Viewer (https://cfci.shinyapps.io/ASGA_3DViewer/) showing a k-fiber pair from spindle #1 (ASGA k-fiber ID: pole1_08). This 3D model illustrates the association of KMT minus ends with MT lattices. The types of interaction are shown by color-coding. The association distance is 35 nm. The approximate position of the spindle poles (p_1, p_2) is indicated. (**B**) Model of k-fiber pair with ID: pole1_20. (**C**) Model of k-fiber pair with ID: pole1_23. Scale bars, 1 µm.

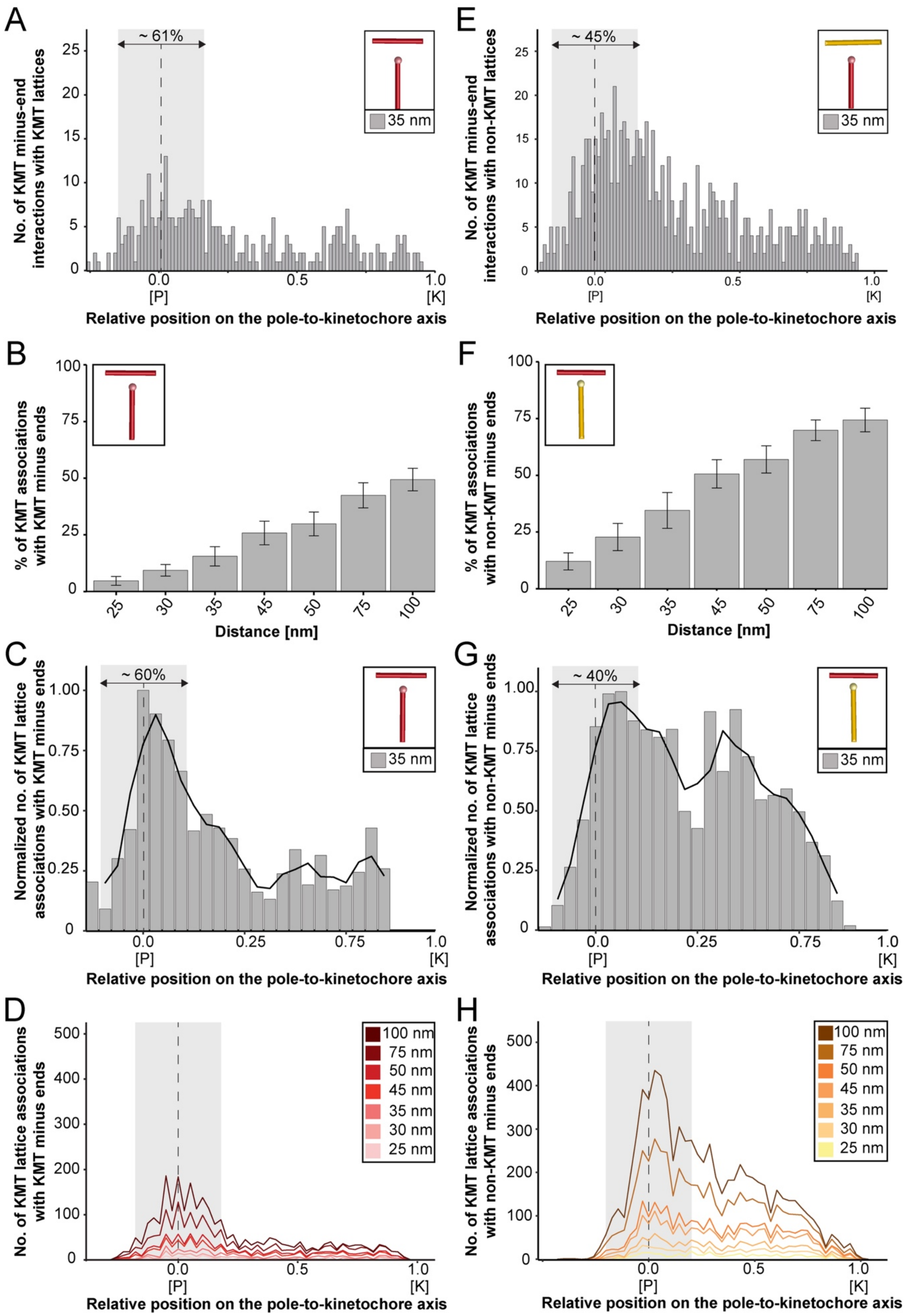
A
~ 61%
No. of KMT minus-end interactions with KMT lattices
0
5
10
15
20
25
0.0
[P]
0.5
1.0
[K]
Relative position on the pole-to-kinetochore axis
35 nm
E
~ 45%
No. of KMT minus-end interactions with non-KMT lattices
0
5
10
15
20
25
0.0
[P]
0.5
1.0
[K]
Relative position on the pole-to-kinetochore axis
35 nm
B
% of KMT associations with KMT minus ends
0
25
50
75
100
25
30
35
45
50
75
100
Distance [nm]
F
% of KMT associations with non-KMT minus ends
0
25
50
75
100
25
30
35
45
50
75
100
Distance [nm]
C
~ 60%
Normalized no. of KMT lattice associations with KMT minus ends
0
0.25
0.50
0.75
1.00
0.0
[P]
0.25
0.5
0.75
1.0
[K]
Relative position on the pole-to-kinetochore axis
35 nm
G
~ 40%
Normalized no. of KMT lattice associations with non-KMT minus ends
0
0.25
0.50
0.75
1.00
0.0
[P]
0.25
0.5
0.75
1.0
[K]
Relative position on the pole-to-kinetochore axis
35 nm
D
No. of KMT lattice associations with KMT minus ends
0
100
200
300
400
500
0.0
[P]
0.5
1.0
[K]
Relative position on the pole-to-kinetochore axis
100 nm
75 nm
50 nm
45 nm
35 nm
30 nm
25 nm
H
No. of KMT lattice associations with non-KMT minus ends
0
100
200
300
400
500
0.0
[P]
0.5
1.0
[K]
Relative position on the pole-to-kinetochore axis
100 nm
75 nm
50 nm
45 nm
35 nm
30 nm
25 nm

Figure 8-figure supplement 2. Association of KMT lattices with MT minus ends

(**A**) Graph showing the number of KMT minus ends interacting with KMT lattices within 35 nm distance (n = 2580). The normalized number of KMT minus ends is plotted against the relative position on the pole-to-kinetochore axis (P, pole; K, kinetochore). The percentage of associations at the MT-centrosome interaction area is indicated. (**B**) Bar plot showing the percentage of KMT lattices associated with other KMT minus ends depending on defined interaction distances (mean ± STD indicated by error bars; n = 2580). The standard deviations are indicated. (**C**) Graph showing the number of KMT lattices associated with other KMT minus ends plotted along with the relative position on the pole-to-kinetochore axis (P, pole; K, kinetochore) and normalized by the spindle density (n = 2580). The distance of MT interaction is 35 nm. The percentage of KMT associations at the MT-centrosome interaction area is indicated. A moving average with a period of 0.05 along the pole-to-kinetochore axis is shown as a black line. (**D**) Plot showing the number of KMT lattices associated with KMT minus ends as shown in C (n = 2580). The plot shows the number of associations for distances of 25, 30, 35, 45, 50, 75 and 100 nm. (**E**) Graph showing the number of KMT minus ends interacting with non-KMT lattices within 35 nm distance (n = 2580). The normalized number of KMT minus ends is plotted against the relative position on the spindle axis (P, pole; K, kinetochore). (**F**) Bar plot showing the percentage of KMT lattices associated with other non-KMT minus ends depending on defined interaction distances (mean ± STD indicated by error bars; n = 2580). The standard deviations are indicated. (**G**) Graph showing the number of KMT lattices associated with non-KMT minus ends normalized by spindle density and plotted along with the relative position on the spindle axis (P, pole; K, kinetochore) (n = 2580). The distance of MT interaction is 35 nm. The percentage of KMT association at the MT-centrosome interaction area is indicated. A moving average with a period of 0.05 along the pole-to-kinetochore axis is shown as a black line. (**H**) Plot showing the number of KMT lattices associated with non-KMT minus ends as shown in G (n = 2580). The plot shows the number of associations for distances of 25, 30, 35, 45, 50, 75 and 100 nm.

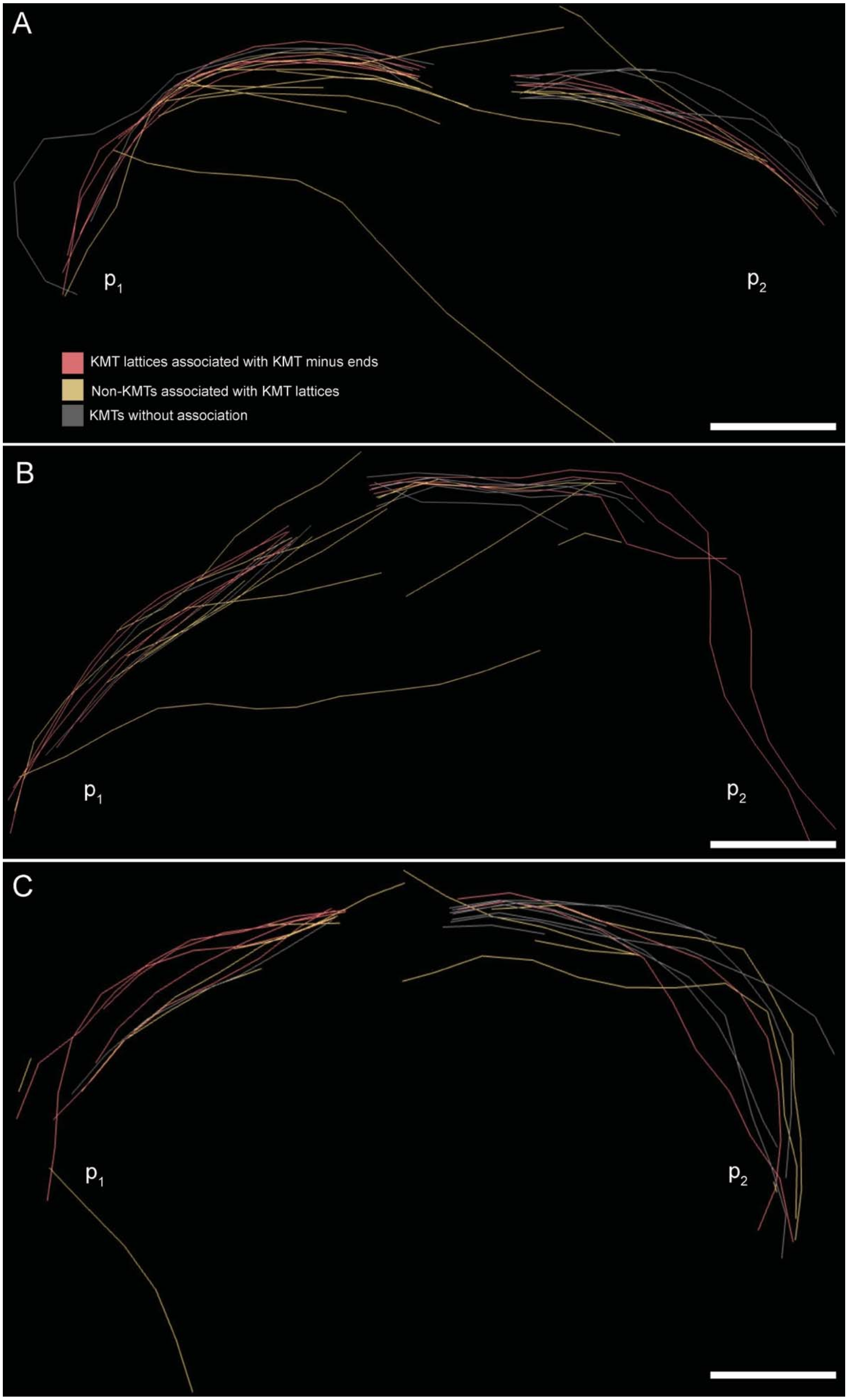
A
p1
p2
🟥 KMT lattices associated with KMT minus ends
🟨 Non-KMTs associated with KMT lattices
⬛ KMTs without association
B
p1
p2
C
p1
p2

Figure 8-figure supplement 3. Association of KMT lattices with other MT minus ends at 35 nm interaction distance

(**A**) Visualization of KMTs and non-KMTs obtained from the ASGA 3D-Viewer (https://cfci.shinyapps.io/ASGA_3DViewer) showing a k-fiber pair from spindle #1 (ASGA k-fiber ID: pole1_08 / pole2_08). This 3D model illustrates the association of KMT lattices with MT minus ends at an association distance of 35 nm. The types of interaction are shown by color-coding. The approximate position of the spindle poles (p_1, p_2) is indicated. (**B**) Model of k-fiber pair with ID: pole1_20 / pole2_20. (**C**) Model of k-fiber pair with ID: pole1_23 / pole2_23. Scale bars, 1 µm.

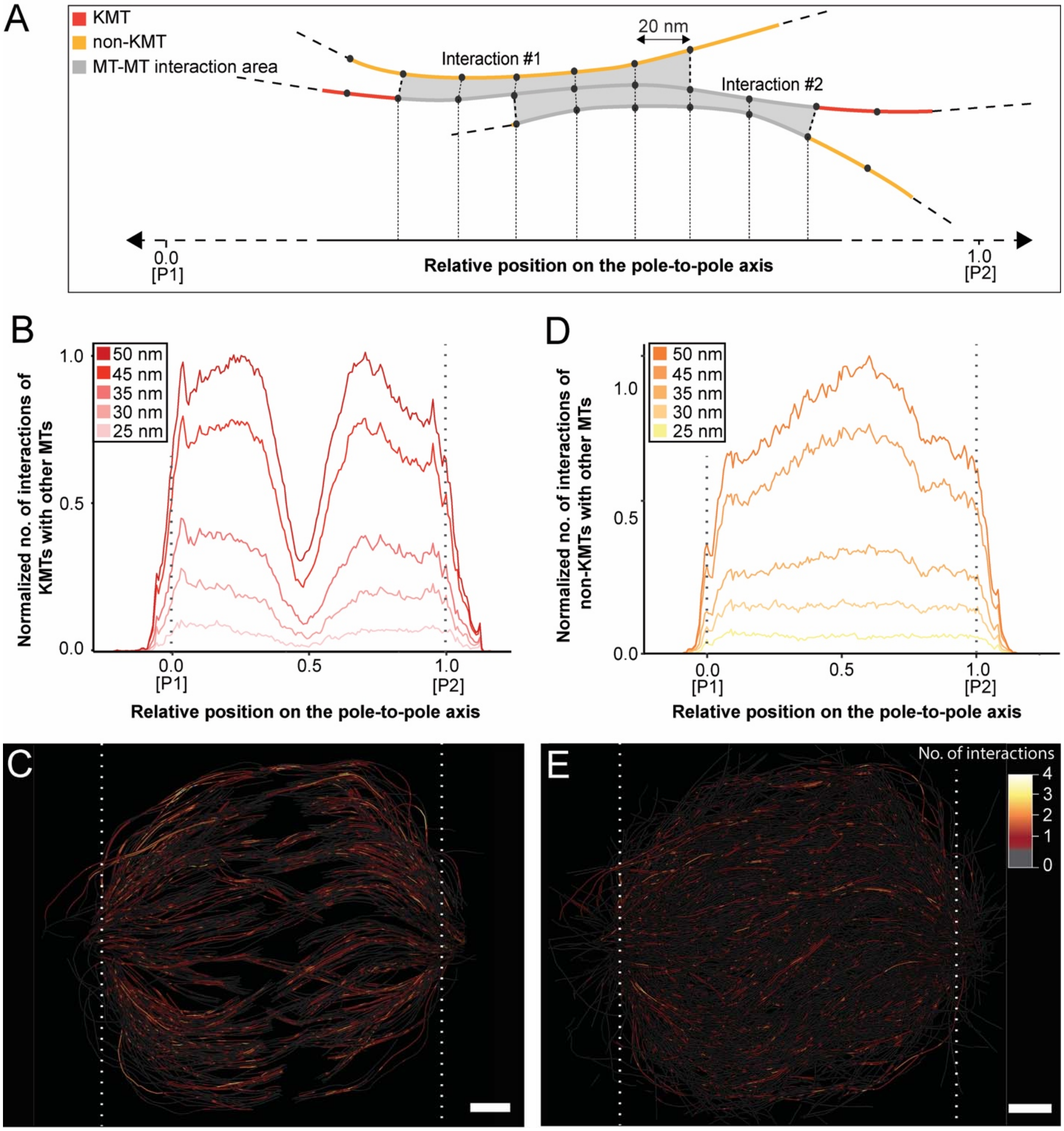

Figure 9. Positions of MT-MT associations

(**A**) Schematic illustration of MT-MT associations. The interactions are given in intervals of 20 nm. This allows mapping of the number of interactions on the pole-to-pole axis (P1 = position 0, P2 = position 1). KMTs are illustrated in red, non-KMTs in yellow, and areas of MT-MT association in gray. (**B**) Graph showing the number of KMTs (normalized against the MT density) associated with other MTs plotted against the relative position of the association on a spindle axis. (**C**) Three-dimensional model of all KMTs showing regions of KMT-MT association within 35 nm or closer (n = 2580). Each KMT segment is color-coded according to the number and position of associations. (**D**) Number of non-KMTs associated with neighboring MTs plotted against the relative position of the association on a spindle axis (normalized against the MT density). Plots are shown for five different thresholds of MT-MT association distances. (**E**) Three-dimensional model of all non-KMTs showing regions of MT-MT association within 35 nm or closer distance (n = 9957). White dashed lines indicate the position of the spindle pole. Scale bars, 1 µm.

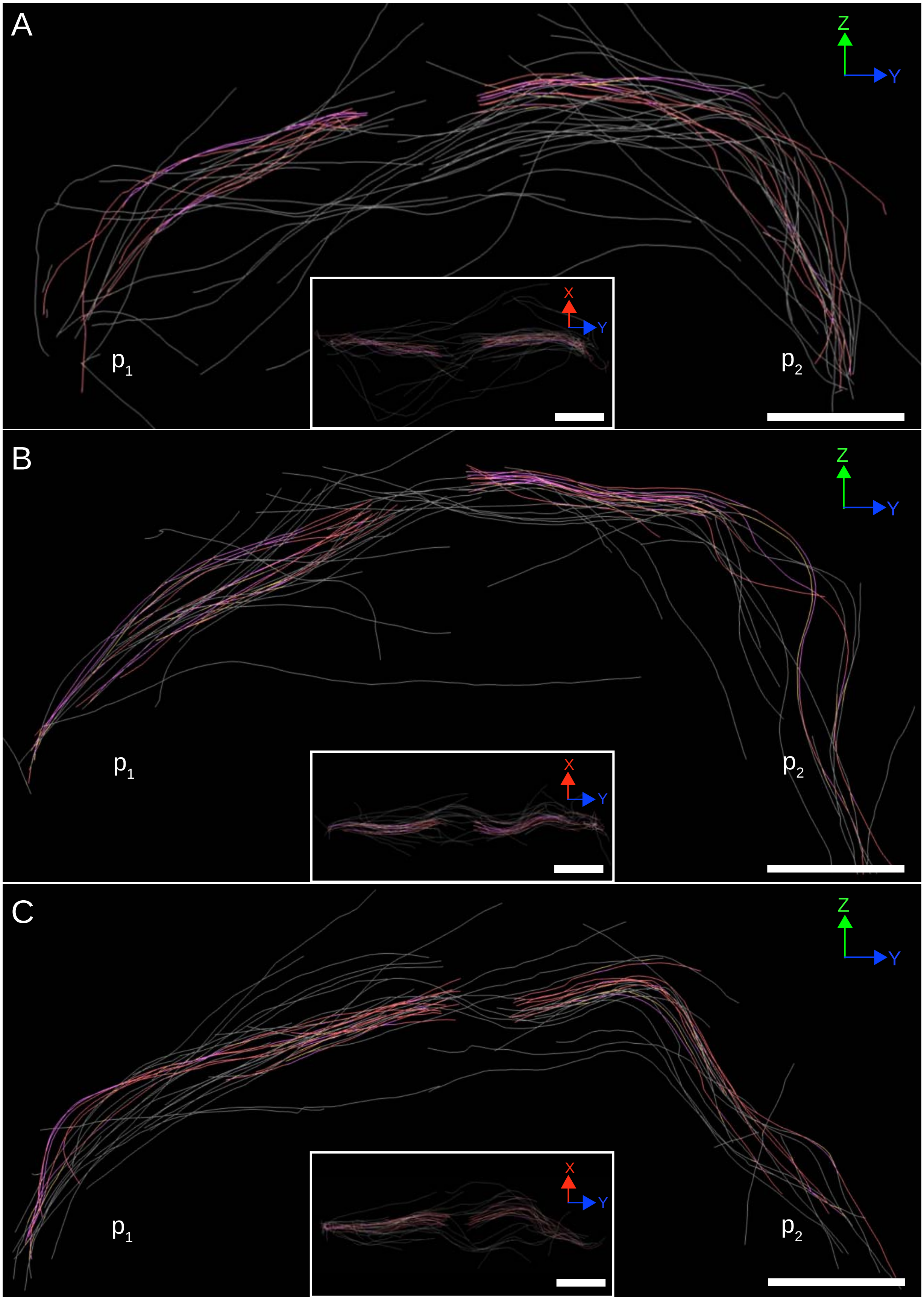
A
Z
Y
X
Y
p1
p2
B
Z
Y
X
Y
p1
p2
C
Z
Y
X
Y
p1
p2

Figure 9-figure supplement 1. Association of KMT lattices with other MT lattices at 35 nm association distance

(**A**) Visualization of KMTs and non-KMTs obtained from the ASGA 3D-Viewer (https://cfci.shinyapps.io/ASGA_3DViewer/) showing a k-fiber pair from spindle #1 (ASGA k-fiber ID: pole1_08). This 3D model illustrates the association of KMT lattices with other KMT lattices minus ends at an association distance of 35 nm. The types of interaction are shown by color-coding. The approximate position of the spindle poles (p_1, p_2) is indicated. The k-fiber pair is shown in a Z/Y (large image) and an X/Y view (insert). (**B**) Model of k-fiber pair with ID: pole1_20. (**C**) Model of k-fiber pair with ID: pole1_23. Scale bars, 1 µm.

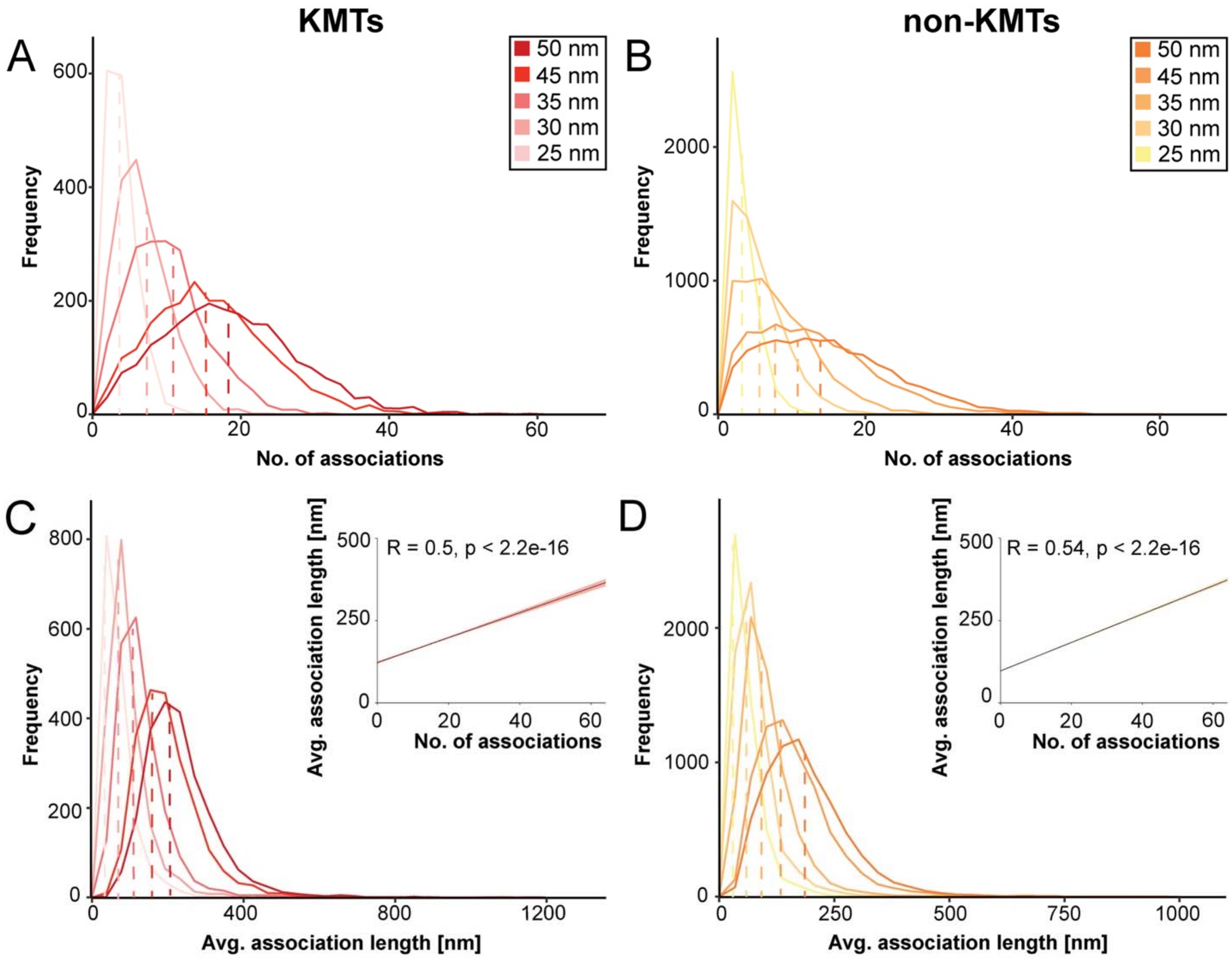

Figure 9-figure supplement 2. Association of KMT lattices with MT minus ends

(**A**) Number of KMTs plotted against the number of associations with other MTs in the spindle per individual KMT (n = 2580). Plots are shown for five different distances between MT-MT. (**B**) Number of non-KMTs plotted against the number of associations (n = 9957). (**C**) Number of KMTs plotted against the average length of MT-MT associations per individual KMT (n = 2580). The correlation of the average length of interactions with the average number of associations is also given (insert). (**D**) Number of non-KMTs plotted against the average length of MT-MT association per individual non-KMT (n = 9957).

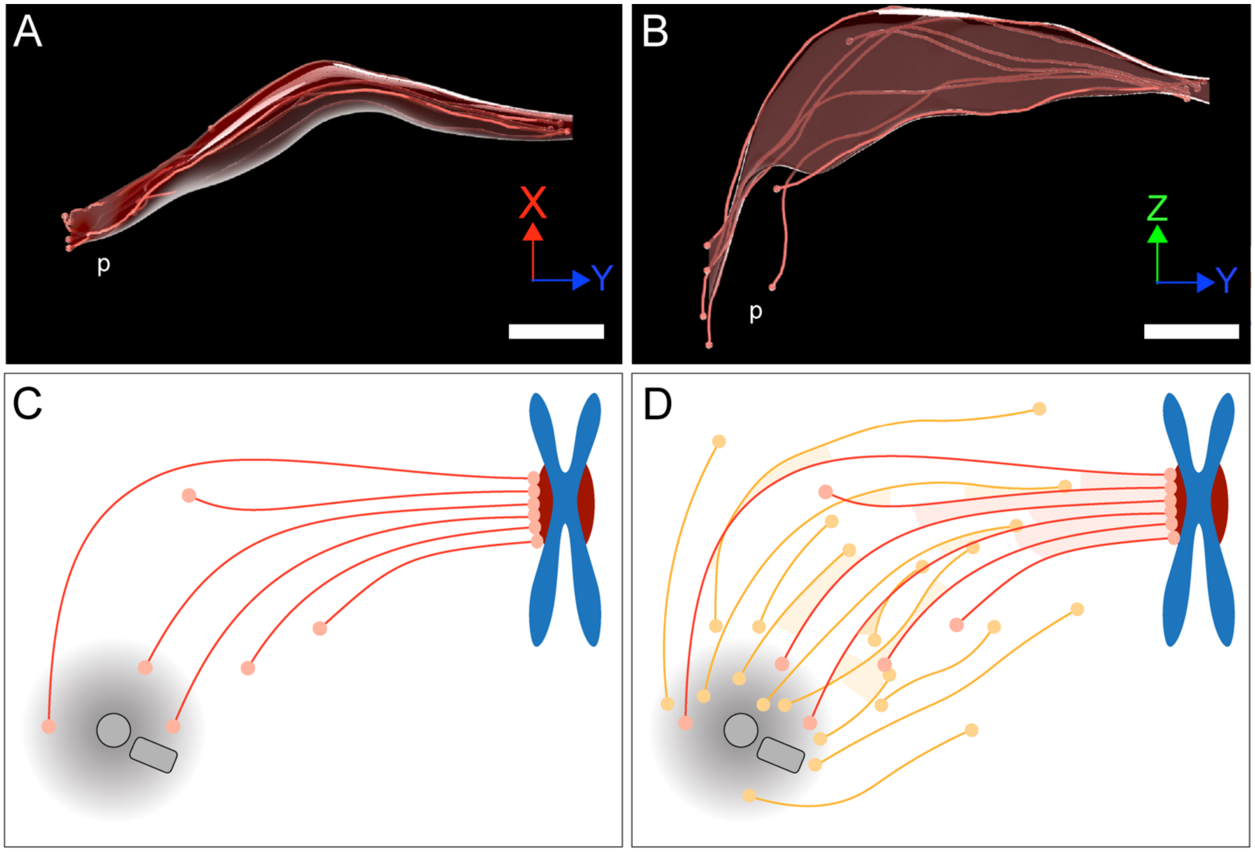

Figure 10. Model of a k-fiber showing a semi-direct connection between a kinetochore and spindle poles

(**A-B**) Three-dimensional views of a selected 3D-reconstructed k-fiber with an overlay k-fiber area drawn around KMTs using the alpha shape method. The KMTs are shown as red lines and the ends are marked with red dots. The approximate position of the pole is indicated (p). The same k-fiber is shown from two different perspectives (side, X/Y, and top, Z/Y view). Scale bars, 1 µm. (**C**) Schematic model of a semi-direct connection between a kinetochore (chromosome in blue, paired kinetochores in dark red) and a spindle pole with centrioles (gray) as established for a single k-fiber. KMTs are shown in red, KMT ends as spheres (light red). (**D**) Schematic model of the k-fiber interaction with a non-KMTs network. Non-KMTs are shown in yellow, and non-KMT ends as spheres (yellow). KMT-KMT interactions are indicated by light red areas, KMT-non-KMT interactions by light yellow areas.

Videos

Figure 2-video 1. Generation of a 3D model from joined serial electron tomograms displaying spindle #1

Series of stitched tomograms and corresponding 3D model of spindle #1. The stacking of serial tomograms to increase the tomographic volume is illustrated. MTs are shown as white lines, and chromosomes are illustrated in blue. This video corresponds to Figure 2C. Scale bars, 1 µm.

Figure 2-video 2. Generation of a 3D model from joined serial electron tomograms displaying spindle #2

Series of stitched tomograms and corresponding 3D model of spindle #2. The stacking of serial tomograms to increase the tomographic volume is illustrated. MTs are shown as white lines, and chromosomes are illustrated in blue. This video corresponds to Figure 2D. Scale bars, 2 µm.

Figure 2-video 3. Generation of a 3D model from joined serial electron tomograms displaying spindle #3

Series of stitched tomograms and corresponding 3D model of spindle #3. The stacking of serial tomograms to increase the tomographic volume is illustrated. MTs are shown as white lines, and chromosomes are illustrated in blue. This video corresponds to Figure 2E. Scale bars, 2 µm.

Figure 2-video 4. Organization of KMTs in spindle #1

Three-dimensional model of spindle #1. Non-KMTs are shown in yellow, and KMTs in red. Chromosomes are illustrated in blue and centrioles in gray. This video corresponds to Figure 2F. Scale bars, 1 µm.

Figure 2-video 5. Organization of KMTs in spindle #2

Three-dimensional model of spindle #2. Non-KMTs are shown in yellow, and KMTs in red. Chromosomes are illustrated in blue and centrioles in gray. This video corresponds to Figure 2G. Scale bars, 1.5 µm.

Figure 2-video 6. Organization of KMTs in spindle #3

Three-dimensional model of spindle #3. Non-KMTs are shown in yellow, and KMTs in red. Chromosomes are illustrated in blue and centrioles in gray. This video corresponds to Figure 2H. Scale bars, 1.5 µm.

Figure 3-video 1. 3D reconstruction of a single k-fiber pair

Three-dimensional model of selected sister k-fibers in spindle #1. The KMTs are shown in red, the KMT ends with white spheres and the centrioles in gray. This video corresponds to Figure 3A (k-fiber pair # I). Scale bars, 1 µm.

Figure 3-video 2. 3D reconstruction of a single k-fiber pair

Three-dimensional model of selected sister k-fibers in spindle #1. The KMTs are shown in red, the KMT ends with white spheres and the centrioles in gray. This video corresponds to Figure 3A (k-fiber pair # II). Scale bars, 1 µm.

Figure 3-video 3. 3D reconstruction of a single k-fiber pair

Three-dimensional model of selected sister k-fibers in spindle #1. The KMTs are shown in red, the KMT ends with white spheres and the centrioles in gray. This video corresponds to Figure 3A (k-fiber pair # III). Scale bars, 1 µm.

Figure 3-video 4. 3D reconstruction of a single k-fiber pair

Three-dimensional model of selected sister k-fibers in spindle #1. The KMTs are shown in red, the KMT ends with white spheres and the centrioles in gray. This video corresponds to Figure 3A (k-fiber pair # IV). Scale bars, 1 µm.

Figure 3-video 5. 3D reconstruction of a single k-fiber pair

Three-dimensional model of selected sister k-fibers in spindle #1. The KMTs are shown in red, the KMT end with white spheres, and the centrioles in gray. This video corresponds to Figure 3A (k-fiber pair # V). Scale bars, 1 µm.

Figure 3-video 6. 3D reconstruction of a single k-fiber pair

Three-dimensional model of selected sister k-fibers in spindle #1. The KMTs are shown in red, the KMT ends with white spheres and the centrioles in gray. This video corresponds to Figure 3A (k-fiber pair # VI). Scale bars, 1 µm.

Figure 6-video 1. Analysis of k-fiber global tortuosity in spindle #1

Three-dimensional model of all KMTs of spindle #1 with indicated global tortuosity. KMTs are color-coded as indicated in Figure 6D. KMT ends are shown as white spheres, centrioles in gray. This video corresponds to Figure 5C. Scale bars, 1 µm.

Figure 6-video 2. Analysis of k-fiber global tortuosity in spindle #2

Three-dimensional model of all KMTs of spindle #2 with indicated global tortuosity. KMTs are color-coded as indicated in Figure 6D. KMT ends are shown as white spheres, centrioles in gray. This video corresponds to Figure 6D (example of spindle #2 shown as a movie only). Scale bars, 1 µm.

Figure 6-video 3. Analysis of k-fiber global tortuosity in spindle #3

Three-dimensional model of all KMTs of spindle #3 with indicated global tortuosity. KMTs are color-coded as indicated in Figure 6D. KMT ends are shown as white spheres, centrioles in gray. This video corresponds to Figure 6D (example of spindle #3 shown as a movie only). Scale bars, 1 µm.

Figure 8-video 1. Associations of KMT minus ends with MT lattices in spindle #1

Three-dimensional model of all KMTs from spindle #1. KMT minus ends interacting with other MTs at association distances up to 35 nm are shown. KMT minus ends interacting with either KMT (red lines) or non-KMT lattices (yellow lines) are illustrated. KMTs without any interactions are shown in gray. This video corresponds to Figure 8C. Scale bars, 1 µm.

Figure 8-video 2. Association of KMT minus end with MT lattices

Three-dimensional model of KMTs from spindle #1 (ASGA k-fiber ID: pole1_08). KMT minus-end interaction with other MTs at an association distance of 35 nm KMT minus ends interacting with either KMTs (purple lines) or non-KMT lattices (yellow lines) is indicated. KMTs without any interactions are shown in gray. This video corresponds to Figure 8-figure supplement 1A. Scale bars, 1 µm.

Figure 9-video 1. Associations of KMT lattices with other MTs

Three-dimensional model of all KMTs in spindle #1. KMT lattices interacting with other MT lattices at association distances of up to 35 nm are shown. KMTs are shown as gray lines with color-coded regions showing the number of MT-MT associations. This video corresponds to Figure 9C. Scale bars, 1 µm.

Figure 9-video 2. Associations of non-KMTs with other MTs

Three-dimensional model of all non-KMTs in spindle #1. Non-KMT lattices interacting with other MT lattices at association distances up to 35 nm are shown. Non-KMTs are shown as gray lines with color-coded regions showing the number of MT-MT associations. This video corresponds to Figure 9E. Scale bars, 1 µm.

Tables

Table 1. Characterization of the 3D-reconstructed metaphase spindles in HeLa cell

Data set	Spindle pole distance [µm]	Inter-kinetochore distance [µm]	No. of MTs in tomographic volume	No. of kinetochores	No. of KMTs	No. of non-KMTs	No. of k-fibers
Spindle #1	7.16	1.08 ± 0.20 (n=43)	4884	92	797 (16.3%)	4087 (83.7%)	92
Spindle #2	10.39	1.24 ± 0.21 (n=50)	8047	110	1102 (13.7%)	6945 (86.3%)	110
Spindle #3	9.48	1.03 ± 0.27 (n=40)	5904	90	680 (11.5%)	5224 (88.5%)	90

Table 2. Quantitative analysis of KMTs and non-KMTs

Data set	Length of KMTs [µm]	Length of non-KMTs [µm]	No. of KMTs per kinetochore	No. of KMTs at MT-centrosome interaction area	Mean KMT minus-end distance to poles [µm]	% of KMTs associated with poles	% of non-KMTs associated with poles
Spindle #1	3.59 (±1.57)	2.13 (±1.67)	8.04 (±1.86)	5.0 (±1.8)	1.72	61.2	44.3
Spindle #2	3.82 (±1.97)	1.95 (±1.60)	9.75 (±2.18)	3.1 (±2.3)	2.87	31.5	28.6
Spindle #3	4.27 (±1.93)	2.07 (±1.93)	7.49 (±1.91)	4.1 (±2.0)	2.12	54.2	41.9

Table 3. Quantitative analysis of the k-fiber organization

Data set	**KMT density at the kinetochore [KMT/µm^2]**	**KMT-KMT distance at the kinetochore [nm]**	**Global tortuosity of KMTs**	**% of curved KMTs**	**Area of k-fibers [µm^2]**	**% of KMTs in a k-fibers**
Spindle #1	122 (± 62)	67 (± 20)	1.11 (± 0.11)	39.8	0.08 (± 0.1)	64 (± 27)
Spindle #2	99 (± 45)	78 (± 23)	1.07 (± 0.07)	28.4	0.09 (± 0.11)	70 (± 25)
Spindle #3	117 (± 72)	76 (± 23)	1.13 (± 0.13)	47.1	0.12 (± 0.24)	59 (± 29)

Table 4. Quantitative analysis of k-fiber positioning in the spindle

Region	Length of KMTs [µm]	No. of KMTs per kinetochore	No. of KMTs at MT-centrosome interaction area	Mean KMT minus-end distance to poles [µm]	No. of KMTs associated with poles	Global tortuosity of KMTs
Central	3.5 (± 1.7)	8.2 (± 2.4)	162 (~48%)	2.0 (± 1.3)	4.3 (± 2.3)	1.08 (± 0.08)
Intermed-iate	3.6 (± 1.7)	8.6 (± 2.1)	266 (~49%)	2.1 (± 1.3)	4.6 (± 1.9)	1.11 (± 0.12)
Peripheral	3.9 (± 2.0)	8.6 (± 2.4)	730 (~45%)	2.5 (± 1.6)	4.1 (± 2.0)	1.10 (± 0.10)

Table 5. Analysis of the potential association of KMT minus ends with other neighboring KMT lattices

Data set	Analysis	Association distances [nm]						
		25	**30**	**35**	**45**	**50**	**75**	**100**
Spindle #1	**No. of KMTs**	37	68	112	204	238	306	330
	% of KMTs	4.9	9.1	15.0	27.3	32.0	40.9	44.1
Spindle #2	**No. of KMTs**	20	37	68	142	177	266	290
	% of KMTs	1.9	3.5	6.3	13.2	16.5	24.8	27.1
Spindle #3	**No. of KMTs**	13	27	66	116	135	199	218
	% of KMTs	1.9	4.0	9.8	17.2	20.0	29.5	32.3

Table 6. Analysis of the potential associations of KMT minus ends with neighboring non-KMT lattices

Data set	Analysis	Association distances [nm]						
		25	**30**	**35**	**45**	**50**	**75**	**100**
Spindle #1	**No. of KMTs**	37	82	132	217	248	353	384
	% of KMTs	4.9	11.0	17.6.0	29.0.6	33.2	47.2	51.3
Spindle #2	**No. of KMTs**	245	313	353	469	5258	677	732
	% of KMTs	22.9	29.2	33.0	43.8	49.0	63.2	68.3
Spindle #3	**No. of KMTs**	28	64	107	198	230	355	410
	% of KMTs	4.2	9.5	15.9	29.4	34.1	52.7	60.8

Table 7. Analysis of the potential association of KMT lattices with other neighboring KMT minus ends

Data set	**No. and % of KMT with KMT associations according to the given association distances [nm]**						
	25	**30**	**35**	**45**	**50**	**75**	**100**
Spindle #1	39 [5%]	71 [10%]	117 [15%]	210 [28%]	236 [31%]	336 [45%]	403 [54%]
Spindle #2	24 [2%]	46 [4%]	86 [8%]	179 [17%]	237 [22%]	401 [37%]	470 [43%]
Spindle #3	14 [2%]	27 4%]	61 [9%]	127 [19%]	148 [22%]	227 [34%]	284 [42%]

Table 8. Analysis of the potential association of KMT lattices with other neighboring non-KMT minus ends

Data set	**No. and % of KMT with non-KMT associations according to the given association distances [nm]**						
	25	**30**	**35**	**45**	**50**	**75**	**100**
Spindle #1	81 (11%)	151 (20%)	223 (30%)	362 (48%)	415 (55%)	534 (71%)	577 (77%)
Spindle #2	51 (5%)	100 (9%)	173 (16%)	351 (33%)	433 (40%)	640 (59%)	717 (67%)
Spindle #3	34 (5%)	93 (14%)	176 (26%)	301 (44%)	348 (51%)	471 (69%)	507 (75%)

Table 9. Average number of associations with MT lattices

Data set	MT type	No. of associations according to the given MT-MT distances [nm]				
		25	30	35	45	50
Spindle #1	**KMTs**	4.8 (± 1.5)	8.6 (± 2.5)	12.4 (± 3.4)	18.8 (± 4.9)	1.3 (±5.5)
	Non-KMTs	4.4 (± 1.5)	7.0 (± 2.6)	9.6 (± 3.7)	13.0 (± 5.4)	16.2 (± 6.2)
Spindle #2	**KMTs**	4.2 (± 1.3)	5.8 (± 1.8)	8.0 (± 2.6)	13.3 (± 4.1)	16.0 (± 4.8)
	Non-KMTs	3.2 (± 0.9)	4.0 (± 1.3)	5.2 (± 1.8)	8.2 (± 3.1)	9.8 (± 3.7)
Spindle #3	**KMTs**	4.2 (± 1.2)	8.0 (± 2.3)	12.4 (± 3.4)	18.6 (± 4.8)	21.2 (± 5.4)
	Non-KMTs	3.6 (± 1.2)	5.2 (± 2.3)	8.0 (± 3.3)	11.6 (± 4.7)	13.2 (± 5.3)
Average	**KMTs**	4.4 (± 1.3)	7.4 (± 2.3)	10.6 (± 3.2)	16.4 (± 4.7)	19.0 (± 5.3)
	Non-KMTs	3.6 (± 1.2)	5.4 (± 2.2)	7.4 (± 3.1)	10.8 (± 4.5)	12.4 (± 5.1)

Table 10. Average length of associations with MT lattices

Data set	MT type	Length of associations according to the given MT-MT distances [nm]				
		25	30	35	45	50
Spindle #1	KMTs	81.3 (± 88.8)	119.7 (± 151.1)	163.9 (± 207.5)	241.3 (± 301.9)	271.0 (± 335.9)
	Non-KMTs	58.3 (± 54.1)	78.3 (± 79.9)	107.7 (± 116.9)	165.1 (± 195.1)	187.9 (± 227.0)
Spindle #2	KMTs	69.5 (± 69.9)	93.2 (± 107.0)	124.3 (± 146.0)	207.8 (± 252.3)	252.2 (± 314,9)
	Non-KMTs	59.2 (± 53.2)	73.2 (± 71.9)	92.3 (± 97.3)	145.8 (± 170.5)	175.1 (± 213.0)
Spindle #3	KMTs	66.1 (± 63.4)	97.3 (± 117.8)	143.2 (± 191.7)	231.3 (± 321.2)	263.4 (± 362.2)
	Non-KMTs	54.3 (± 51.7)	74.5 (± 86.4)	104.6 (± 133.7)	165.6 (± 218.7)	191.3 (± 252.0)
Average	KMTs	73.0 (± 76.2)	104.6 (± 129.2)	145.1 (± 186.0)	225.6 (± 292.3)	261.9 (± 336.8)
	Non-KMTs	57.2 (± 53.1)	75.4 (± 80.5)	102.2 (± 118.9)	159.1 (± 197.2)	184.9 (± 232.1)

Table 11. Tomographic data sets as used throughout this study

Data set	Original data set	Montage (X/Y)	No. of serial sections [300 nm each]	Estimated tomographic volume [µm^3]	Data set size [Gb]
Spindle #1	T_0475	2x3	22	598	46.5
Spindle #2	T_0479	2x3	29	996	77.9
Spindle #3	T_0494	2x3	35	904	71.9

Table 12. Quantification of KMT structure before and after application of Z-expansion to the 3D models

Data set	**Length of KMTs [µm]**		**Length of non-KMTs [µm]**		**No. of KMTs per kinetochore**		**No. of KMTs at MT-centrosome interaction area**		**Mean KMT minus-end distance to poles [µm]**		**No. of KMTs associated with poles [%]**		**No. of non-KMTs associated with poles [%]**	
	Before	After	Before	After	Before	After	Before	After	Before	After	Before	After	Before	After
Spindle #1	3.23 (±1.49)	3.59 (±1.57)	2.03 (±1.6)	2.13 (±1.67)	8.04 (±1.86)	8.04 (±1.86)	4.1 (±1.8)	5.0 (±1.8)	1.16	1.72	62.2	61.2	44.5	44.3
Spindle #2	3.69 (±1.87)	3.82 (±1.97)	1.85 (±1.55)	1.95 (±1.60)	9.75 (±2.18)	9.75 (±2.18)	2.4 (±2.0)	3.1 (±2.3)	2.47	2.87	53.6	31.5	28.8	28.6
Spindle #3	4.03 (±1.79)	4.27 (±1.93)	1.91 (±1.80)	2.07 (±1.93)	7.49 (±1.91)	7.49 (±1.91)	3.4 (±1.8)	4.1 (±2.0)	1.35	2.12	62.0	54.2	42.3	41.9

Table 13. Quantification of the k-fiber organization before and after application of Z-expansion to the 3D models

Data set	**Density of KMTs at the kinetochore [KMT/μm^2]**		**KMT-KMT distance at the kinetochore [nm]**		**Global tortuosity of KMTs**		**% of curved KMTs**		**Area of k-fibers [μm^2]**		**% of KMTs in a k-fibers**	
	Before	After	Before	After	Before	After	Before	After	Before	After	Before	After
Spindle #1	151 (± 74)	122 (± 62)	61 (± 11)	67 (± 20)	1.09 (± 0.10)	1.11 (± 0.11)	36.1	39.8	0.063 (± 0.09)	0.08 (± 0.1)	34 (± 27)	64 (± 27)
Spindle #2	137 (± 68)	99 (± 45)	65 (± 12)	78 (± 23)	1.06 (± 0.06)	1.07 (± 0.07)	21.4	28.4	0.068 (± 0.10)	0.09 (± 0.11)	70 (± 25)	70 (± 25)
Spindle #3	175 (± 123)	117 (± 72)	66 (± 12)	76 (± 23)	1.11 (± 0.11)	1.13 (± 0.13)	39.5	47.1	0.080 (± 0.15)	0.12 (± 0.24)	59 (± 39)	59 (± 29)